Transient processes near the threshold of subharmonic resonance

A. O. Maksimov and E. V. Sosedko

Pacific Ocean Oceanological Institute, Far East Branch of the ran, Vladivostok
(Submitted April 1, 1999)
Pis'ma Zh. Tekh. Fiz. **25**, 1–6 (September 12, 1999)

Instability of a dynamical system near a subharmonic resonance is manifested in the prolongation of transient processes. It is shown for nonlinear pulsations of a gas bubble under the action of an acoustic carrier signal modulated by a pulse that the subharmonic radiation observed experimentally below the generation threshold can be explained by the contribution of characteristic oscillations which arise at the moment the pulse arrives and have a damping time comparable to the pulse duration, due to the parametric energy transfer. © *1999 American Institute of Physics.* [S1063-7850(99)00109-3]

The response of a nonlinear dynamical system to an external harmonic perturbation is unusual in that spectral components below the excitation frequency appear. These components are said to be subharmonic. The best known example is the 1/2 component, whose frequency is half the excitation frequency. In contrast to higher-order harmonics, whose amplitudes grow continuously with the intensity of the perturbation, the appearance of subharmonic components is of a threshold character.

In what follows, we shall analyze as an example of such a system the radial pulsations of a gas bubble in a liquid under the action of a powerful acoustic wave. The detection of the subharmonic component (we shall always be referring to the 1/2 component) is a general characteristic of cavitation and other nonlinear phenomena in liquids containing phase inclusions.[1–5] At the same time, as first observed by Neppiras,[2] a small subharmonic component is also observed below threshold,[6–8] so that the growth of this spectral component is not, strictly speaking, of a threshold character.

The explanation proposed in the present letter involves the analysis of transient processes near a subharmonic resonance. Near threshold the state in which oscillations at the fundamental frequency have zero amplitude becomes unstable, and one of the two Lyapunov exponents goes to zero. When an external field is switched on (as a rule, experiments are performed with modulated pulsed signals containing from ten to hundreds of pump periods $T=2\pi/\omega_p$), besides forced oscillations, characteristic oscillations with frequency $\sim\omega_p/2$ are excited. Near threshold the damping of the characteristic oscillations, which is determined by a Lyapunov exponent, is very small because of parametric energy transfer into this component (it vanishes at the threshold value of the pump amplitude). For this reason, the time of the transient processes can be greater than the duration of the pump pulse, and the corresponding component in the radiation spectrum can be interpreted as the appearance of a subharmonic component below threshold.

To analyze the effect quantitatively we shall employ the Rayleigh–Plesset equation describing the pulsations of a bubble in a pressure field $P_p=P_m\cos(\omega_p t+\alpha)$

$$R\ddot{R}+\frac{3}{2}\dot{R}^2+\frac{P_0}{\rho_0}\left[1-\left(\frac{R_0}{R}\right)^{3\gamma}\right]+2\delta R_0\dot{R}=-\frac{P_p}{\rho_0}. \tag{1}$$

Here γ is the ratio of specific heats; δ is the damping, which effectively takes account of the dissipative processes, due to viscosity and heat conduction, as well as radiation losses; P_0, ρ_0, and R_0 are the equilibrium values of the pressure and density of the liquid and the bubble radii. The asymptotic expansion of the solution of Eq. (1) near a subharmonic resonance $|\omega_p-2\Omega_0|\ll\omega_p$ (see, for example, Refs. 9–11) has the form

$$(R-R_0)/R_0=a\cos(i\Omega_0 t+i\vartheta)+\frac{P_m\cos(\omega_p t+\alpha)}{\rho_0 R_0^2(\omega_p^2-\Omega_0^2)}+\varepsilon u_1(a,\vartheta,t)+\varepsilon^2 u_2(a,\vartheta,t)+\ldots \tag{2}$$

Here $\Omega_0=(3\gamma P_0/\rho_0 R_0^2)^{1/2}$ is the characteristic frequency of the bubble and ε is a small dimensionless parameter introduced to designate the order of the nonlinear terms. The slowly varying amplitude a and phase ϑ of the oscillations are determined from a system of ''truncated'' equations that follows from the requirement that there be no secular terms in the expansion. Taking account of terms up to second order inclusively in Eq. (1) gives the following equation for $z=a\exp(i\vartheta)\exp[-i(\omega_p/2-\Omega_0)t]$:

$$\dot{z}=-\delta z-i\Delta\Omega z-i\delta\frac{P_m}{P_k}\exp(i\alpha)z^*,$$

$$\Delta\Omega=\omega_p/2-\Omega_0,\quad P_k=4\delta\Omega_0\rho_0 R_0^2\gamma^{-1}. \tag{3}$$

This equation must be supplemented by initial data for a and ϑ, which can be obtained by substituting the expansion (2) into the exact initial conditions. When the bubble is excited from rest, $R(0)=0$ and $dR/dt(0)=0$, we have

$$a(0)=\frac{P_m}{3\rho_0 R_0^2\Omega_0^2}\sqrt{1+3\sin^2\alpha};\quad \tan\vartheta(0)=2\tan\alpha. \tag{4}$$

The solution of the system of equations (3) with constant coefficients is

$$z(t)=\exp(-\lambda_1 t)\frac{1}{2}\left[z(0)\left(1-i\frac{2\Delta\Omega}{\lambda_1-\lambda_2}\right)-iz^*(0)\frac{\delta P_m}{P_k(\lambda_1-\lambda_2)}\right]+\exp(-\lambda_2 t)\frac{1}{2}\left[z(0)\times\left(1+i\frac{2\Delta\Omega}{\lambda_1-\lambda_2}\right)+iz^*(0)\frac{\delta P_m}{P_k(\lambda_1-\lambda_2)}\right], \quad (5)$$

where $\lambda_{1,2}=\delta[1\mp\sqrt{(P_m^2/P_k^2)-(\Delta\Omega/\delta)^2}]$ are Lyapunov exponents.

Near threshold $P_m=P_b-\Delta P$, where $\Delta P>0$, $\Delta P \ll P_b$, and $P_b^2=P_k^2[1+(\Delta\Omega/\delta)^2]$, the exponent $\lambda_1=\delta[1-\sqrt{(P_m^2/P_k^2)-(\Delta\Omega/\delta)^2}]=\delta[1-\sqrt{1-(P_b^2/P_k^2)-(P_m^2/P_k^2)}]\approx\delta(\Delta P P_b/P_k^2)$ is small, so that the first term in Eq. (5) will dominate at times $t=\lambda_1^{-1}\approx[\delta(\Delta P P_b/P_k^2)]^{-1}\gg\delta^{-1}$ and describe the subharmonic component of the radiation of the bubble.

Substituting explicit expressions for the initial values $z(0)$ and $z^*(0)$ we obtain

$$a(t)\cos(\Omega_0 t+\vartheta(t))=a(0)(P_b/P_k)\exp[-\delta t(\Delta P P_b/P_k^2)]\mathrm{Re}\{\exp[i((\omega_p/2)t+\tan^{-1}(2\tan\alpha))]0.5[\exp i(\tan^{-1}(\Delta\Omega/\delta))-\exp i(\pi/2-2\tan^{-1}(2\tan\alpha)+\alpha)]\}. \quad (6)$$

As follows from this expression, the efficiency of excitation of the weakly-stable component of the characteristic oscillations depends on the phase α of the external field. This effect is greatest for $P_m<P_k$, while for a continuous distribution of the bubble sizes P_k is the experimentally observed threshold for the excitation of the subharmonic component. The conditions for damping to be small in this region are $P_k-P_m\ll P_k$ and $(\Delta\Omega)^2\ll\delta^2$. Excitation will be extremely inefficient for a pump wave with phase close to $\pi/2$. As follows from Eq. (6), the difference of the exponentials in the brackets is $\sim(\Delta\Omega)/\delta$ in this case. It should be noted that in the now classic works of Lauterborn,[12–14] which are devoted to the analysis of the nonlinear dynamics of a bubble by numerical methods, the phase of the external field was assumed to be $\pi/2$.

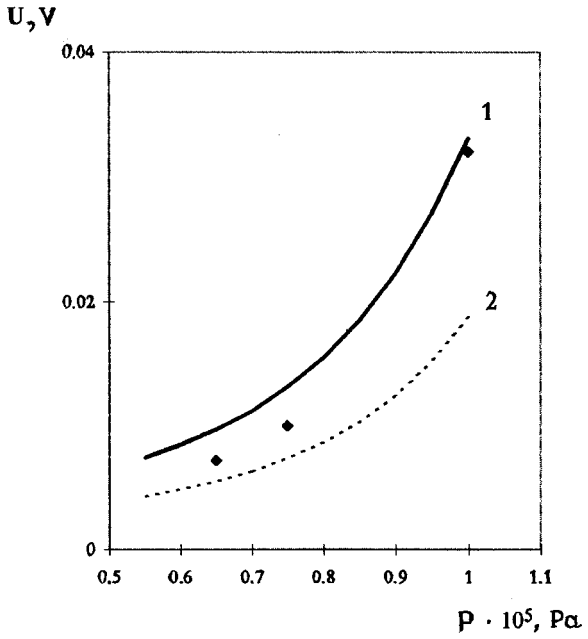

FIG. 1.

We shall now compare our results with existing experimental data.[6] The region where $(5-10)\times10^{-6}$ m bubbles were produced by electrolysis was probed with ultrasonic pulses with a 1.2 MHz carrier frequency and 10 μs duration. A selective detector was used to measure the signal level at 0.6 MHz. The results show that there is no clear generation threshold for probe pulse amplitudes in the range $(0.25-1)\times10^5$ Pa. These data are shown in the figure by black squares.

The spectral density of the subharmonic signal emitted by the bubble under the action of a carrier shaped by a pulse with duration T is proportional to

$$S(\omega_p/2)\sim\frac{(1-\exp[-T(\delta-\lambda_1)])^2+2(1-\cos(\Delta\Omega T))\exp[-T(\delta-\lambda_1)]}{((\delta-\lambda_1)/\delta)^2+(\Delta\Omega/\delta)^2}. \quad (7)$$

The damping coefficient δ of a bubble with resonance frequency 0.6 MHz is, according to Ref. 15, $\delta\sim4\times10^5\ \mathrm{s}^{-1}$. The threshold P_k of a subharmonic resonance will be equal to (see the definition (3) or the more accurate expression given in Ref. 10 taking account of surface tension) $P_k\sim0.8\times10^5$ Pa. Since the bubble density was not determined during the experiments being discussed, we treated the bubble density as an adjustable parameter and plotted the subharmonic signal level versus the pressure, starting from the expression (7), for various values of the offset. The curve *1* corresponds to exact resonance $\Delta\Omega=0$ and the curve *2* corresponds to $\Delta\Omega/\delta=0.5$. The qualitative agreement is a definite argument in support of the proposed explanation. However, to make a quantitative comparison the contributions of individual bubbles must be systematically summed and the Rayleigh equation must be solved numerically, since the large value of the threshold limits the accuracy of the asymptotic expansion employed.

In closing, we note that although the results presented above are for a specific physical model, the fact that a wide class of nonlinear dynamical problems, described by, for example, the Duffing equation, has the same structure as the

truncated equation (3) enables us to predict prolongation of transient processes in these systems near the threshold of a subharmonic resonance.

We thank V. A. Bulanov for a fruitful discussion.

[1] R. Esche, Acustica **2**, 208 (1952).
[2] H. G. Flynn, in *Physical Acoustics*, edited by W. P. Mason, Vol. I–Part B (Academic Press, New York, 1964), pp. 58–172.
[3] E. A. Neppiras, J. Acoust. Soc. Am. **46**, 587 (1969).
[4] A. Eller and H. G. Flynn, J. Acoust. Soc. Am. **46**, 722 (1969).
[5] T. G. Leighton, *The Acoustical Bubble* (Academic Press, London, 1994).
[6] A. D. Mansfel'd and A. M. Reĭman, in *Ultrasonic Diagnostics* (Institute of Applied Physics, Soviet Academy of Sciences, Gor'kiĭ, 1983), pp. 151–161.
[7] A. G. Kirilov, A. D. Mansfeĺd, A. M. Reĭman, and P. K. Chichagov, in *Problems of Nonlinear Acoustics*, Part 2 (Institute of Hydrodynamics, Novosibirsk, 1987), pp. 32–34.
[8] O. Losberg, J. M. Hovem, and B. Aksum, J. Acoust. Soc. Am. **99**, 1366 (1996).
[9] A. Prosperetti, J. Acoust. Soc. Am. **56**, 878 (1974).
[10] A. Prosperetti, J. Acoust. Soc. Am. **57**, 810 (1975).
[11] A. O. Maksimov, Zh. Tekh. Fiz. **58**, 822 (1988) [Sov. Tech. Phys. Lett. **33**, 500 (1988)].
[12] W. Lauterborn, Acustica **22**, 238 (1969/70).
[13] W. Lauterborn, J. Acoust. Soc. Am. **59**, 283 (1976).
[14] E. Cramer and W. Lauterborn, Acustica **49**, 280 (1981).
[15] C. J. Church, J. Acoust. Soc. Am. **97**, 1501 (1994).

Translated by M. E. Alferieff

Transmission function of a directional coupler with a saturable nonlinearity

P. I. Khadzhi and O. K. Orlov

Dnestrovsk State University, Tiraspol', Moldavia
(Submitted January 29, 1999)
Pis'ma Zh. Tekh. Fiz. **25**, 7–12 (September 12, 1999)

It is shown that when saturation is taken into account, the transmission function of a directional coupler is more complicated than the Kerr function. Specifically, transmission characteristics with two critical points of self-switching exist. [S1063-7850(99)00209-8]

The investigation of nonlinear directional couplers (NDCs), which are based on the laws of propagation of unidirectional distributed-coupled waves, opens up wide prospects for creating superfast all-optical switches.[1–3] The phenomenon of self-switching of waves was predicted in Ref. 1. It consists in the fact that even weak changes of the input intensity of one wave give rise to abrupt changes in the intensities of both waves at the output of the system. In Ref. 2 the effect of saturation in the refractive index of the medium was studied by numerical methods, and it was shown that the operational characteristics of NDCs are qualitatively different from those of Kerr media. In this connection, it is of interest to obtain exact analytical solutions of the system of equations for an NDC in a model of a medium with exponential saturation of the refractive index (propagation constant).

Let us consider an NDC consisting of two identical optical waveguides whose propagation constant β depends on the intensity J of the propagating waves as[2]

$$\beta=\beta_0+\alpha\exp\left(-\frac{J}{J_s}\right), \tag{1}$$

where β_0, α, and J_s are constants. We shall assume that the coupling constant γ of the coupler does not depend on the intensity[1–3] and that light absorption in the medium in vanishingly small.

The nonlinear differential equations for the amplitudes E_1 and E_2 of the coupled waves propagating along the x axis of the guides in the NDC have the following form in this case:[1–4]

$$\frac{dE_k}{dx}=-i\left(\beta_0+\alpha\exp\left(-\frac{J_k}{J_s}\right)\right)E_k+i\gamma E_{3-k}, \quad k=1,2. \tag{2}$$

Introducing the functions

$$J_1=\frac{c}{8\pi}|E_1|^2, \quad J_2=\frac{c}{8\pi}|E_2|^2,$$

$$Q=\frac{c}{8\pi}(E_1^*E_2-E_2^*E_1), \quad R=\frac{c}{8\pi}(E_1^*E_2+E_2^*E_1) \tag{3}$$

and using Eqs. (2)–(3) we obtain the following system of coupled nonlinear equations:

$$\frac{dJ_1}{dx}=i\gamma Q, \quad \frac{dJ_2}{dx}=-i\gamma Q,$$

$$\frac{dQ}{dx}=i\alpha\left(\exp\left(-\frac{J_1}{J_s}\right)-\exp\left(-\frac{J_2}{J_s}\right)\right)R+2i\gamma(J_1-J_2),$$

$$\frac{dR}{dx}=i\alpha\left(\exp\left(-\frac{J_1}{J_s}\right)-\exp\left(-\frac{J_2}{J_s}\right)\right)Q. \tag{4}$$

We shall find the solutions of this system of equations under the condition that laser radiation with amplitude E_0 (intensity J_0) enters at the input of one of the guides in the NDC (for example, the first one). Then three integrals of motion and a differential equation for the light intensity in the first guide can be derived from Eq. (4), whose solution is conveniently written in quadratures in the form

$$\int_{y_1}^{y_0}[y(y_0-y)-a(1-\exp(-y))^2\times(1-\exp(y-y_0))^2]^{1/2}dy=2\gamma x, \tag{5}$$

where the following scaled variables were introduced:

$$y_1=\frac{J_1}{J_s}, \quad y_0=\frac{J_0}{J_s}, \quad a=\frac{\alpha^2}{4\gamma^2}. \tag{6}$$

Here y_1 is the normalized light intensity in the first guide in the NDC, y_0 is the pump intensity, and a is the nonlinearity parameter.

It follows from Eq. (5) that the intensity of the light propagating along the first guide varies periodically from the value y_0 up to a certain minimum value given by the root of the nonlinear transcendental equation, obtained by setting the radicand of the expression in Eq. (5) to zero, which closest to y_0.

Investigation of the phase trajectories of the differential equation corresponding to the integral (5) and the bifurcation curve in the (a,y_0) plane shows that qualitatively different types of solutions exist. For $a<a_c$ complete transfer of light intensity from the first to the second guide occurs, while for $a>a_c$ less than half the intensity y_0 at the guide input is

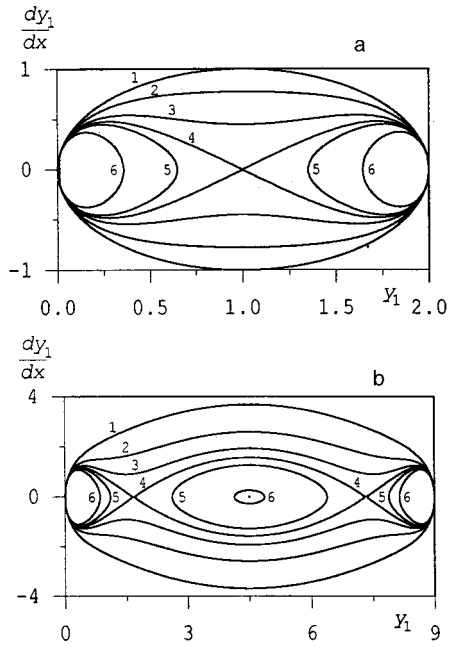

FIG. 1. Phase trajectories in the $(dy_1/dx, y_1)$ plane for the cases $0<y_0<5.97$ (a) and $y_0>5.97$ (b) with various values of the nonlinearity parameter a: a) *1*—0.0, *2*—1.0, *3*—5.0, *4*—6.26, *5*—7.0, *6*—12.5; b) *1*—7.0, *2*—14.2, *3*—17.3, *4*—18.6, *5*—19.5, *6*—21.1.

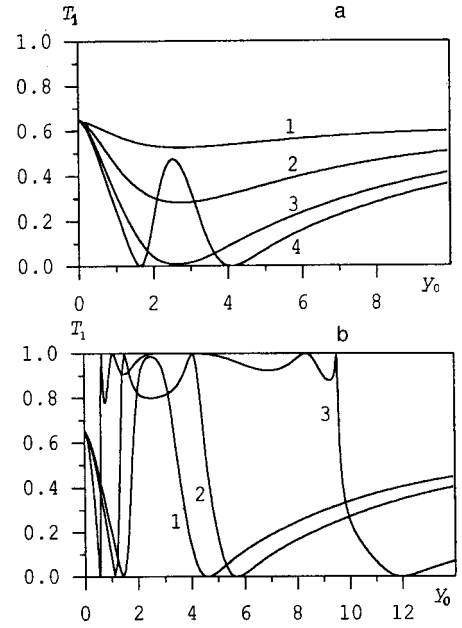

FIG. 2. Transmission function $T_1(y_0)$ of the first guide, pumped from the end, with NDC length $L/L_0=5$ and various values of the nonlinearity parameter a: a) *1*—1, *2*—2, *3*—5, *4*—$a>a_c$; b) *1*—6.5, *2*—8.0, *3*—20.

transferred into the second guide. Here the critical value a_c of the nonlinearity parameter is given by the expression

$$a_c=\frac{y_0^2}{4(1-\exp(-y_0/2))^4}. \tag{7}$$

For $a=a_c$ exactly half the intensity y_0 is transferred into the second guide. This occurs over an infinitely long distance from the front end. The solution with $a=a_c$ is unstable. Vanishingly small variations of the parameter a in either direction from a_c convert the solution into a region with a different behavior of the function $y_1(x)$. In the region $y_0>5.97$ a fork appears in the bifurcation curve $a_c(y_0)$ in the (a,y_0) plane, i.e., there arises a new section of the curve below which light propagates with total transfer, while with a transition through the new bifurcation curve the transferred intensity is less than half. Figure 1 shows the phase trajectories of the solution in the $(dy_1/dx, y_1)$ plane for various values of the parameters y_0 and a. These trajectories show the existence of various types of solutions separated by separatrices. The separatrices correspond to the values of y_0 and a located on the bifurcation curves in the (a,y_0) plane which separate regions in which the solutions behave differently.

The coupling length is a complicated function of y_0 and a. For values of y_0 and a lying on the bifurcation curves or on the separatrices, the coupling length becomes infinite. For other values of a and y_0 the coupling length is finite. We note that for $a>6.029$ the coupling length becomes infinite twice as y_0 increases.

Figure 2 shows the transmission functions (power transmission coefficient) $T_1=y/y_0$ of the first guide in the NDC, pumped from the end, as a function of the excitation level y_0 for various values of the nonlinearity parameter a and NDC length $L/L_0=5$. The length L was chosen to be greater than the coupling length $L_0=\pi/(2\gamma)$ of a linear coupler.

Analyzing the results presented in Fig. 2, we can conclude that the behavior of the transmission function of the NDC including saturation is more diverse and more complicated than for a Kerr NDC.[1] For $a<a_c$ the curve $T_1(y_0)$ is characterized by sections with smoothly increasing and decreasing transmission in the range of small values of y_0. The decrease in T_1 on the initial section of the curves is due to the increase in the coupling length with increasing y_0. When the coupling length as a function of the excitation level y_0 is equal to the length of the coupler, complete transfer of radiation from the first into the second guide occurs and the transmission of the first guide is zero. It is significant that the transmission function does not have an oscillatory tail with transmission essentially equal to 1 when the excitation level y_0 increases, as is characteristic of a Kerr NDC.[1]

For $a>a_c$ the transmission curve vanishes twice with increasing y_0 for different values of y_0, and irregular oscillatory changes occur between these points near $T\approx 1$. The number of oscillations and the width of the region of oscillations increase as functions of the nonlinearity parameter a. Another characteristic feature of the transmission function is the presence of two steep sections in $T_1(y_0)$. They correspond to values of y_0 for which the coupling length of the NDC is equal to the length of the coupler.

Comparing our results with those of Ref. 1 for a Kerr NDC, we can conclude that self- (double) switching exists in NDC with saturation. In contrast to Ref. 1, saturation results in the existence of transmission characteristics with two criti-

cal self-switching points. If the input radiation intensity is slightly less or slightly greater than the critical intensity, corresponding to the midpoint of the actually linear, steep section of transmission, then virtually all of the input radiation ends up in one or the other guide in the coupler. Therefore small variations of the input intensity near the critical point give rise to abrupt changes in the output intensity. This effect can be used to produce all-optical switches, weak-signal amplifiers, optical transistors, and other devices for integrated optics.

[1] A. A. Maĭer, Usp. Fiz. Nauk **165(9)**, 1037 (1995).
[2] Y. Chen, J. Opt. Soc. Am. B **8**, 986 (1991).
[3] F. Kh. Abdullaev and R. Gulyamov, Pis'ma Zh. Tekh. Fiz. **18**(20), 10 (1992) [Sov. Tech. Phys. Lett. **18**, 653 (1992)].
[4] J. D. Begin and M. Cada, IEEE J. Quantum Electron. **QE-30**, 3006 (1994).

Translated by M. E. Alferieff

Investigation via characteristic electron energy loss spectroscopy of the chemical interaction of antimony with a eutectic composite in the aluminum–nickel system

L. I. Antonova, V. P. Denisov, and Yu. A. Fadin

St. Petersburg State University, Russia
(Submitted March 9, 1999)
Pis'ma Zh. Tekh. Fiz. **25**, 13–17 (September 12, 1999)

The interaction of thin layers of antimony with a substrate consisting of an Al_3Ni eutectic composite was investigated by characteristic electron energy loss spectroscopy. It was found that antimony interacts chemically with the substrate, which makes it possible to control the surface activity of the main material. © *1999 American Institute of Physics.*
[S1063-7850(99)00309-2]

Eutectic-based composite materials are of great interest as promising materials for especially critical structural applications. One such material is a eutectic composite in the aluminum–nickel system. It is distinguished by high corrosion resistance and large Young's modulus, reaching 187 GPa.[1] One of the problems in using this material remains reliable binding of the components. As is well known, this problem is characteristic for any aluminum alloys and is the other side of the coin of their stability with respect to external perturbations.[2]

The objective of the present work is to investigate the possibility of controlling the surface properties of a eutectic composite by depositing active films. The eutectic samples were prepared by the standard technology and consisted of cylinders 3–5 mm in diameter, made by threading a large number of single-crystal Al_3Ni filaments through an aluminum matrix. The cylinders were sawed with a circular diamond saw and chemically treated in a hydrochloric acid solution. Next, they were placed in a vacuum chamber, which made it possible to investigate the electronic secondary-emission spectra, including Auger spectra and characteristic energy loss spectra, and to deposit aluminum and antimony films. After the standard evacuation and degassing at 150 °C, a 10^{-7} Pa vacuum was attained in the system.

The Auger spectra of the samples contained the main peaks of aluminum, nickel, oxygen, and carbon, the latter being quite large in all cases. The observed carbon seemed to have been introduced at the time the sample was grown, since the control samples did not show such a peak. The peaks of the characteristic energy losses (CELs) of secondary electrons did not correspond to the characteristic losses of any of the materials present or their oxides (Fig. 1). Their distinguishing property was that the position depended on

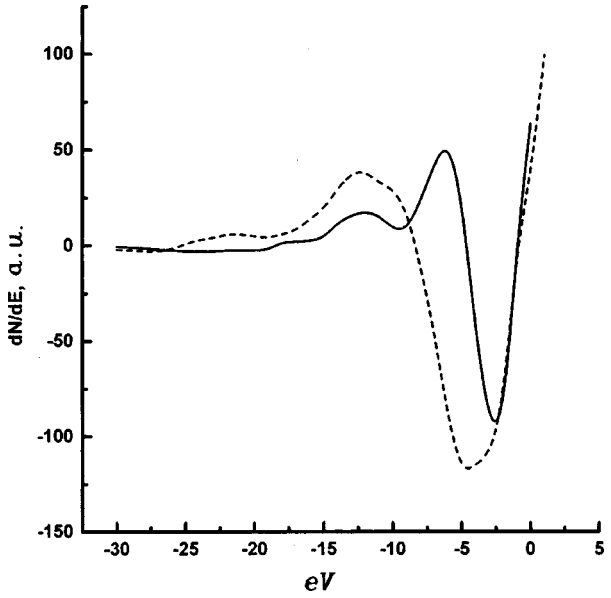

FIG. 1. Characteristic energy loss spectrum of the eutectic composite Al_3Ni. The primary-electron energies are 246 eV (solid line) and 470 eV (dashed line).

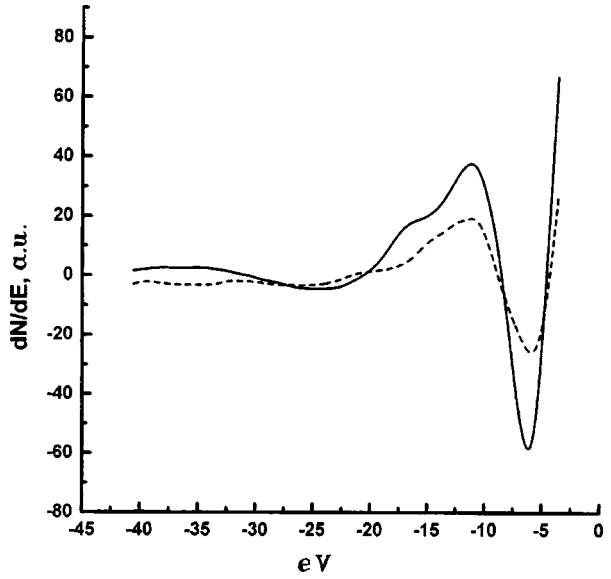

FIG. 2. Characteristic energy loss spectrum of the eutectic composite Al_3Ni with a 3 nm thick antimony layer. The primary electron energies are 246 eV (solid line) and 470 eV (dashed line).

the energy of the primary electron beam. This phenomenon is presumably associated with the excitation of electronic levels of the *d* band, which in this material is very well developed,[3] though the possibility of certain plasma-type oscillations being excited in the thin Al_3Ni filaments cannot be ruled out. It is well-known that plasmon oscillations in low-dimensional structures, for example, thin layers, can exhibit very specific properties.[4]

The deposition of aluminum led to a completely predictable result. At the initial stages the carbon and oxygen Auger peaks disappeared, and the CEL structure changed sharply. The nickel Auger peaks remained for thickest films. For thick aluminum films, a characteristic structure of volume and surface plasmons of aluminum appeared.

The behavior of the system with thin antimony layers is much more interesting. Even with approximately one-tenth of an angstrom of antimony, when the Auger spectrum was essentially constant, with the exception of the appearance of an antimony peak, the CEL spectrum changed sharply. Its general shape was transformed, and the position of the main feature stabilized at 8.5 eV (Fig. 2). Note that this position of the CEL can be due only to nickel, for which CELs equal to 8.5 eV have been recorded,[5] but formed clusters of metallic nickel are very unlikely to appear in this process. When the sample with an antimony film was allowed to stand at room temperature for 12–16 h, the initial structure of CELs was restored, just as the Auger spectra.

The most likely explanation of the observed phenomena is a chemical reaction of the type

$$Al_3Ni + 3Sb = 3AlSb + Ni,$$

which occurs with substantial energy release. The heat of formation of the compound AlSb is 49 kJ/mole and that of Al_3Ni is only 40 kJ/mole, which corresponds to about 0.16 eV released per atom participating in the reaction. In our view, the observed CEL spectrum refers precisely to aluminum antimonide.

Similar reactions in Al–Ni systems have been observed repeatedly, though at somewhat higher temperatures,[6] and in Ref. 7 it is mentioned such reactions can also occur at room temperature. For our samples, these processes are especially likely because the surface is extremely extended, and thermal insulation of the thin filaments can lead to local heating of the material as a result of energy release in the reaction mentioned. The disappearance of the observed CEL structure is probably due to the migration of antimony into the interior volume of the sample, i.e., surface or volume diffusion. It is well-known that the crystal lattice of Al_3Ni is very open and interstitial diffusion is quite likely to occur. Diffusion along grain boundaries, i.e., along the aluminum matrix and Al_3Ni filaments, also cannot be ruled out.

In summary, the deposition of an antimony layer has an extremely strong effect on the surface activity of a eutectic composite in the aluminum–nickel system and can be used to control its surface properties.

[1] Y. Fukui and K. Takashima, in *3-rd International Symposium on Structural and Functional Gradient Materials*, Laussane, Switzerland, 1994, p. 293.
[2] H. M. Dunlop and M. Benmalek, J. Physique IV, Colloque C6, 7, C6–163 (1997).
[3] G. Cubiotti *et al.*, J. Phys.: Condens. Matter **8**, 2549 (1996).
[4] Cheng-Min Lee and Chin-Hsiung Liao, Jpn. J. Appl. Phys., Part 1 **35**, 5448 (1996).
[5] J. L. Robins and J. B. Swan, Proc. Phys. Soc. **76**, 857 (1960).
[6] Y. Huttel, P. Soukiassian, P. S. Mungat, and Z. Hurych, Surf. Sci. **352–354**, 845 (1996).
[7] E. J. Petit and R. Caudano, Appl. Surf. Sci. **46**, 357 (1990).

Translated by M. E. Alferieff

Optical absorption in $Gd_3Ga_5O_{12}$ epitaxial films grown from $PbO-B_2O_3$ based fluxed solution

V. V. Randoshkin, N. V. Vasil'eva, A. M. Saletskiĭ, and N. N. Sysoev

M. V. Lomonosov Moscow State University, 119899 Moscow, Russia;
Joint Self-Supporting Magneto-Optoelectronics Laboratory, Institute of General Physics of the Russian Academy of Sciences, N. P. Ogarev Mordovian State University
(Submitted March 24, 1999)
Pis'ma Zh. Tekh. Fiz. **25**, 18–22 (September 12, 1999)

We report the observation of additional optical absorption in single-crystal garnet films with the nominal composition $Gd_3Ga_5O_{12}$, grown by liquid-phase epitaxy from a supercooled fluxed solution based on $PbO-B_2O_3$. © *1999 American Institute of Physics.* [S1063-7850(99)00409-7]

It has been observed[1] that single-crystal garnet films (SGFs) with a variety of compositions grown successively under identical conditions by liquid-phase epitaxy on $Gd_3Ga_5O_{12}$ (GGG) substrates from a supercooled fluxed solution based on $PbO-B_2O_3$ change color.

To determine the reasons for this effect, in the present work we studied the optical transmission of $Gd_3Ga_5O_{12}$ SGFs grown on (111) GGG substrates from a $PbO-B_2O_3$ based fluxed solution.

The composition of the charge was characterized by the following molar ratios:

$$R_1 = Ga_2O_3/Gd_2O_3 \approx 14.4,$$

$$R_2 = PbO/B_2O_3 \approx 16.0,$$

$$R_3 = (Gd_2O_3 + Ga_2O_3)/(Gd_2O_3 + Ga_2O_3 + PbO + B_2O_3) \approx 0.08.$$

The fluxed solution was homogenized in a platinum crucible for 240 min. Next, its temperature was lowered to the growth temperature T_g in 30 min, and when the temperature was set the substrate was immersed in the fluxed solution. The SGFs were grown with the fluxed solution supercooled by $\Delta T = 20$ K. Four series of SGFs, each series containing three samples, were grown. The growth times t_g for each series were 2, 5, 10, and 20 min, and the time interval between the removal of one film and the commencement of growth of the next film was ~60 min.

In each series the first film was violet and the last film was colorless. It was also found that ~70 μm garnet single crystals, as a rule, in the form of a tetragontrioctahedron, were observed to precipitate spontaneously on the surface of the fluxed solution and platinum assembly. Just as for the epitaxial films, the first single crystals formed were violet, after which the single crystals became colorless.

The thickness h of the SGFs was determined by weighing the substrate before epitaxial growth and the film together with the substrate after growth.[1] The transmission spectrum of the films was measured with a Perkin–Elmer Lambda 900 spectrometer. The parameters of the experimental SGFs are presented in Table I.

A strong decrease of the film growth rate f_g was observed when the fluxed solution was held in the supercooled state. As a result, the thicknesses h of the SGFs grown successively in each series under identical conditions are different (see Table I). Following Ref. 1, we attribute this decrease in f_g to degradation of the saturated state of the fluxed solution, well known to occur for single crystal iron-garnet films.[2–4]

The decrease in f_g cannot be explained by evaporation of the fluxed solution,[5] since it also occurs during successive growth of a series of films, one after another, with $t_g = 2$ min ($f_g = 2.23$ μm/min for the first film in the series and $f_g = 0.47$ μm/min for the fourth film).

The transmission spectra of the GGG substrate (curves *1*) and two series of films with growth times $t_g = 2$ min (Fig. 1, curves *2–4*) and $t_g = 20$ min (Fig. 2, curves *5–7*) are displayed in Figs. 1 and 2. It is evident that the epitaxial films show additional absorption compared with the substrate, especially large for relatively thick samples (Fig. 1, curve *2*; Fig. 2, curves *5–7*). In each series of successively grown SGFs, as the number of the sample and therefore the film growth rate increase, the edge of the transmission curve shifts into the short-wavelength region. We characterized

TABLE I. The parameters of epitaxial SGFs with the nominal composition $Gd_3Ga_5O_{12}$.

Film No.	t_g, min	$2h$, μm	f_g, μm/min	$\lambda_{0.1}$, nm	λ_{max}, nm	λ_{min}, nm	I_{min}/I_{max}
1	2	5.6	2.80	359	430	552	0.89
2	2	1.5	0.75	251	–	–	–
3	2	1.1	0.55	235	–	–	–
4	5	9.5	1.90	367	425	554	0.82
5	5	4.6	0.92	297	–	–	–
6	5	2.0	0.40	241	–	–	–
7	10	35.9	3.59	385	425	556	0.51
8	10	8.0	0.80	341	432	552	0.97
9	10	3.1	0.31	249	–	–	–
10	20	64.9	3.25	393	428	556	0.35
11	20	29.8	1.49	365	438	542	0.95
12	20	9.4	0.47	289	–	–	–

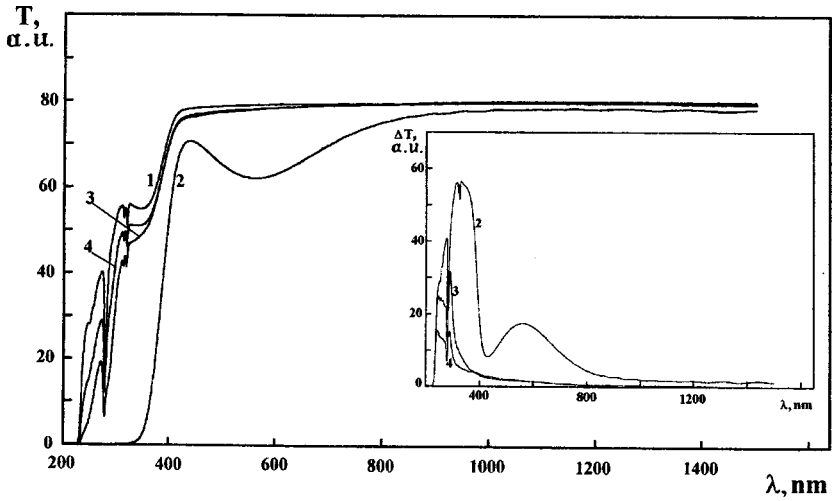

FIG. 1. Optical transmission spectra $T(\lambda)$ of the GGG substrate (*1*) and epitaxial SGFs No. 1 (*2*), No. 2 (*3*), and No. 3 (*4*). Inset: Difference spectra $\Delta T(\lambda)$ of the GGG substrate and epitaxial SGF No. 1 (*2*), No. 2 (*3*), and No. 3 (*4*).

this edge by the wavelength $\lambda_{0.1}$ (see Table I) at which the transmission T is 10% of the maximum value.

Two characteristic forms of the curves $T(\lambda)$ can be distinguished in Figs. 1 and 2. The curves *3* and *4* (Fig. 1) have the same basic features as the transmission curve of the GGG substrate (curve *1*). The curve *2* (Fig. 1) and the curves *5* and *6* (Fig. 2) have a dip near the wavelength $\lambda_{min} \approx 550$ nm. We characterize d the depth of this dip by the ratio I_{min}/I_{max}, where I_{min} is the transmission in the dip and I_{max} is the transmission in the preceding peak near the wavelength $\lambda_{max} \approx 430$ nm. The values of λ_{min}, λ_{max}, and I_{min}/I_{max} are presented in Table I. The curve *7* (Fig. 2), which does not hav a dip but does have a transmission peak at the wavelength $\lambda \approx 270$ nm characteristic for the GGG substrate falls in between.

For clarity, the difference spectra $\Delta T(\lambda)$ obtained by subtracting from the transmission spectrum of the GGG substrate the transmission spectrum of the corresponding film are presented in the insets in Figs. 1 and 2. It is evident that a wide peak centered near 560 nm, whose intensity increases with h, is characteristic for thick SGFs.

The appearance of additional optical absorption in epitaxial SGFs as compared with GGG single crystals can be explained by the fact that the films contain impurity ions. In addition, the higher the film growth rate, the higher the concentration of ions with distribution factor less than 1, specifically, nontrivalent ions Pb^{2+}, Pb^{4+}, and Pt^{4+}, in the film is. (We note that platinum ions enter the fluxed solution as a result of dissolution of the crucible material.) Specifically, the peak centered near 560 nm is most likely due to the presence of Pb^{2+}–Pb^{4+} ions in the SGFs and, in consequence, to the corresponding intervalence transitions.[3] Intraionic transitions are weaker.[3]

The existence of additional optical absorption must be taken into account in the development of new laser film materials grown by liquid-phase epitaxy from a supercooled fluxed solution.

In summary, it has been shown in this work that, first, epitaxial SGFs with the nominal composition $Gd_3Ga_5O_{12}$ grown from a PbO–B_2O_3 based fluxed solution exhibit additional optical absorption compared with the GGG substrates and, second, degradation of the fluxed solution influences this absorption.

We are sincerely grateful to A. V. Vasil'ev and V. G. Plotnichenko for assisting in the optical measurements and analysis of their results.

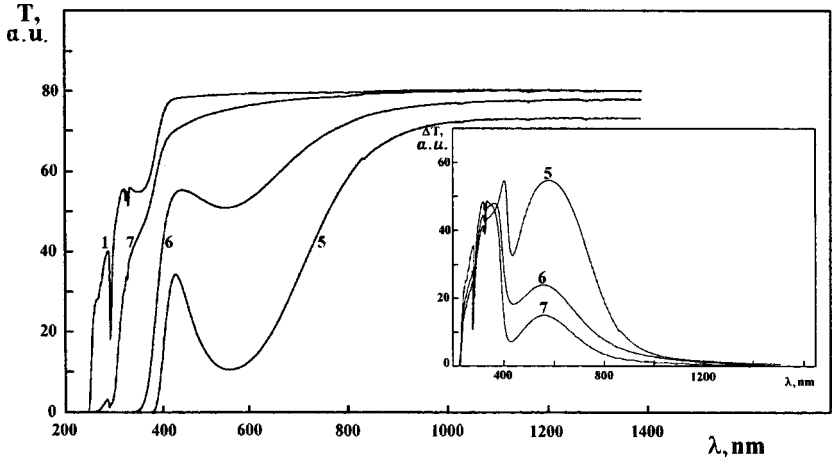

FIG. 2. Optical transmission spectra $T(\lambda)$ of the GGG substrate (*1*) and epitaxial SGFs No. 10 (*5*), No. 11 (*6*), and No. 12 (*7*). Inset: Difference spectra $\Delta T(\lambda)$ of the GGG substrate and epitaxial SGFs No. 10 (*5*), No. 11 (*6*), and No. 12 (*7*).

This work was partially supported by the Russian Fund for Fundamental Research (Grant No. 99-02-18427).

[1] V. V. Randoshkin, A. M. Belovolov, M. I. Belovolov, N. V. Vasil'ev, E. M. Dianov, K. V. Stashun, and M. I. Timoshechkin, Kvant. Elektron. (Moscow) **25**, 233 (1998).

[2] V. V. Randoshkin, N. V. Vasil'ev, K. V. Stashun, and M. V. Stashun, Neorg. Mater. **35**, 1 (1999).

[3] V. V. Randoshkin and A. Ya. Chervonenkis, *Applied Magneto-Optics* (Énergoatomizdat, Moscow, 1990).

[4] A. A. Chernov, E. I. Kivargizov, Kh. S. Bagdasarov, V. A. Kuznetsov, L. N. Dem'yanets, and A. N. Lobachev, *Modern Crystallography, Vol. 3, Formation of Crystals* (Nauka, Moscow, 1980), p. 42.

[5] B. Ferrand, B. Chambaz, and M. Couchaud, Optical Materials **11**, 101 (1999).

Translated by M. E. Alferieff

Production of ions and microdroplets in conducting-liquid emitters

I. S. Gasanov

Institute of Photoelectronics, Azerbaĭdzhan Academy of Sciences, Baku
(Submitted December 2, 1998; resubmitted March 11, 1999)
Pis'ma Zh. Tekh. Fiz. **25**, 23–28 (September 12, 1999)

The characteristics of the finely dispersed component of an electrodynamic source of indium and tin ions were studied. Microdroplets are emitted above a threshold value of the beam current, and oscillations of the ion current with a frequency of order 10 MHz are excited at the same time. At the maximum values of the ion current the microdroplet sizes range from 20 to 400 Å. The mechanisms for producing light ions and charged microdroplets in sources of this type were analyzed. These are field ionization of vapor and thermal dispersion of liquid, respectively. [S1063-7850(99)00509-1]

Although tip sources based on conducting liquids,[1–3] have long been studied in detail, a generally accepted interpretation of the processes occurring in them has still not been attained. This applies specifically to the mechanisms for the production of charged microdroplets and the excitation of oscillations of the ion current. The observed phenomena are difficult to interpret because it is virtually impossible to perform diagnostics on them, since the ion-production processes occur in micron-size regions.

In the present work, the mechanisms responsible for the formation of light ions and charged microdroplets in liquid-metal emitters are analyzed on the basis of a study of the characteristics of the finely dispersed component.

A source of indium and tin ions with current up to 150 μA and energy up to 10 keV was used in the experiments.[4] The spectra of the ion current oscillations that partially strike the extractor were recorded with an S4-25 analyzer with a transmission band of up to 60 MHz. The mass spectra were obtained using a Wien velocity filter analyzer with crossed E and H fields, (Fig. 1). The strength of the uniform magnetic field in the analyzer was 1.4 kOe, and that of the electric field between the deflecting plates was 7–20 kV/cm. A dc amplifier made it possible to fix the current of the beam components passing through the mass analyzer to the collector 8 at a value as small as 10^{-12} A.

For a gap of about 0.5 mm between the tip and the extractor, the threshold voltage for ion emission was 4–6 kV. Up to ion currents of 30–40 μA the emission is highly stable, and above this range current oscillations with a frequency of 25 MHz are excited in the beam. As the current increases continuously, stronger and lower-frequency modes appear in the spectrum in a threshold manner, and the previously excited modes remain. It is noteworthy that the frequency spectrum is discrete, i.e., not arbitrary; distinct modes develop in the system. A maximum the tin ion current of 150 μA corresponds to the minimum oscillation frequency of order 2 MHz.

Mass analysis of the composition of the beam of tin ions performed over a wide range of currents shows that the form of the spectrum as a whole remains unchanged. The ions Sn_2^+ and Sn^+ make the main contribution to the ion current. In the experiments, it was clearly observed that oscillations of the beam current arise simultaneously with the emission of charged microdroplets, corresponding to the peak in the mass spectrum in the range of small specific charges.[5] The current transported by the microdroplets is a small fraction of the light-ion current (less than 2%) and was detected using an amplifier. Calculations show that for a microdroplet specific charge $q/m = 5\times10^4$ C/kg there is one elementary charge for each 15 tin atoms, and the particle velocity in an accelerating voltage $U = 6$ kV is $v = E/H = \sqrt{2qU/m} = 2.5\times10^6$ cm/s (E and H are the electric and magnetic field strengths, respectively, in the analyzer).

To determine the sizes of the microdroplets after they settled on graphite films, the films were photographed in an electron microscope. It was found that as the beam current increases, larger particles appear in the beam and the microdroplet sizes form a continuous spectrum over a wide range from 20 to 400 Å; the number of the smallest particles is three orders of magnitude greater than the number of the largest particles, and individual particles with micron diameters are present.

It should be emphasized that the production of microdroplets does not cause an inflection in the current–voltage characteristic of the source, although mass transfer increases sharply. This shows that the emission of charged microdroplets does not destroy the process leading to the formation of light ions.

These properties of the microdroplet phase[6] allow the process of emission of charge carriers in liquid-metal sources to be interpreted as being due to overheating of the emitter. Substantial overheating of the tip in sharp sources has been noted in a number of treatments, and for a gallium-ion source the tip temperature reached 1000 °C.[7]

As the voltage rises, the sequence of processes in the source between the tip wetted with the working material and the extractor can be represented as follows.

The electric field brings the surface of the liquid to a point. This substantially increases the field near the protuberance where the curvature is small and causes breakdown of the vacuum gap with emission of light ions. The electrons produced as a result of field ionization of the vapor as well as

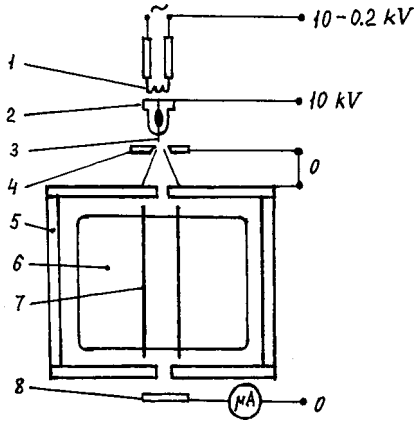

FIG. 1. Diagram of ion source with mass analyzer: *1*—cathode, *2*—container, *3*—tip, *4*—extractor, *5*—magnetic core, *6*—flat permanent magnet, *7*—deflecting plate, *8*—collector.

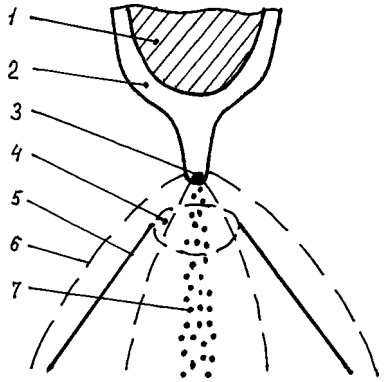

FIG. 2. Scheme of the emission of ions and microdroplets: *1*—tip, *2*—liquid, *3*—region of overheating (dispersion) of the liquid, *4*—region of ionization of vapor, *5*—beam boundary, 6—field lines, *7*—microdroplets.

the electrons knocked out by fast ions from the electrode surfaces are accelerated in the form of a sharply focused beam by the field in the direction of the tip. The local power input into the liquid excites its electronic subsystem, as a result of which the binding energy of the surface atoms decreases. For a power level of 10^6 W/cm^2, a high rate of anomalous evaporation is exhibited in phenomena such as the breakdown of vacuum insulation and ion emission from the surface of a liquid.[8] In the presence of an electrodynamic source, the field ionization coefficient

$$P(t)=1-\exp\left[-\frac{A\omega ts}{\hbar}\exp\left(-\frac{2s}{\hbar}\right)\right] \tag{1}$$

of an atom over its transit time t (Ref. 9) is close to 1. The observed values of the ion currents cannot be obtained by conventional thermal vaporization of a liquid even at 1000 °C temperature.

The deviation of the ion beam composition composition from the stoichiometric composition of the working material, the presence of vapor[10] with a high concentration of order 10^{16} cm^{-3}, and the brightly glowing region at the apex of the tip argue in favor of this mechanism of ion production due to ionization of anomalously evaporating ions in a strong electric field of order 10^8 V/cm.

As the beam current increases, the heating of the tip apex by secondary electrons increases, and when the central zone of the emitter boils up, charged microdroplets are dispersed. The continuous spectrum of microdroplet sizes is similar to the vapor bubble size distribution in a boiling liquid, expressed by the formula[11]

$$f(x)=\frac{1}{2}\sqrt{x}e^{-1/3x^{3/2}}, \tag{2}$$

where $x=R/R_0$ and R_0 is the most probable bubble radius.

The regions where ions and microdroplets form can be schematically represented as in Fig. 2. The travel distance of atoms before ionization is finite, so that the regions of production are spatially separated, which is why the CVC of the source with emission of microdroplet s is monotonic.

As the liquid boils up, the evaporation of atoms from the zone of overheating sharply intensifies. The space charge of the ions and microdroplets that builds up locally decreases the electric field near the surface of the liquid until dispersion of the liquid stops. Estimates show that the liquid tin will cool by 10 K, as a result of the removal of heat by evaporation of atoms when 10^7 W/cm^2 is introduced by electrons, in a time 9×10^{-8} s, which is comparable to the observed period of the oscillations of the ion current.

A subsequent monotonic increase of the beam current will increase in the same manner the power introduced. However, the liquid will be dispersed impulsively, since it is hot and heat is removed by the evaporated matter in a finite time. A new, more intense and low-frequency peak will appear in the spectrum of oscillations at an ion current such that the power of the electron beam is sufficient for a wider, concentric zone of the emitter to boil up. That is, the spectrum of ion-current oscillations reflects a temporal sequence of microexplosions of increasing intensity.

[1] R. Gomer, Appl. Phys. **19**, 365 (1979).
[2] D. R. Kingham and L. W. Swanson, Appl. Phys. A **34**, 123 (1984).
[3] V. E. Badan, V. V. Vladimirov, V. N. Gorshkov, and I. A. Soloshenko, Zh. Tekh. Fiz. **63**(6), 47 (1993) [Tech. Phys. **38**, 457 (1993)].
[4] M. D. Gabovich, I. S. Gasanov, and I. M. Protsenko, Zh. Tekh. Fiz. **58**, 2367 (1988) [Sov. Phys. Tech. Phys. **33**, 1442 (1988)].
[5] V. E. Badan and I. S. Gasanov, Pis'ma Zh. Tekh. Fiz. **15**(18), 49 (1989) [Sov. Tech. Phys. Lett. **15**, 724 (1989)].
[6] I. S. Gasanov, Tr. J. Phys. **20**, 1098 (1996).
[7] R. I. Hornsey and P. J. Marriot, J. Phys. D **22**, 699 (1989).
[8] V. E. Ptitsin, Rev. Sci. Instrum. **64**, 1354, 1476 (1994).
[9] E. W. Müller and T. T. Tsong, *Field Ion Microscopy, Field Ionization, and Field Evaporation* (Pergamon Press, New York, 1973; Nauka, Moscow, 1980, 220 pp.).
[10] T. Venkatesan, A. Wagner, and D. Nash, Appl. Phys. Lett. **39**, 9 (1981).
[11] V. K. Zavoĭskiĭ, At. Energ. **16**, 64 (1964).

Translated by M. E. Alferieff

Inelasticity of solids for small strains

G. G. Kochegarov

Institute of Geophysics, Siberian Branch of the Russian Academy of Sciences, Novosibirsk, Russia
(Submitted February 19, 1999)
Pis'ma Zh. Tekh. Fiz. **25**, 29–35 (September 12, 1999)

Residual (irreversible) deformations of solids were observed under very low stresses for strains $\varepsilon \approx 10^{-6}$, which in the literature are traditionally classed in the elastic region. Inelastic deformations appeared in this range for all types of solids (mono- and polycrystals of plastic and brittle materials, amorphous solids) differing strongly in nature and physicomechanical properties. These deformations can be classified as a special form of inelastic deformations—quasimicroplastic—and quasimicroplasticity can be classified as a fundamental property of solids. © *1999 American Institute of Physics.* [S1063-7850(99)00609-6]

Solids are classified as plastic and elastic. Plastic deformation divides into micro- and macroplastic. Microplastic deformation, observed in plastic metals and alloys at stresses $\sim 10^4$ times lower than their theoretical strength, is due to dislocation motion in individual microvolumes of grains, and the shear stress at which the first dislocation source is actuated is taken as the true elastic limit of the material.[1]

Materials and other dielectrics (diamond, quartz, corundum, glass) exhibit brittle properties. Specifically, quartz at room temperature is an absolutely brittle material.[2] It is believed that its yield point is close to the breaking point, so that it can deform plastically only under fracturing stresses of order 2×10^9 Pa,[3] and in the process only a thin layer of the quartz ($\ll 1$ μm)[4] along the edges of the growing fracture crack undergoes plastic deformation. Germanium and silicon cleave, as a rule, along the {111} plane without substantial preceding deformations at stress 1.5×10^8 Pa, and at 4×10^7 Pa their plastic properties appear at temperatures of 450 and 650 °C, respectively.[5]

We have observed residual (irreversible) deformations at room temperature in both plastic and brittle solids in the strain range $\varepsilon \approx 10^{-6}$, which in the literature is usually placed in the elastic region (see Fig. 1). These deformations are comparable to or greater in magnitude than the elastic deformations. Tests on the samples were performed by the three-point bending method, and the loading time was 1–2 s in the initial region of deformation and 10–15 s in the strain range $\varepsilon > 10^{-6}$. Samples were prepared in the form of $70\times 5\times 3$ mm plates. The deformation was measured by the optical-mechanical method, whose sensitivity was 5×10^{-7} (Ref. 6), and the measurement error was $\pm 50\%$ in this strain range and $\pm 10\%$ and less in the range $\varepsilon \geqslant 10^{-6}$ (as the strain increases, the measurement error decreases). The experiment was performed by the loading–unloading method with the load increased in steps. The total deformation was measured for a loaded sample, and the residual deformation was measured for an unloaded sample. No indications of creep were observed during the tests.

Figure 1 shows the results of measurements of the residual strains ε_k as a function of the stress σ for samples of various materials with different surface smoothness: polished 1 and ground 6 silicon polycrystals, glass 2, polished germanium single crystal 3, and fused quartz 4, ground silicon single crystal 5, and a sample of polycrystalline copper 7.

It is evident from the figure that the residual strains are recorded for brittle and plastic materials even with stresses $5\times 10^4 - 10^5$ in the strain range $8\times 10^{-7} - 10^{-5}$, which is traditionally placed in the elastic range.[3,5] It should also be noted that for the quartz sample only residual strains in the absence of an elastic component were observed in the initial region of loading. The stresses for which residual strains were recorded in the experimental materials are ~ 6 orders of magnitude lower than the theoretical shear strength of the material (in order of magnitude, $\tau \sim G/15$ when the direction of glide and the glide plane make an angle of 45° with the direction of the applied force;[7] here G is the shear modulus), they are ~ 4 orders of magnitude less than the yield point (equal to, for example, $\sim 2\times 10^8$ Pa for general purpose steel[8]) and their real strength, and two orders of magnitude less than the stress of microplastic flow of metals (the stress at which dislocation motion starts).

Repeated testing of the samples with no ''rest'' under identical conditions (second stage of the experiment) does not qualitatively change the picture of the ''stress–residual strain'' diagram, but the dependence $\sigma(\varepsilon_k)$ is not reproduced quantitatively; in addition, in repeated measurements of the stresses at which the previously recorded residual strain of samples was reached in the first stage shift into a higher region. The need to increase the stresses with repeated testing to achieve the residual strain recorded in the first loading shows that at this stress level the capability of material for irreversible deformation is exhausted even in the first stage. This behavior of materials under very weak stresses attests to irreversible substructural changes in their crystal lattice, and the experimental data presented suggest that the stress relaxation mechanism in our experiments is different from the microplastic strain mechanism. This conjecture is strengthened if one notes that in the range of these low stresses residual strains were recorded for typical brittle materials, such as quartz, glass, silicon, and germanium, which do not manifest plastic properties under ordinary conditions, is taken into account.

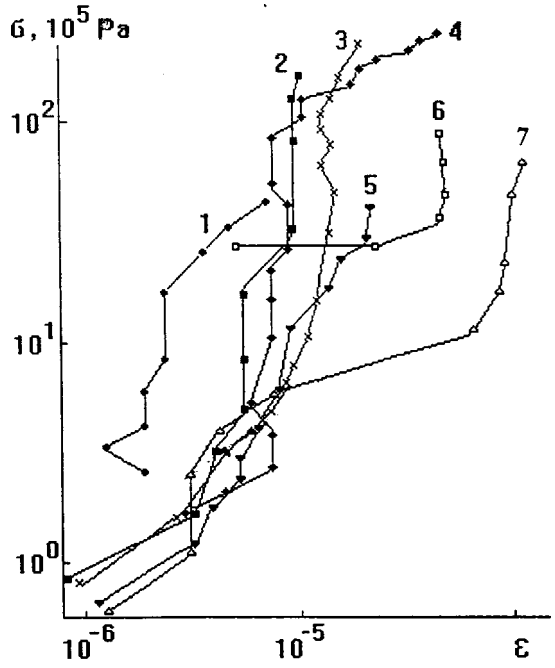

FIG. 1. Strain diagram $\sigma(\varepsilon)$, where ε is the residual strain, of materials.

In this connection, we note that according to the data of Ref. 9 the barrier for dislocation motion in metallic and ionic crystals is $10^{-3}-10^{-4}$ times lower than the interatomic bond energy and is overcome by dislocations under stresses $10^{-3}-10^{-4}$ G, while in covalent (brittle) crystals the potential barrier for dislocation motion approaches the chemical-bond energy in order of magnitude. Covalent solids have this property because the Peierls potential barrier, which dislocations must overcome in their motion, is higher than in metals. Indeed, determining the activation energy ΔW per unit length of an edge dislocation and the critical shear stress σ_c as $\Delta W \sim [Gb^2/2\pi(1-\nu)]\exp[-2\pi a/(1-\nu)b]$ and $\sigma_c \sim [2G/(1-\nu)]\exp[-2\pi a/(1-\nu)b]$, which are approximate (here b is the Burgers vector, a is the lattice constant, and ν is the Poisson ratio),[10] and substituting characteristic values for copper[5] ($G=4.9\times10^{10}$ Pa, $b=2.6\times10^{-10}$ m, $a=3.6\times10^{-10}$ m, and $\nu=0.3$), we obtain $\Delta W \sim 10^{-15}$ J/m and $\sigma_c \sim 10^6$ Pa, while for corundum[5] ($G=3.5\times10^{11}$ Pa, $b=8.3\times10^{-10}$ m, $a=4.8\times10^{-10}$ m, $\nu=0.3$) we obtain $\Delta W \sim 10^{-10}$ J/m and $\sigma_c \sim 10^{10}$ Pa. Hence ΔW for copper is five orders of magnitude smaller than in corundum, and σ_c is four orders of magnitude smaller. In Ref. 11, the same ratio was obtained for the critical stress σ_c for dislocation motion in copper and the critical stress σ of a Peierls dislocation, $\sigma_c \sim 10^{-4}\sigma$, showing that in a plastic metal the dislocation displacement stress is four orders of magnitude lower than in a covalent crystal.

The decrease in the mobility of dislocations in covalent materials can be explained by the localization and spatial directedness of their chemical bonds[7] and by the specific topology of dislocations in an energetically inhomogeneous crystal-chemical lattice. A change in their position and configuration even with a unit translational displacement can induce recombination of several interatomic bonds at the same time. These crystal-chemical features of solids with covalent bonds are responsible for the high starting stress and energy of dislocation motion in a material.

According to published data, the stresses for generation of dislocations and the stresses at which the leading dislocation stops in lithium fluoride are an order of magnitude greater, 1×10^7 Pa,[12] and a stress of order 0.03–0.05 G is required for stable growth of dislocation loops and clusters with homogeneous nucleation in germanium, while for heterogeneous nucleation an order of magnitude lower stress is required.[13] The formation of glide bands in quartz was observed in Ref. 14 at 1000 °C and 8×10^8 Pa pressure, the exposure time was up to 5 h. Translational glide in quartz parallel to the basal plane (0001) at 500–700 °C, 2×10^9 Pa pressure, and exposure time $\sim$0.5 h is described in Ref. 15. According to the data in Ref. 16 dislocations in silicon are stationary at room temperature, and in Ref. 17 it is stressed that below a certain temperature (250 °C for germanium and 600 °C for silicon) the mechanism of plastic deformation in covalent crystals changes substantially.

Thus, the residual strains observed in covalent crystals, where the critical stress for dislocation motion is approximately an order of magnitude higher than in plastic metals, point especially clearly to the specific character of the mechanism of inelastic deformations in our experiments. As a result, the residual deformation which we recorded in a solid under unusually low stresses can be characterized as a manifestation of a special type of inelastic deformation—quasimicroplasticity (QMP).

Special attention should be given to the fact that the observed QMP deformation in the initial strain range (where it is most effectively manifested) does not differ greatly in magnitude and stress level even for solids with sharply different nature and physicochemical properties, such as plastic copper and brittle covalent crystals. Such behavior of materials with QMP deformation emphasizes its special character, which gives rise to the difference between microplasticity and QMP deformation of solids, while the generality of the manifestation of QMP in brittle and plastic materials confirms the generality of its mechanism in solids with different physicochemical properties. It can be inferred that QMP deformation of solids precedes microplastic flow.

In summary, the experimental data presented above show that the QMP properties of materials have a special mechanism, different from plastic flow, and they are manifested in single and polycrystals as well as in amorphous solids. These materials possess qualitatively opposite physicomechanical properties, which are due to the difference of their nature, crystal structure, surface state, material and phase composition, degree of crystallinity, and chemical-bond structure, and on the basis of all factors examined taken as a whole the observed quasimicroplasticity can be classified as a fundamental property of solids.

[1] E. F. Dudarev, *Microplastic Deformation and the Yield Point of Polycrystals* (Tomsk Stase University Press, Tomsk, 1988) 256 pp.
[2] R. J. Stokes, *Fracture* (Academic, New York, 1972), Vol. 7, pp. 157–165.
[3] A. V. Shubnikov, *Selected Works on Crystallography* (Nauka, Moscow, 1975), pp. 359–366.

[4] G. S. Khodakov, *The Physics of Pulverization* (Nauka, Moscow, 1972) 308 pp.
[5] H. G. Van Bueren, *Interfections in Crystals* (North-Holland, Amsterdam, 1960) 624 pp.
[6] L. I. Tushinskiĭ and A. V. Plokhov, *Study of the Structure and Physical–Mechanical Properties of Alloys* (Nauka, Novosibirsk, 1985) 200 pp.
[7] P. V. Pavlov and A. F. Khokhlov, *The Physics of Solids* (Vyssh. Shkola, Moscow, 1985) 384 pp.
[8] Yu. A. Geller and A. G. Rakhshtadt, *Materials Science* (Metallurgiya, Moscow, 1989) 456 pp.
[9] *Encyclopedic Physics Dictionary*, edited by A. M. Prokhorov (Sov. Éntsiklopediya, Moscow, 1983) 928 pp.
[10] J. Friedel, *Dislocations* (Pergamon Press, New York, 1964) 653 pp.
[11] A. H. Cottrell, *Theory of Crystal Dislocation* (Blackie and Son Ltd., London, 1964) 103 pp.
[12] R. I. Garber and V. M. Mikhaĭlovskiĭ, Fiz. Tverd. Tela (Leningrad) **14**, 1557 (1972) [Sov. Phys. Solid State **14**, 1342 (1972)].
[13] V. P. Alekhin, V. I. Eremenko, and E. I. Mal'tina, *Metallic Single Crystals* (Nauka, Moscow, 1990), pp. 109–117.
[14] I. S. Delitsin and A. G. Zhabin, Dokl. Akad. Nauk SSSR **234**, 433 (1977).
[15] E. V. Tsinzerling, ZVMO, Ch. 986, 213 (1969).
[16] J. Dash, *Dislocations and the Mechanical Properties of Crystals* (Inost. Lit., Moscow, 1960), pp. 315–362.
[17] V. I. Trefilov and Yu. V. Mil'man, Dokl. Akad. Nauk SSSR **153**, 824 (1963) [Dokl. Akad. Nauk SSSR **8**, 1240 (1964)].

Translated by M. E. Alferieff

Josephson effect in a metal–polyimide-film–metal structure

A. N. Ionov, V. A. Zakrevskiĭ, and I. M. Lazebnik

A. F. Ioffe Physicotechnical Institute, Russian Academy of Sciences, St. Petersburg, Russia;
B. P. Konstantinov Institute of Nuclear Physics, Russian Academy of Sciences, Gatchina, Russia
(Submitted May 27, 1999)
Pis'ma Zh. Tekh. Fiz. **25**, 36–43 (September 12, 1999)

It is shown that in metal–polyimide-film–metal sandwich structure a conducting state arises in a zero electric field when a reliable electric contact is established between the metal and polyimide film. The Josephson effect is observed with superconducting electrodes in weak magnetic fields, attesting unequivocally to the existence of superconductivity in the polyimide film.
 [S1063-7850(99)00709-0]

It was first reported in Ref. 1 that metal–polyimide-film–metal (Me–PF–Me) in sandwich structure a technical zero of the resistance is detected if the metallic electrodes are in a superconducting state. It was concluded that the polymer interlayer itself possesses conductivity higher than that of nonsuperconducting metals. Atactic polypropylene preirradiated with UV light at high temperature was used as the object of investigation. As a result of intense photothermooxidative destruction occurring under these conditions, the molecular structure of the organic interlayer was indefinite. Moreover, a high-conductivity state was detected at electric field strengths $E=10^2-10^3$ V/cm, i.e., under conditions such that some authors admit intergrowth of a metallic dendrite from electrode to electrode as a result of ion transport.[2] These circumstances, specifically, the impossibility of reliably characterizing the object together with the effect of a comparatively strong field, made the result of Ref. 1 unconvincing.

These doubts were removed in Ref. 3. It was established there that for a thin (approximately 1 μm thick) polyphthalidylidene biphenylene film inserted between two metallic electrodes, the existence of a high-conductivity state without the application of an electric field is characteristic. For this polymer, just as in the case described in Ref. 1, a technical zero of resistance was recorded with a transition of the electrodes from the normal to the superconducting state. It was shown that the high-conductivity state is an intrinsic property of metal–polymer film–metal structures.

It became obvious that there is a need for new data on the conditions under which the superconducting state arises in Me–PF–Me structures and to determine their conductivity.

Polyimide was chosen as the object of investigation. Polyimides comprise a wide class of polymers characterized by high thermal stability (up to 700 K), high radiation resistance, and stiffness (the elastic modulus reaches 1000 kg/mm^2). Just as in Ref. 1, in Me–polyimide–Me structures 1) the conducting state arose after an electric field $E<10^3$ V/cm was applied and 2) at low, liquid-helium, temperatures a technical zero of resistance was observed after the electrodes passed into the superconducting state.[4]

Films of thickness 0.7–3.0 μm were prepared by depositing drops of a 20% solution of sulfoxidianiline on the polished surface of one of the electrodes, followed by centrifuging, as a result of which the solution spread out uniformly over the surface of the metal. Then the film was held for 2 h at $T=330$ K to remove the solvent, after which imidization was performed at $T=450$ K.

Massive tin and niobium of at least 99.99% purity were used as electrode materials. An MII-4 interference microscope was used to monitor the quality of surface polishing. The surface irregularities was less than 0.08 μm. The electrode diameters were 10 and 3 mm. The polyimide film investigated was deposited on the electrode of larger diameter. The other electrode was clamped to the polymer film with a small force. To obtain more uniform clamping and to prevent bending, the clamped electrode was pressed into a ring, made of a dielectric material, with inner and outer diameters of 3 and 10 mm, respectively, in such a manner that the electrode and the nonconducting outer ring formed a single clamping surface. The series of sandwich structures had a 0.7–1.4 μm thick bounding ring made of a nonconducting material. The inner 2 mm in diameter opening with a diameter of 2 mm was filled with the polyimide under study. The sandwich structures were constructed so as to prevent the electrodes from coming into direct contact with one another.

The appearance of a conducting state in the sandwich structure was detected with a digital voltmeter with a high input resistance, i.e., in the same way as in Ref. 3. When the conducting polymer was connected to the input of the digital voltmeter, its noise voltage dropped sharply. Under these conditions detection of a conducting state in a zero electric field becomes possible.

It was established experimentally that the conducting state in Me–PF–Me structures arises for films of thickness $d<1.5$ μm over a wide temperature range from 77 to 500 K. This rules out a model whereby a metallic dentrite forms between electrodes by an ionic mechanism,[2] since 1) there is no ionic current in the absence of an electric field and 2) there are no electrolytes that would not freeze at the boiling temperature of liquid nitrogen.

It has been remarked in a number of publications[5,6] that a conducting state arises in polymer films only after a uniaxial mechanical pressure has been applied. A theoretical

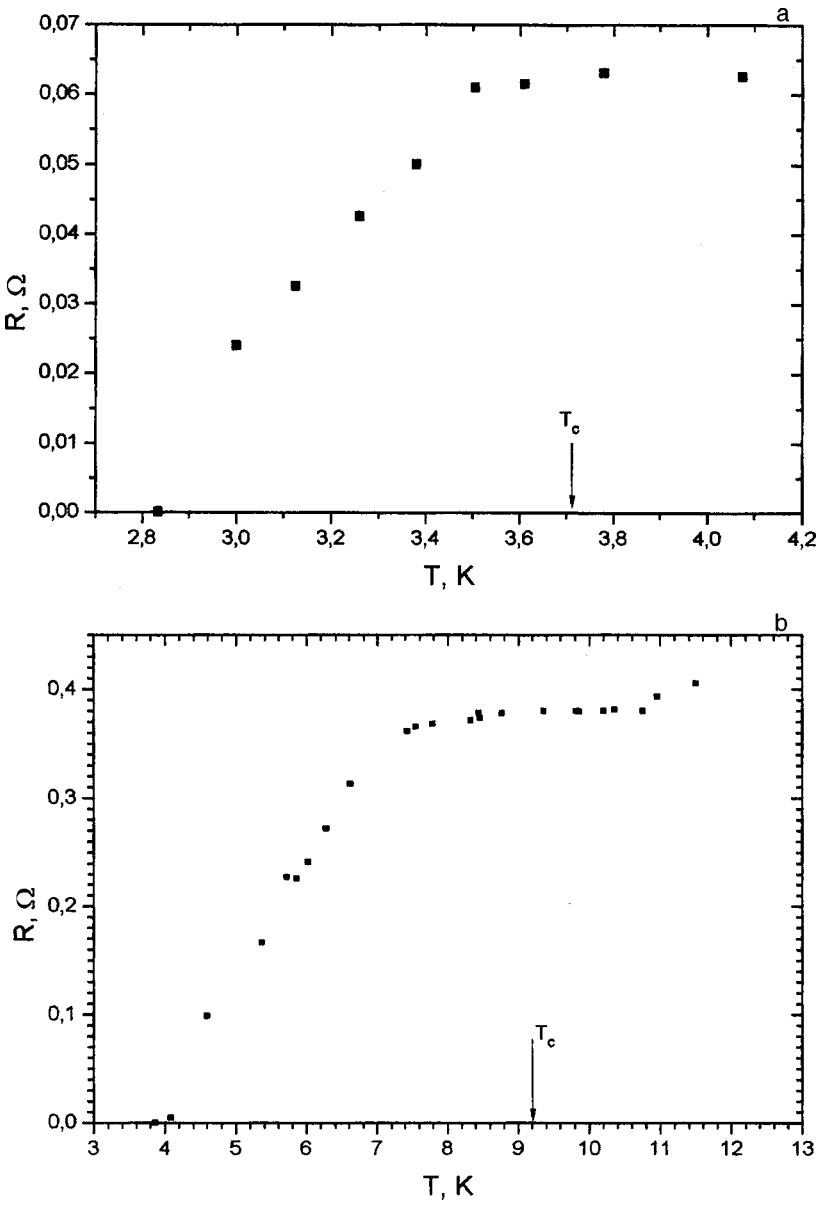

FIG. 1. Temperature dependence of the resistances of Sn–PF–Sn (a) and Nb–PF–Nb (b) sandwich structures with current less than 100 μA through the structure.

model where the mechanical pressure plays a key role in the formation of the conducting state has been proposed in Ref. 7. However, it should be noted here that in all experimental work a small threshold pressure, less than 10^5 Pa, was observed. Such a weak pressure is hardly likely to bring about changes in the molecular and supermolecular structures of the film or any substantial deformation. In this connection, it was proposed in Ref. 3 that the only role of mechanical pressure is to ensure a reliable electrical contact between the polymer film and the electrode. To check this supposition the following experiments were performed.

A droplet of liquid gallium[1)] with volume less than 1 mm^3, which wetted an area of at least 10^4 μm^2 on the surface of the polymer, was deposited on the free surface of the polymer in a metal–polymer structure. As soon as the needle electrode touched the top of the gallium droplet, using a micrometric vertical manipulator, the electric circuit (metal–polyimide-film–liquid-gallium-drop–needle-electrode) was closed and the voltmeter instantaneously detected a conducting state. The load on the polymer in these experiments was so small that there is no sense in talking about it influencing the properties of the film. On the other hand, the liquid metal provided a good electric contact with the film. We also note that when tin was used as the bottom electrode, liquid gallium was also a good indicator of quality of the polymer coating, because in the presence of hollow channels through the polymer film gallium will wet the Sn bottom electrode and form with it a eutectic alloy Sn–Ga. After the polymer coating on the polished surface of the tin electrode is removed with an organic solvent, craters should be observed at the locations of the channels in the polymer coating. In our case, the quality of the electrode surface did not change after such a procedure, indicating good uniformity of the polymer film.

In some experiments a 0.4 μm thick and 2–3 mm in diameter electrode, obtained by vacuum depositing gold on the polyimide surface, was used instead of a clamped, massive electrode. The deposited electrode, whose weight could

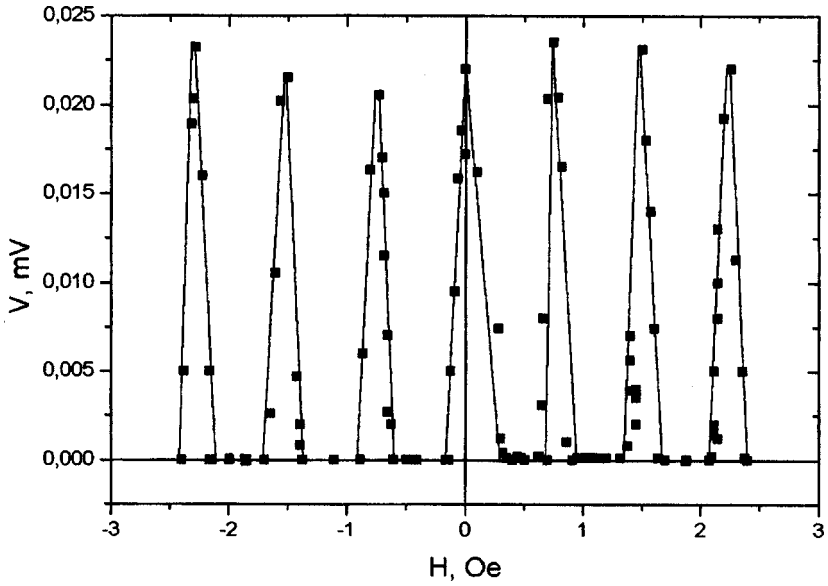

FIG. 2. Voltage drop V versus the magnetic field H for a structure Nb–PF–Sn structure at temperature $T=2.83$ K with current $I \geqslant I_c = 163\ \mu$A through the sandwich structure.

be neglected, also provided a good electric contact, and the conductivity of the structure was recorded without applying mechanical pressure.

The data obtained confirm the conjecture, made previously in Ref. 3, that mechanical pressure is merely a means for providing a reliable electric contact between the electrode and the polymer.

We now turn to investigation of low-temperature phenomena in the Me–PF–Me structure. The voltage V on the sandwich structures was measured by means of a four-probe method using SHCH300 and V2-36 digital voltmeters with constant current, which was set by a large load resistance. Temperatures below 4.2 K were obtained by evacuating helium vapors, and it was fixed with a monostat to within 0.01 K. A temperature above 4.2 K was obtained by heating helium vapors with a microheater, and it was measured with a conventional TSG-1 germanium thermometer.

Figures 1a and 1b show the low-temperature variation of the resistances R for Sn–PF–Sn (a) and Nb–PF–Nb (b) structures. It is well known that tin passes into a superconducting state at temperature $T_c = 3.72$ K and niobium at $T_c = 9.2$ K. As one can see from the figure, when our sandwich structures are cooled, an appreciable decrease of resistance is first observed at T_c, which continues down to technical zero, determined by the resolution limit of the apparatus employed. It is also evident from the figure that for Sn–PF-Sn (a) and Nb–PF–Nb (b) the transition to technical zero is observed in temperature ranges of 0.9 and 4 K, respectively. When no polyimide was present between the metallic electrodes and the electrodes directly touched one another, the transition to technical zero of the resistance on cooling occurred extremely sharply, which confirms that the purity of the metals employed as electrodes was quite high. On the basis of the classical theory of superconductivity the diffuseness of the transition could indicate fluctuation phenomena near the critical temperature T_c. According to the theory (see, for example, Ref. 8), near T_c order-parameter fluctuations give rise to a resistance in the superconducting state at $T < T_c$ and superconducting electrons at $T > T_c$. In pure massive superconductors such fluctuations do not appreciably affect the character of the superconducting transition. In contrast to this, in two- and one-dimensional superconductors such fluctuations should wash out the transition in temperature. Such behavior is indeed observed in thin superconducting filaments and particles with diameter $d \ll \xi_0$—the coherence length.

Tin and niobium have $\xi_0 \simeq 2500$ and $\xi_0 \simeq 600$ Å, respectively. Hence it follows that if the gradual temperature transition to technical zero of the resistance which we observed is due to the existence of superconducting electrodes in the polyimide, then the effective diameter of all superconducting polymer channels should be much smaller than 2500 Å for Sn electrodes and 600 Å for Nb electrodes. In this case, the sandwich structures investigated should be systems generally referred to as ''weak links.'' As is well known, a weak link is a region where the critical current is much lower than in the superconductors linked by it.[2)]

This region can be formed by a bridge with a small cross section consisting of a superconductor, a point contact between two superconductors or a normal metal where superconductivity has appeared as a result of the ''proximity'' effect. In our case a low critical current could be due either to induced superconductivity in the polymer channel, as happens in superconductor–normal metal–superconductor structures,[9] or point contacts between the ends of a superconducting polymer channel and the superconducting electrodes. In the latter case the superconductivity of the polymer channel cannot be due to the superconductivity of the metallic electrodes, and the mechanism leading to the appearance of superconductivity can be different from classical superconductivity, which is due to a weak interaction. The observed smearing of the transition is due to the properties of the polymer film. However, in any case, in the presence of a weak link a stationary Josephson effect should be observed, i.e., oscillations of the critical current in weak magnetic fields (see, for example, Ref. 10). To check this supposition we investigated the dependence $V(H)$ in weak magnetic fields for the same current, transverse to the magnetic field,

flowing through an Nb–PF–Sn structure for which a voltage drop is recorded on the sandwich structure. Figure 2 shows the observed dependence $V(H)$, clearly indicating oscillation of the critical superconducting current.

In summary, it has been established that: 1) in a thin polyimide film inserted between two metallic electrodes, a conducting state arises in a zero electric field when a reliable electric contact is established between the metal and the polyimide film and 2) when the electrodes pass into the superconducting state a Josephson effect is observed in Me–PF–Me structures, unequivocal evidence that the thin polyimide film is superconducting.

In closing, we thank V. M. Sarygina and V. A. Ionov for assisting in this work.

[1)]The experiment was performed at a temperature higher than the melting temperature of gallium (29 °C) and under conditions ruling out the formation of gallium oxide films.

[2)]This region can be formed by a bridge with a small cross section consisting of a superconductor, a point contact between two superconductors or a normal metal where superconductivity has appeared as a result of the ''proximity'' effect.

[1] V. M. Arkhangorodskiĭ, A. N. Ionov, V. M. Tuchkevich, and I. S. Shlimak, JETP Lett. **51**, 67 (1990).
[2] N. V. Agrinskaya and V. I. Kozub, Solid State Commun. **106**, 111 (1998).
[3] V. A. Zakrevskiĭ, A. N. Ionov, and A. N. Lachinov, Pis'ma Zh. Tekh. Fiz. **24**(13), 89 (1998) [Tech. Phys. Lett. **24**, 539 (1998)].
[4] A. M. El'yachevich, A. N. Ionov, M. M. Rivkin, and V. M. Tuchkevich, Fiz. Tverd. Tela (Leningrad) **34**, 3457 (1992) [Sov. Phys. Solid State **34**, 1850 (1992)].
[5] A. Yu. Zherebov and A. N. Lachinov, Synth. Met. **44**, 99 (1991).
[6] A. M. El'yashevich, A. N. Ionov, V. V. Kudryavtsev *et al.*, VMS **35**(1), 50 (1993).
[7] O. A. Ponomarev and E. S. Shikhovtseva, Zh. Éksp. Teor. Fiz. **107**, 637 (1995) [JETP **80**, 346 (1995)].
[8] P. Hohenberg, Paper at the 11th International Conference on Low-Temperature Plasma, Scotland, August 1968.
[9] T. Y. Hsiang and D. K. Finnemore, Phys. Rev. B **22**, 154 (1980).
[10] L. Solymar, *Superconductive Tunneling and Applications* [Chapman and Hall Ltd., London, 1972; Mir, Moscow, 1974, p. 428].

Translated by M. E. Alferieff

Mechanical behavior of porous zirconium dioxide under active deformation by compression

S. P. Buyakova, Han Wei, Li Dunmy, Chen Haiyun, T. Yu. Sablina, A. G. Mel'nikov, and S. N. Kul'kov

Institute of Physics of Strength and Materials Science, Siberian Branch of the Russian Academy of Sciences, Tomsk, Russia;
Dzilin University, Changchun, 130023 China
(Submitted February 15, 1999)
Pis'ma Zh. Tekh. Fiz. **25**, 44–48 (September 12, 1999)

The properties of the mechanical behavior of porous ceramic based on partially stabilized zirconium dioxide are studied. The special features of the mechanical behavior of ceramic with different degrees of porosity are determined. It is shown that three macrodeformation mechanisms are observed simultaneously in the material: elastic deformation characteristic of compact material; microcracking with accumulation of microdefects; and displacement of local volumes of material into the pore space. A ceramic with porosity less than 20% retains its capacity for transformational changes in the stress field of a propagating crack. © *1999 American Institute of Physics.* [S1063-7850(99)00809-5]

Ceramics based on partially stabilized zirconium dioxide are of great interest as high-viscosity ceramic materials.[1,2] In addition, they are promising as materials containing a controllable number of pores but at the same time retaining the strength characteristics determined by transformation hardening. This could be helpful, for example, for biomaterials, filters, heat-shielding structures, and so on.[3] However, there are no data on the influence of porosity on the mechanical properties.

The objective of the present work is to investigate the effect of porosity on the mechanical behavior of zirconium dioxide based ceramic under active deformation by compression.

A porous ceramic based on ultradispersed zirconium dioxide powder, stabilized with 3 molar% Y_2O_3, was studied. Samples of the material were prepared by the power metallurgy method by pressing and then sintering ZrO_2 in the temperature range 1200–1600 °C. Varying the sintering time from 10 min to 10 h caused the final porosity to vary over the range 10–60%. Compression tests on the samples were performed in an INSTRON-1185 testing machine with a constant loading rate of $3\times10^{-4}\,s^{-1}$. The strength and relative deformation of the material were determined.

Figure 1 shows stress–strain diagrams of ceramics with different degrees of porosity. As one can see from the figure, in the loading diagram for the pore-free ceramic (porosity less than 2%) the material fractures essentially from the elastic region, and there is a small section corresponding to nonlinear elasticity or, possibly, tetragonal–monoclinic structural transformation.[1]

As porosity increases, multiple microdefects appear in the course of deformation, and the number of defects increases with the degree of porosity. This process appears in the loading diagram as sharp drops of the stress as a result of microcracking. Microcracks stop at pores and the material regains its capability for elastic deformation.

The microcracking process is accompanied by displacement of local volumes of material into the pore space, so that an increase in porosity results in the appearance of quasiplasticity as a result of additional compaction of the material.

Thus, three macrodeformation mechanisms are observed simultaneously in the material: the elastic deformation characteristic of compact material; microcracking with accumulation of microdefects; and displacement of local volumes of material into the pore space. This is most clearly illustrated in Fig. 2, where the relative coordinates $\sigma/\sigma_{max}=f(\varepsilon/\varepsilon_{max})$ are used. As porosity increases, the region of microcracking observed in the loading diagram as sharp drops in stress

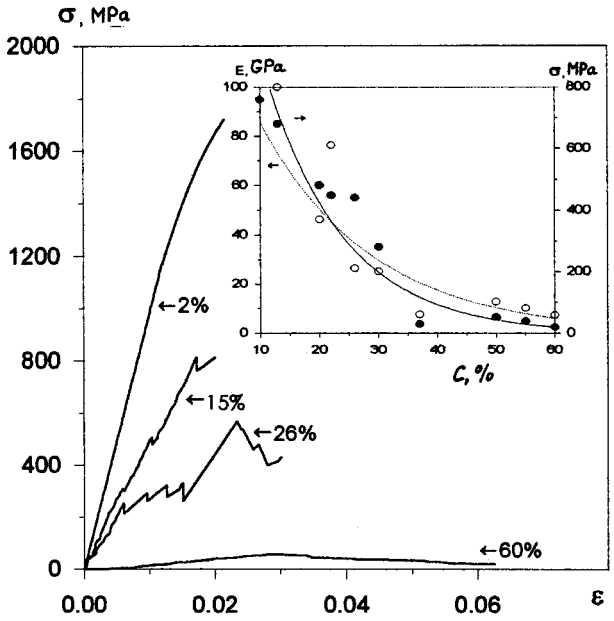

FIG. 1. Curves of deformation of ZrO_2 based ceramic with different degrees of porosity. Inset: Variation of the strength and elastic modulus with increasing porosity.

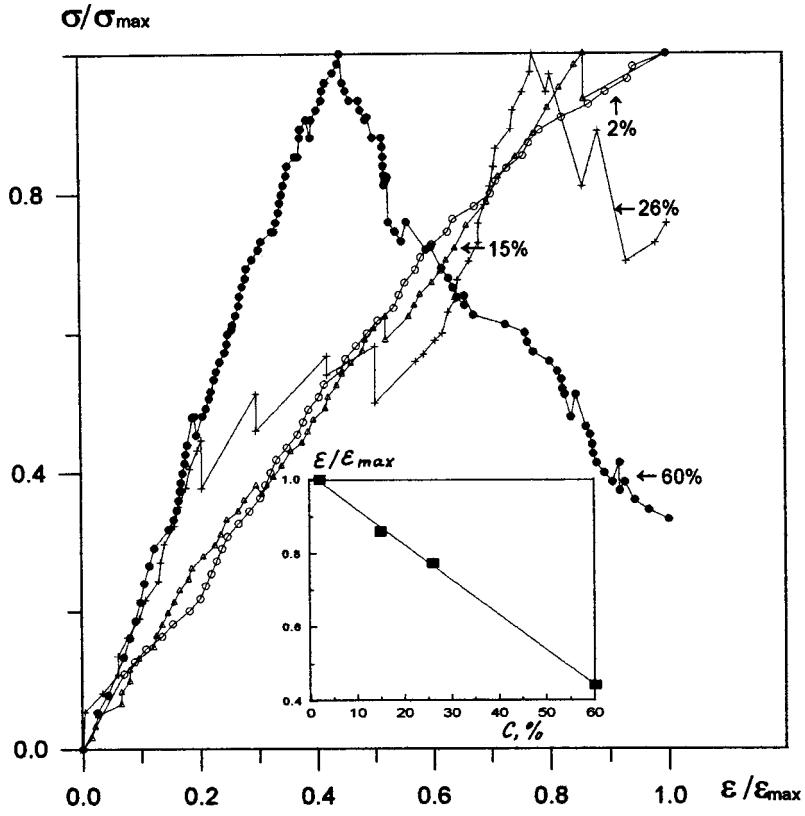

FIG. 2. Curves of deformation of ZrO_2 based ceramic in relative coordinates. Inset: Variation of the relative strain $\varepsilon/\varepsilon_{\max}$ with increasing porosity.

shifts into the region of smaller relative deformations and becomes more extended. Characteristically, the relative strain $\varepsilon/\varepsilon_{\max}$ at which the stresses reach their maximum values (i.e., $\sigma/\sigma_{\max}=1$) decreases linearly with increasing porosity (inset in Fig. 2).

The inset in Fig. 1 shows the dependence of the strength and elastic modulus on the degree of porosity. Fitting functional dependences of the form $Y=A\exp(b\cdot X)$ (Ref. 4) to the experimental values gave 1200 MPa and 200 GPa, respectively, for the strength and elastic modulus of pore-free material, in good agreement with the published data.[5]

The results of x-ray crystallographic analysis of the samples, performed with a Dron-UM1 diffractometer using FeKα radiation, showed that in its initial state the ceramic is in a tetragonal phase. Under loading a structural transformation, typical of these materials, from the tetragonal to the monoclinic phase on the fracture surface, is observed only for low porosity, because quasiplastic deformation of these materials starts at low stresses. Indeed, an estimate of the concentration of internal stresses, following Ref. 4, in the form

$$E/E_0=\sigma/\sigma_1,$$

where E is the elastic modulus, E_0 is the elastic modulus of the pore-free material, σ is the applied stress, and σ_1 is the local stress, showed that stresses sufficient for a phase transformation (>200 MPa according to Ref. 6) arise only in material with porosity less than 20%. In ceramic with higher porosity the local stresses decrease sharply and do not reach a high enough level for a phase transformation.

In summary, three macrodeformation mechanisms are observed simultaneously in porous ceramic material: elastic deformation characteristic for compact material; microcracking with accumulation of microdefects; and displacement of local volumes of material into the pore space. A ceramic with porosity not exceeding 20% retains its capacity for transformational changes in the stress field of a propagating crack.

[1] D. F. Kalinovich, L. I. Kuznetsova, and É. T. Denisenko, Poroshkovaya Metallurgiya, No. 11, 98 (1987).
[2] A. G. Evans and R. M. Cannon, Acta Metall. **34**, 761 (1986).
[3] *Porous Structural Ceramic*, edited by Yu. L. Krasulin (Metallurgiya, Moscow, 1980).
[4] R. L. Coble and N. M. Parikh, *Fracture*, Vol. 7 (Mir, Moscow, 1976).
[5] A. R. Andrievskiĭ and I. I. Spivak, *Handbook of the Strength of Refractory Compounds and Materials Based on Them* (Metallurgiya Press, Chelyabinsk, 1989).
[6] D. B. Marshal and M. R. James, J. Am. Soc. **69**, 3 (1986).

Translated by M. E. Alferieff

Deformation stability of a flat domain wall in magnetic films

Yu. I. Gorobets, Yu. F. Vilesov, and N. A. Groshenko

Simferopol' State University
(Submitted July 20, 1998; resubmitted May 18, 1999)
Pis'ma Zh. Tekh. Fiz. **25**, 49–56 (September 12, 1999)

The forces determining the orientation of domain walls in films of magnetooptic materials with a figure of merit of order unity are studied. The behavior of small perturbations of the position of a flat domain wall in the presence of an in-plane component of the anisotropy vector is analyzed. The forces arising when the orientation of the domain wall deviates from the easy-magnetization axis and striving to return the wall to its initial state are conventionally represented as a gradient ''effective magnetic field.'' The forces exerted by the ''effective field,'' due to the in-plane component of the anisotropy vector, on the perturbed domain wall are calculated. The orientational stability conditions for a planar domain wall are found. An explanation is given for the experimentally observed predominant orientation of striped domains.
 [S1063-7850(99)00909-X]

A labyrinthine domain structure is formed in films of a magnetooptic material with anisotropy axis perpendicular to the film plane and figure of merit of order unity, $q = H_k/4\pi M_s \geqslant 1$, in the absence of external magnetic fields and anisotropy axis in the film plane. It appears because the domain wall, as an analog of a conductor with a current, is unstable with respect to bending deformations.[1–3] The magnetic field resulting from a small deformation of a conductor carrying a current strives to increase this deformation. Ultimately, straight domain walls are energetically unfavorable compared with curved walls. This is what gives rise to a labyrinthine domain structure.

The existence of a component of the anisotropy field in the film plane has the effect that the magnetization vector in the domains turns under the action of this field through an angle relative to the normal. This rotation of the magnetization vector in domains decreases the angle of rotation of the magnetization vector in domain walls oriented along the anisotropy field and decreases the energy of domain walls. An orientation of striped domains along the anisotropy field becomes energetically favorable.

To analyze the question of the bending instability of a flat domain wall we shall calculate the total energy of a sinusoidally perturbed domain wall in an effective magnetic field with a constant gradient (Fig. 1a). Rotation of a domain wall relative to the easy-magnetization axis will increase the specific energy of the domain wall and result in the appearance of certain compensating forces which strive to return the wall to the initial state. In solving the problem, these elastic forces can be replaced by an effective gradient magnetic field. The magnitude of these forces and, correspondingly, the effective gradient magnetic field for a sinusoidally perturbed wall are proportional to the ratio $H_z \sim 2B/\Lambda$, where B is the amplitude of the sinusoidal perturbation of the domain wall and Λ is the period of the sinusoidal perturbation.

We also assume that the uniaxial anisotropy field is much greater than the in-plane component of the anisotropy field, and the contribution of the in-plane anisotropy to the total energy of the system is taken into account completely by the effective magnetic field which we have introduced. We shall assume that the effective magnetic field is perpendicular to the film surface and is zero in the initial (unperturbed) state of the planar domain wall. For perturbations with constant period Λ the field varies along the x axis as

$$H_z(x) + \alpha x/\Lambda, \tag{1}$$

where α is a constant, which depends on the ratio between the in-plane and normal components of the anisotropy field. The equilibrium position of the wall for $\alpha > 0$ corresponds to the coordinate $x = 0$.

The change in energy of the domain structure in the effective magnetic field due to the bending of the wall is

$$\Delta W_H = 4M_s \frac{\alpha}{\Lambda} t \frac{L_y}{\Lambda} \int_S x dS, \tag{2}$$

where t is the thickness of the magnetic film, L_y/Λ is the number of bends of the domain wall, and the integration extends over the area S of a half-period of the wall (Fig. 1a). The integral in Eq. (2) can be calculated as

$$\int_S x dS = \int_0^{\Lambda/2} dy \int_0^{B \sin ky} x dx = \frac{\pi B^2}{4k}, \tag{3}$$

where $k = 2\pi/\Lambda$. Thus,

$$\Delta W_H = \frac{M_s B^2 \alpha t L_y}{2\Lambda}. \tag{4}$$

Next, we use the well-known formulas for the surface energy of a domain wall as a function of its surface density σ:

$$\Delta W_s = \sigma \frac{2tL_y}{\Lambda} \int_0^{\Lambda} dy \left(\sqrt{1 + B^2 k^2 \cos ky} - 1 \right)$$

$$\approx \frac{\sigma t B^2 k^2 L_y}{4} \tag{5}$$

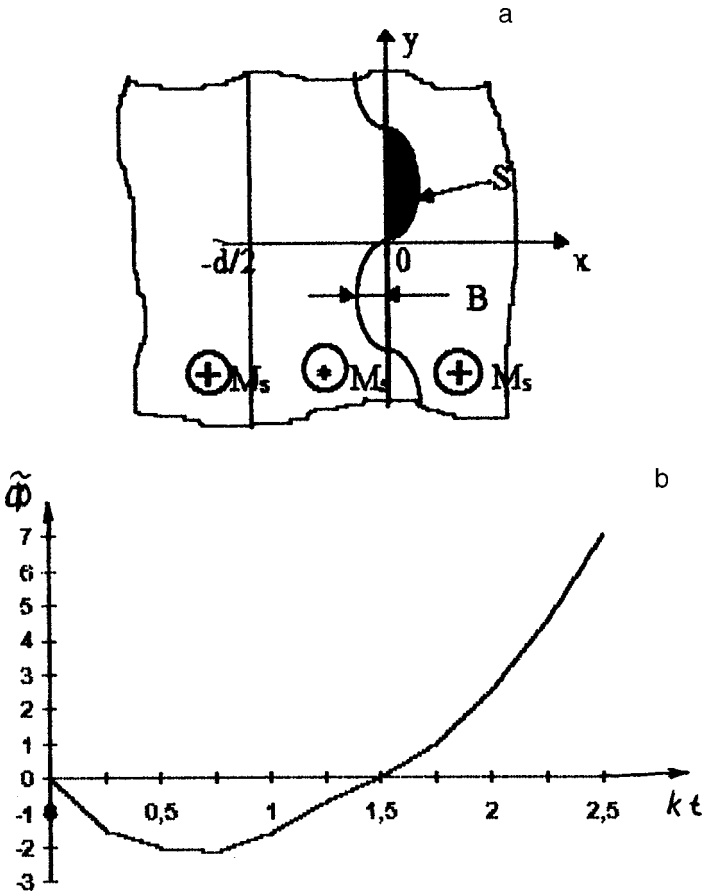

FIG. 1. a—Striped domain with one flat and one sinusoidally perturbed wall. b—Qualitative behavior of the function $\tilde{\Phi}(kt)$.

and the magnetostatic energy of a sinusoidally deformed wall for $d=\infty$:

$$\Delta W_M = -4M_s^2 L_y B^2 \left\{ K_0(kt) + \gamma - \ln \frac{kt}{2} \right\}, \tag{6}$$

where $\gamma = 0.5772$ is Euler's constant and K_0 is a modified Bessel function.[3]

Summing all types of changes in the energy of a deformed wall we obtain

$$\Delta W_M = 4\pi M_s^2 L_y B^2 \left[\tilde{\Phi}(kt) + \frac{\alpha t}{8M_s \Lambda} \right]. \tag{7}$$

Here

$$\tilde{\Phi}(kt) = \frac{\sigma (kt)^2}{16 M_s^2 t} - \gamma + \ln \frac{kt}{2} - K_0(kt). \tag{8}$$

Analyzing the expression (7), taking into account the graphical dependence of $\tilde{\Phi}$ on kt (Fig. 1b), we conclude that in the absence of a gradient field ($\alpha = 0$) a flat domain wall in a uniaxial film is always unstable relative to an increase in the deformation amplitude B, since in this case the increment ΔW in the energy becomes negative. The minimum value of the gradient field α/Λ for which a flat domain wall is still stable can evidently be found from the condition that the energy increment ΔW with the minimum possible value of the function $\tilde{\Phi}$ vanishes. This is determined by the relations

$$\frac{\alpha}{\Lambda} = \frac{8M_s}{t} \left[K_0(kt) + \ln \frac{kt}{2} + \gamma - \frac{\sigma t k^2}{16 M_s} \right], \tag{9}$$

$$\frac{\sigma k}{8M_s^2} - \frac{1}{kt} + K_1(kt) = 0, \tag{10}$$

where K_1 is a modified Bessel function. The equation (10) determines the period of the resulting perturbations.

It is obvious from the foregoing analysis that for positive values of the derivative of the function $\tilde{\Phi}$, a spontaneous periodic domain structure with striped domains oriented along the easy-magnetization axis in the film plane is established in a magnetic field (Fig. 2a). However, for negative values of the derivative the in-plane anisotropy field has a large effect on the orientation of domains in a magnetic film. The deformation arising in the domain wall can lead to branching of the initial stripe domain and growth of the ''branches.'' The deformation of the domain wall loses its sinusoidal form. However, the behavior of the domain wall can be described qualitatively by examining deformations along the x and y axes. The width of a ''branch'' arising from the initial domain is determined by the relations (9) and (10) and is equal to the width of the initial domain. The effective field will be minimum if the ratio of the maximum of the deviation of the domain wall in the direction of the x axis to the maximum of the displacement along the y axis is minimum, i.e., when the deformation of the domain wall develops not in the direction of the x axis, but rather starting

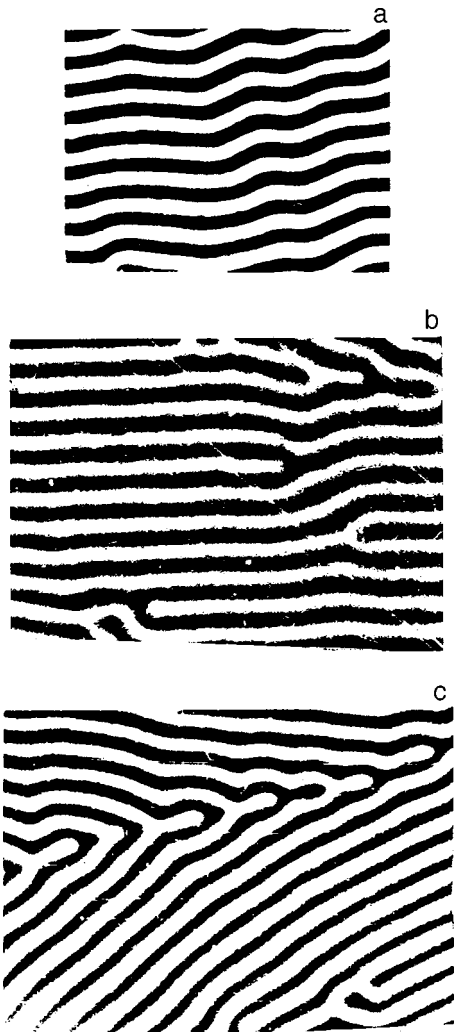

FIG. 2. a—Photograph of a striped periodic domain structure. b—Photograph of disclinations of a domain grating in the form of a *Y*-shaped domain or ''fork.'' c—Photograph of disclinations of a domain grating in the form of accumulations of *V*-shaped domains.

at some deviation of order the period of the domain structure in the direction of the *y* axis. For such development of the deformation, its growth is not accompanied by an increase in elastic forces exerted by the in-plane component of the anisotropy field, and a *Y*-shaped branched domain is formed (Fig. 2b).

Examples of physical mechanisms leading to the appearance of an easy-magnetization axis in the film plane are growth anisotropy, mechanical deformations (magnetostriction), or a small deviation of the crystallographic direction [111] of the substrate from the normal direction.[4] In magnetic films with an easy-magnetization axis in the film plane, disclinations of the domain lattice in the form of *Y*-shaped domains (or ''fork-shaped'' disclinations[5]) appear.

Many factors responsible for the anisotropy (growth, mechanical stresses) can be largely eliminated in the process of synthesis of the magnetic film or during subsequent annealing of the film. If no other physical mechanisms for the formation of an easy-magnetization axis in the plane of the magnetic film are present, then the projections of the three other crystallographic directions [111], making angles of 120° with one another, make the decisive contribution to the process leading to the formation of a planar anisotropy. In this case, accumulations of *V*-shaped domains form in a magnetic field (Fig. 2c).

Despite its approximate character, our analysis of the behavior of striped domains in magnetic films with an in-plane component of the anisotropy vector agrees quite well with experiment. It not only determines the stability conditions of a flat domain wall relative to bending deformations, but it also predicts qualitatively the development of the bending deformation of a wall, if the stability conditions are not completely satisfied—appearance of a *Y*-shaped branched domain and accumulations of *V*-shaped domains.

Periodic domain structures find wide application as reorganizable magnetooptic diffraction gratings in optoelectronics: in magnetooptic deflectors, spectrum analyzers, magnetic field sensors, magnetically controlled lasers, and so on.[4,9] It should be expected that a domain grating with disclinations in magnetooptic diffraction should act like a magnetic hologram of an optical vortex and transform a fundamental Gaussian beam into a wave carrying angular momentum.[5–8] The disclinations of a domain structure have a strong effect on the parameters of the diffracted radiation, and they must be either eliminated (in deflectors, spectrum analyzers, and lasers) or induced to form optical vortices. Therefore the problem of matching the parameters of magnetooptic materials is very pressing, and the relation between the magnetic properties of a film (for example, the anisotropy field) and the quality of a domain grating, studied in the present letter, makes it possible to optimize the technology for synthesizing magnetooptic materials for specific technical applications.

[1] F. B. Hagedorn, J. Appl. Phys. **41**, 1161 (1970).
[2] E. Schlomann, in *International Conference on Magnetism*, Moscow, August 1973, pp. 22–28.
[3] V. G. Bar'yakhtar and Yu. I. Gorobets, *Magnetic Bubble Domains and Their Arrays* (Naukova dumka, Kiev, 1988), pp. 133–135.
[4] A. M. Balbashov and A. Ya. Chervonenkis, *Magnetic Materials for Microelectronics* (Énergiya, Moscow, 1979), pp. 21–65.
[5] J. F. Nye, Proc. R. Soc. Lond. A **387**, 105 (1983).
[6] N. A. Groshenko, A. V. Volyar, and T. A. Fadeeva, Pis'ma Zh. Tekh. Fiz. **22**(15), 37 (1996) [Tech. Phys. Lett. **22**, 615 (1996)].
[7] N. Groshenko, T. Fadeyeeva, and A. Volyar, *Nonlinear Optics of Liquid and Photorefractive Crystals*, SPIE **2649** (1995), pp. 212–215.
[8] A. Volyar, T. Fadeyeeva, and N. Groshenko, Pis'ma Zh. Tekh. Fiz. **23**(22), 58 (1997) [Tech. Phys. Lett. **23**, 883 (1997)].
[9] Yu. F. Vilesov and N. A. Groshenko, *Magnetic Optoelectronics* (Tavriya, Simferopol', 1995).

Translated by M. E. Alferieff

The Oktupol' galathea electric-discharge confinement system

A. I. Morozov, A. I. Bugrova, A. M. Bishaev, and V. A. Nevrovskiĭ

Moscow State Institute of Radio Engineering, Electronics, and Automation (Technical University)
(Submitted January 20, 1999)
Pis'ma Zh. Tekh. Fiz. **25**, 57–61 (September 12, 1999)

A new electric-discharge plasma confinement system based on an octupole magnetic field is described. The results of experiments with a confinement system using argon are reported.
 [S1063-7850(99)01009-5]

The Oktupol' electric-discharge plasma confinement system belongs to the galathea class of magnetic traps, i.e., confinement systems with current-carrying conductors which are completely immersed in plasma.[1] Such conductors are called myxines.

Galatheas make it possible to produce a magnetic-field configuration having a gapless magnetic barrier around the plasma volume where the magnetic field is arbitrarily close to zero. In Ref. 2 it was suggested that plasma be produced in such confinement systems by means of an electric discharge between a heated cathode placed inside the confinement system and the walls of a vacuum chamber, which serve as the anode. The results obtained in Refs. 2 and 3 in MIREA on the ''Avos'ka'' ÉRL-M facility with a plasma volume of 0.5l demonstrate the great possibilities of such electric-discharge confinement systems.

The ÉRL-M confinement system uses a quadrupole magnetic field produced by two coaxial current-carrying rings with currents flowing in the same direction. To increase the plasma-occupied volume in the region of a weak magnetic field (up to 5l), it was decided to use an octupole magnetic configuration and to increase the barrier field to 0.1 T by switching to pulsed powering of the magnetic system.

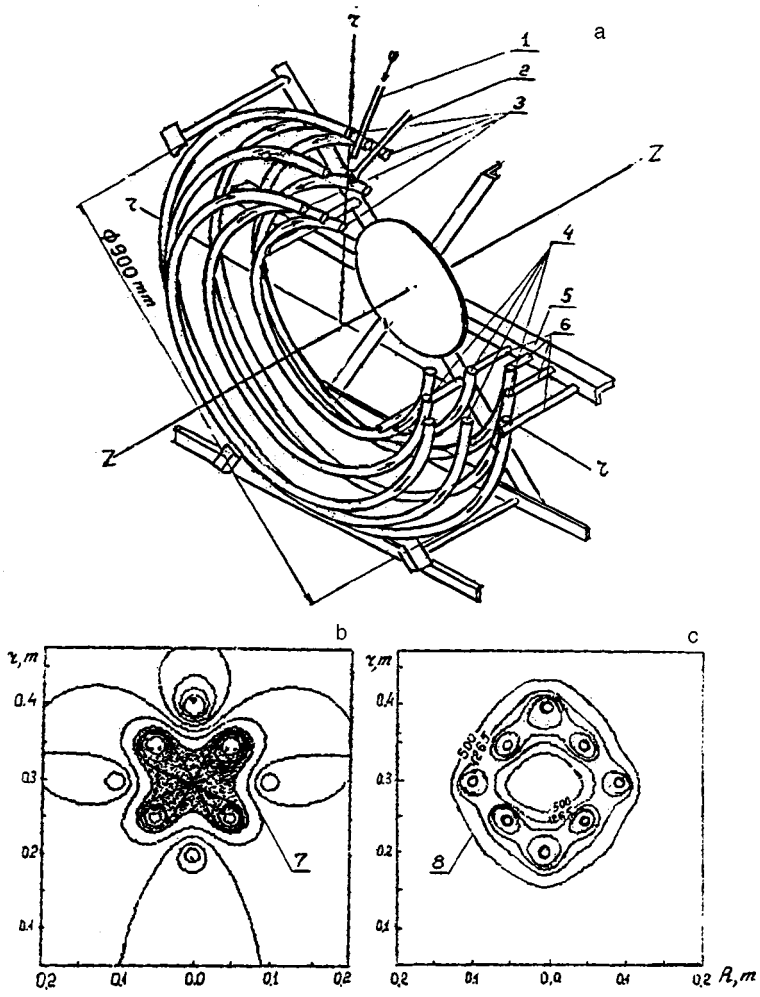

FIG. 1. Schematic of the Oktupol' magnetic system (a) and magnetic field distribution in a section of the confinement system passing through the *z* axis (b—flux lines, c—lines of constant voltage): *1*—gas input, *2*—cathode, *3*—repellers and compensators, *4*—myxines, *5*—framework, *6*—myxine holders, repellers, and compensators, *7*—magnetic flux lines, *8*—B = const contours.

Presumably, the plasma parameters in the Oktupol' confinement system can be improved.

A toroidal magnetic-field formed by four myxines was used as a basis for the Oktupol' confinement system. In this system, because of the curvature of the central line of the torus, the field differs strongly from that of a straight octupole formed by four straight conductors.

Inserting two repeller coils and two more compensating coils, all with currents flowing opposite to the current in the myxines, decreased the attractive forces between the myxines and improved the field configuration.[4] Thus, the Oktupol' magnetic system consists of eight coils, shown in Fig. 1. All coils are connected in series. The optimal magnetic configuration is obtained with the ratios $N_1:N_2:N_3 = 1:1.25:0.75$, where N_1, N_2, and N_3, are the number of turns in a myxine, a repeller, and a compensator, respectively. The total number of ampere-turns is zero, and the magnetic field is concentrated primarily near the coils, encircling the central line of the torus. The magnetic field configuration in the Oktupol' confinement system is shown in Figs. 1b and 1c. A region of essentially zero magnetic field and the surrounding magnetic barrier can be seen in the figure.

Each coil was wound with aluminum foil, which played the role of a liner, and was attached with six stainless steel holders to the Oktupol' framework. The outer diameter and width of Oktupol' were 900 mm and 380 mm, respectively. The system was placed in a vacuum chamber (background gas pressure 10^{-3} N/m^2), a heated tungsten-wire cathode was placed near the central line of the torus, gas was introduced into the region near the cathode, and a discharge was ignited, the anode consisting of the chamber and the liner of the myxines. A pulsed voltage source powered the discharge. The initial voltage was up to 5 kV, and the pulse duration was ~ 10 ms. A dc current source with a discharge voltage of up to 400 V could also supply power. A barrier magnetic field up to $H = 0.1$ T was produced by a pulsed-power system (pulse duration ~ 30 ms). An additional power supply maintained a barrier field $H \approx 0.005$ T for a long time (up to ~ 15 min) and $H \approx 0.01$ T for a short time (up to 2 min).

The basic measurements were performed with argon, whose flow rate was regulated in the range $\dot{m} = 1.3–13$ mg/s. The working pressure in the chamber was set in the range $p = (1.8–3.7) \cdot 10^{-2}$ N/m^2.

The observations showed that the plasma in the confinement system occupies the shaded region in Fig. 1b. The current–voltage characteristics of the discharge demonstrate strong saturation with respect to current with discharge voltages above ~ 110 V, and the saturation current is determined only by the heating of the cathode. It was difficult to ignite a discharge when only the chamber served as the anode and the liners of the myxines were not connected to the source powering the discharge. In this case it was necessary to apply ~ 300 V with a magnetic field of 0.005 T in the barrier region.

Probe measurements of the plasma parameters showed the existence of a potential well in the plasma, where ions are confined, similarly to the ÉRL-M confinement system, but wider in the transverse direction. In this region the electron temperature is $T_e = 20–22$ eV, the charged-particle density is $n_e \sim 10^{11}$ cm^{-3}, the space-charge potential is $\varphi \approx -50$ V with a discharge voltage of 200 V and a barrier field $H = 0.005$ T (Fig. 2). In contrast to the ÉRL-M confinement system, the plasma in the Oktupol' possesses a fairly sharp boundary, determined visually from the emission of the discharge and the distribution of the plasma parameters.

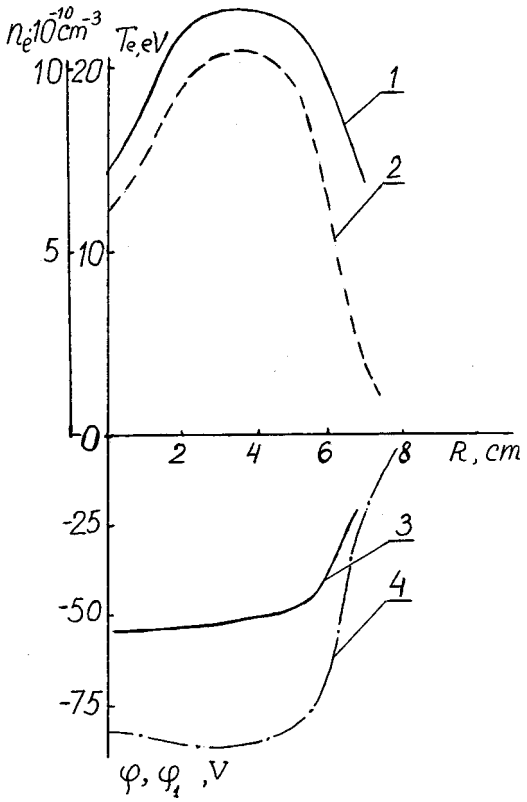

FIG. 2. Plasma parameters versus the short radius R of the torus: *1*—Electron temperature T_e, *2*—electron density n_e, *3*—plasma potential φ, *4*—floating potential φ_1.

In the experiments, the oscillations of the discharge current, the floating potential of the probe, and the ionic current on a probe in the frequency range 100 kHz–100 MHz were measured. It was found that a 0.005–0.01 T magnetic field greatly decreases the amplitude of the oscillations at frequencies above 30 MHz and increases the amplitude of the oscillations at frequencies below 5 MHz.

This work was supported by the Ministry of Atomic Energy of the Russian Federation.

We are grateful to V. A. Abramov for his constant interest and suggestions while this work was being performed.

[1] A. I. Morozov, Fiz. Plazmy **18**, 305 (1992) [Sov. J. Plasma Phys. **18**, 159 (1992)].
[2] A. I. Bugrova, A. S. Lipatov, A. I. Morozov, and V. K. Kharchevnikov, Fiz. Plazmy **19**, 1411 (1993) [Plasma Phys. Rep. **19**, 741 (1993)].
[3] A. I. Bugrova, A. S. Lipatov, A. I. Morozov, and V. K. Kharchevnikov, Fiz. Plazmy **19**, 972 (1993) [Plasma Phys. Rep. **19**, 505 (1993)].
[4] Yu. A. Ermakov and A. I. Morozov, in *Abstracts of Reports at the 25th Zvenigorod Conference on Plasma Physics and Controlled Thermonuclear Fusion* (March 2–6, 1998), p. 69.

Translated by M. E. Alferieff

Electrostriction mechanism of microwave losses in a ferroelectric film and experimental confirmation

O. G. Vendik and A. N. Rogachev

St. Petersburg State Electrotechnical University, Russia
(Submitted May 18, 1999)
Pis'ma Zh. Tekh. Fiz. **25**, 62–68 (September 12, 1999)

The experimental confirmation of the existence of the electrostriction mechanism of microwave losses in a thin ferroelectric film is discussed. The results of simulation of the dielectric loss tangent due to the mechanism discussed for a planar capacitor with one gap are presented and compared with existing experimental data for an interdigital capacitor. The simulation results agree well with the experimental data. The small discrepancy with experiment could be due to inaccurate determination of the sound velocity in the ferroelectric film and to differences in the capacitor structures used in the simulation and in the experiment. © *1999 American Institute of Physics.* [S1063-7850(99)01109-X]

Dielectric losses at microwave frequencies are the main obstacle to practical applications of controllable ferroelectric (FE) devices. The sources of these losses have thus far not been absolutely identified. According to the latest publications, the microwave losses in ferroelectrics are due to the following mechanisms:[1,2]

1) fundamental losses due to multiphonon scattering of the soft FE mode;

2) conversion of microwave oscillations of the electric field into acoustic oscillations via scattering by regions with residual FE polarization;

3) conversion of microwave oscillations of the electric field into acoustic oscillations as a result of fields generated by charged defects;

4) conversion of microwaves into hypersound because of resonance phenomena arising when the characteristic dimensions of the working region of the FE device become multiples of half the hypersound wavelength.

All these mechanisms have been formulated for so-called virtual ferroelectrics, used at liquid-nitrogen temperature. However, they can also be applied to conventional ferroelectrics, such as $(Ba_x, Sr_{1-x})TiO_3$, in the paraphase at room temperature.

This letter is devoted to proving the existence of experimental confirmation of the existence of the electrostriction mechanism of microwave losses due to hypersonic resonance in a FE film. Microwave losses of this type appear in a FE film with nonzero bias voltage, which generates an induced piezoelectric effect in the FE film. For a flat capacitor, hypersonic resonance can arise in the gap between the electrodes and within the FE film. This phenomenon was predicted theoretically in Ref. 2, and a formula describing the behavior of the dielectric loss tangent due to hypersonic resonance phenomena was also presented there:

$$\tan\delta_{ac}=[V\langle\sin^2(kg/2)/(kg/2)\rangle + 2V_k\langle\sin^4(kh/2)/(kh/2)\rangle]\Phi(E). \quad (1)$$

In this formula

$$V_{(k)}=(4/s)Q_{(k)}^2\varepsilon_0^3, \quad (2)$$

$$\Phi(E)=\varepsilon_r^3(E_{dc})E_{dc}^2, \quad (3)$$

$$k=\frac{\omega}{v_s}, \quad (4)$$

where s is the diagonal component of the elasticity tensor, Q and Q_k are, respectively, the diagonal and off-diagonal components of the electrostriction tensor, g is the distance between the electrodes, h is the thickness of the FE film, ω is the microwave frequency, and v_s is the longitudinal phase velocity of sound in the ferroelectric.

In Ref. 2 it was shown that the dielectric loss tangent due to the electrostriction mechanism is a function of frequency, and for a flat $SrTiO_3$ capacitor it is less than 0.01 in the frequency range 1–10 GHz.

Until recently it was difficult to check the theory expounded in Ref. 2 because of the lack of data on the dependence of the dielectric loss tangent for a FE film in a sufficiently wide frequency range. However, the first publication giving such information has recently appeared.[3] In Ref. 3 the results of an investigation of a series of interdigital capacitors based on a thin $(Ba_{0.5}, Sr_{0.5})TiO_3$ film are presented. The measurements were performed at room temperature in the frequency range 50 MHz–20 GHz. The method of conformal mapping was used to obtain the values of the dielectric constant and the dielectric loss tangent. This method made it possible to obtain reliable results right up to 5 GHz. In Ref. 3 the results of measurements performed on an interdigital BSTO capacitor with interelectrode distance $g=7.5\,\mu$m and FE film thickness $h=0.4\,\mu$m are described in detail. The frequency dependence of the dielectric loss tangent of the FE film in this capacitor is presented in Fig. 1a.

In summary, experimental data making it possible to check the validity of the theory proposed in Ref. 2 are now available.

To compare the experimental results of Ref. 3 with theoretical estimates, it is first necessary to extract from the

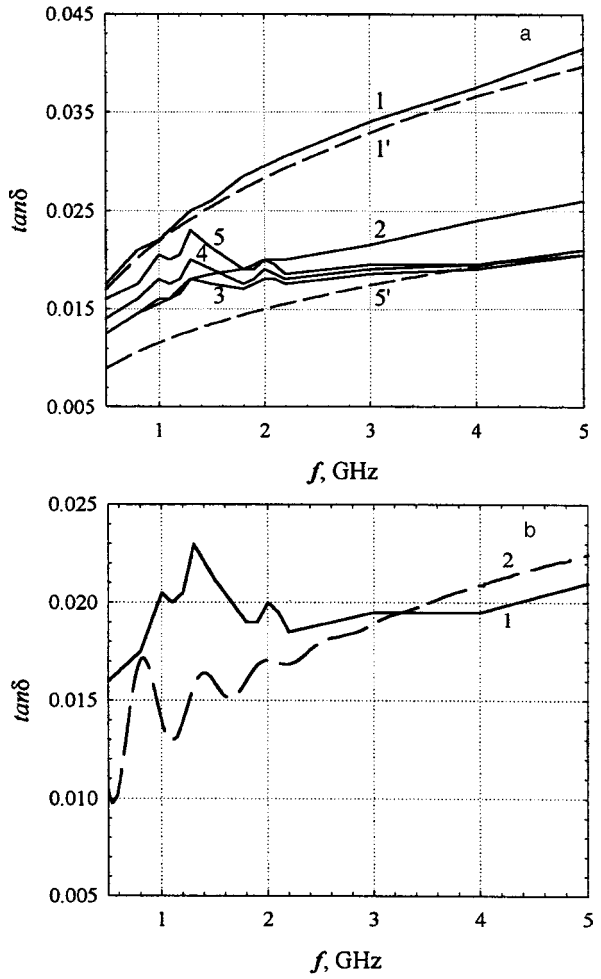

FIG. 1. a—Frequency dependence of the dielectric loss tangent for an interdigital capacitor based on a thin FE film. Experiment (Ref. 3): *1*—$U_b=0$ V, *2*—$U_b=10$ V, *3*—$U_b=20$ V, *4*—$U_b=30$ V, *5*—$U_b=40$ V. Simulation: *1′*—$f^{1/3}$ for $U_b=0$ V and 5′—$f^{1/3}$ for $U_b=40$ V. b—Frequency dependence of microwave losses due to hypersound generation in the capacitor gap and losses due to charged defects ($U_b=40$ V): *1*—experimental results (Ref. 3), *2*—simulation.

experimental data the part of the microwave losses for which the mechanism under study is responsible. As already mentioned above, a hypersound resonance arises in a FE film only with a nonzero bias voltage, and therefore for a zero bias voltage (Fig. 1a, curve *1*) this mechanism does not contribute to the total microwave losses in the film. It should be noted that in this case the experimental values of the dielectric loss tangent can be fit to a high degree of accuracy by a function of the form $\tan\delta(f)\sim f^{1/3}$ (Fig. 1a, curve *1′*). For a nonzero bias voltage the losses via hypersound appear in the form of resonance peaks in the frequency characteristic of the dielectric loss tangent (Fig. 1a, curves *2*–*5*). The second circumstance that helps to distinguish the various loss mechanisms is that for the given dimensions of the capacitor structure the contribution of the mechanism under study is negligibly small at frequencies above 2–3 GHz. Thus, to separate the loss mechanism under discussion from the others it is first necessary to fit the field dependence of the dielectric loss tangent due to the other loss mechanisms using the dependence

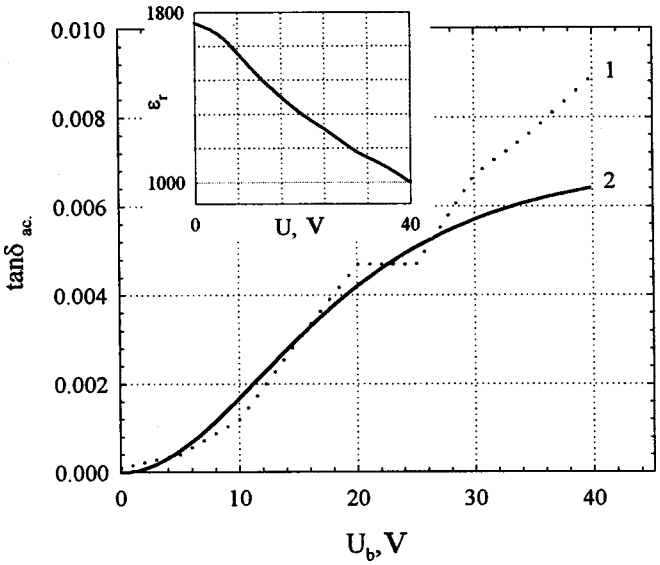

FIG. 2. Microwave losses due to hypersound generation in a capacitor gap as a function of the bias voltage: *1*—Experimental results (Ref. 3, $f=1$ GHz), *2*—simulation ($f=0.8$ GHz).

$$\tan\delta(E,f)=A(E)f^{1/3}, \tag{5}$$

where $A(E)$ is a function of the bias field, which ensures agreement of the experimental and computed values of the dielectric loss tangent at high frequencies. Next, the computed dependence must be subtracted from the experimental dependence for each value of the bias voltage. The remainder is the dielectric loss tangent due to the mechanism under investigation.

The source of the losses described by the expression (5) are charged defects.[1,4] It was shown in Ref. 4 that the losses due to charged defects are characterized by a bias-voltage dependence of $\tan\delta$ that is proportional to the field-dependence of the dielectric constant. This relation between the dielectric loss tangent and the dielectric constant of a FE film can also be seen from the experiment described above.[3] The frequency dependence of the microwave losses due to charged defects is determined by the sizes of the charged regions. A reasonable choice of the size distribution of charged regions makes it possible to satisfy the experimentally observed dependence $f^{1/3}$.

Returning to the acoustic loss mechanism, it should be noted that for the given values of the interelectrode gap (7.5 μm) and the thickness of the FE film (0.4 μm) the mechanism under study forms maxima of the microwave losses at frequencies of 1, 1.3, and 2 GHz.

To calculate the dielectric loss tangent using the expression (1) it is first necessary to determine the longitudinal phase velocity of sound in the $(Ba_{0.5}, Sr_{0.5})TiO_3$ film. The sound velocity $v_s=4200$ m/s used in the simulation was found by interpolating the velocities in $SrTiO_3$ and $BaTiO_3$.[5]

Figure 1b shows the frequency dependence of the microwave losses with a bias voltage ($U_b=40$ V). The experimental results (1 GHz) and the simulation results (0.8 GHz) for the field dependence of the loss mechanism under investigation in the range 0–40 V are shown in Fig. 2. The value of the relative dielectric constant obtained in Ref. 3 was used in

the calculation (Fig. 2, inset). The discrepancy between the positions of the peaks of the microwave losses for the simulation and experimental results can be explained by the error in determining the sound velocity in the FE film.

In conclusion, it should be noted that the simulation results agree well with the experimental data. This can be interpreted as experimental proof of the existence of a loss mechanism via hypersound generation in the gap of a flat capacitor. The small discrepancy with experiment could be due to the differences in the capacitor structures used in the calculation and in experiment.[3] The frequency dependence of the microwave losses in the interdigital capacitor used in the experiment of Ref. 3 could have certain features due to the periodic structure of the capacitor. Thus, the theory developed in Ref. 2 needs to be modified to take account of the construction of an interdigital capacitor with several gaps. The result could be an acoustic model resembling the Kronig–Penney model for energy bands in a solid. This will make it possible to give recommendations for changing the dimensions of an interdigital capacitor and, in consequence, to decrease microwave losses in the working frequency range of the device.

We thank L. T. Ter-Martirosyan for a discussion of this work and D. Pond for providing prior to publication[3] the experimental data on microwave losses in a flat BSTO capacitor.

[1] O. G. Vendik, L. T. Ter-Martirosyan, and S. P. Zubko, J. Appl. Phys. **84**, 993 (1998).
[2] O. G. Vendik and L. T. Ter-Martirosyan, Zh. Tekh. Fiz. **69**, (8) (1999) [in press].
[3] J. M. Pond, S. W. Kirchoffer, W. Chang, J. S. Horwitz, and D. B. Chrisey, *Integrated Ferroelectrics*, Vol. 22, p. 317.
[4] O. G. Vendik and L. M. Platonova, Fiz. Tverd. Tela (Leningrad) **13**, 1617 (1971) [Sov. Phys. Solid State **13**, 1352 (1971)].
[5] G. A. Smolenskiĭ, *The Physics of Ferroelectric Phenomena* (Nauka, Leningrad, 1985), 396 pp.

Translated by M. E. Alferieff

Erbium-doped oxidized porous silicon for integrated optical waveguides

V. P. Bondarenko, V. A. Yakovtseva, L. N. Dolgiĭ, N. N. Vorozov, N. M. Kazyuchits, L. Tsybeskov, and F. Foucher

Belorussian State University for Informatics and Radio Electronics, Minsk;
Belorussian State University, Minsk;
Rochester University, Rochester, New York 14626, USA
(Submitted April 12, 1999)
Pis'ma Zh. Tekh. Fiz. **25**, 69–73 (September 12, 1999)

It is shown for the first time that introducing erbium electrochemically into waveguide structures based on oxidized porous silicon not only preserves their waveguide properties but it also opens up prospects for producing active waveguide devices based on them. It is established that erbium in a waveguide is in an optically active state and light with wavelengths 381 and 523 nm excites the erbium ions most efficiently. © *1999 American Institute of Physics.* [S1063-7850(99)01209-4]

In Ref. 1 it was shown that it is possible to produce integrated optical waveguides based on oxidized porous silicon (PS). The fabrication process is compatible with the traditional silicon technology and consists in the formation of local layers of PS followed by thermal oxidation of the layers. All waveguides developed thus far using oxidized PS[1–6] are passive devices. Active waveguide devices can be obtained by introducing optically active impurities into the waveguide channel. Erbium is of special interest for this purpose, since its main emission band with wavelength 1532 nm corresponds to minimum losses of the quartz fiber optics.[7] In the present work, electrochemical method of deposition of erbium-containing material in PS layers, followed by thermal oxidation of the structures obtained, was used to introduce erbium ions into oxidized PS.

Hole-type (111) silicon wafers with resistivity 0.01 $\Omega \cdot$cm were used. The local PS regions were formed by anodization in a 24% solution of hydrofluoric acid at current density 20 mA/cm^2 through a silicon nitride mask. Erbium was introduced by cathodic treatment in an alcohol solution 0.1 M $Er(NO_3)_3$ at current density 0.1 mA/cm^2 for 30 min. Next, the samples were heat-treated for 1 h in oxygen at 300 °C, followed by 30-min treatment in vapor at 1000 °C, and then in argon at 1150 °C 30 min.

Spectroscopic investigations were performed on 3 m^2 oxidized PS samples, prepared by a similar method but without a nitride mask. The erbium distribution profiles in the waveguides were determined by x-ray microprobe analysis. The photoluminescence (PL) spectra were measured at room temperature and at the temperatures of liquid helium (4.2 K) and liquid nitrogen (77 K). The photoluminescence excitation spectra (PLE) were recorded in the wavelength range 250–1000 nm at 300 K.

Comparative investigations showed that doping with erbium does not alter the waveguide properties of oxidized PS. Figure 1 shows a transverse section of an integrated waveguide based on oxidized PS (a) and erbium distribution profiles over the surface (b) and depth (c) of the waveguide channel. As one can see from Fig. 1a, the channel waveguides are 8 μm thick and 20 μm wide. Scanning the waveguide surface (Fig. 1b) showed erbium to be present in

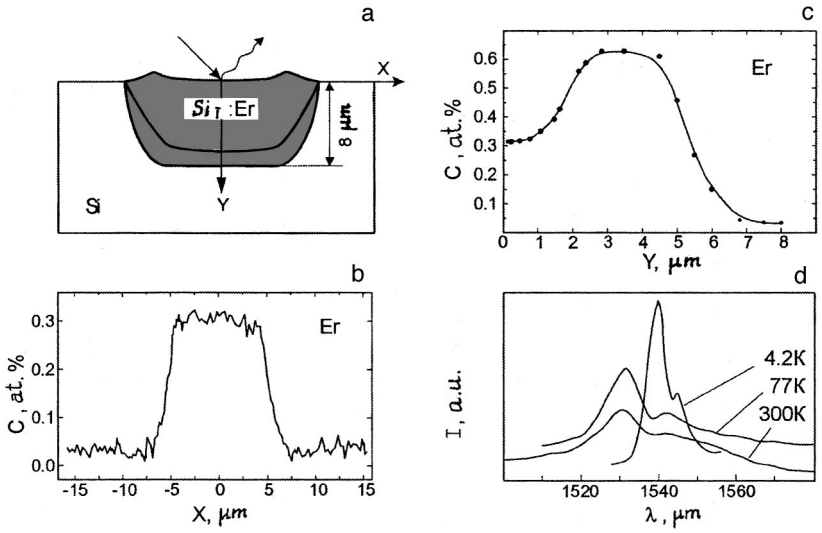

FIG. 1. Transverse section of an integrated waveguide based on oxidized porous silicon Si_I (a), erbium distribution profiles on the surface (b) and in the interior (c) of the waveguide channel and photoluminescence spectra of an erbium-doped waveguide (d).

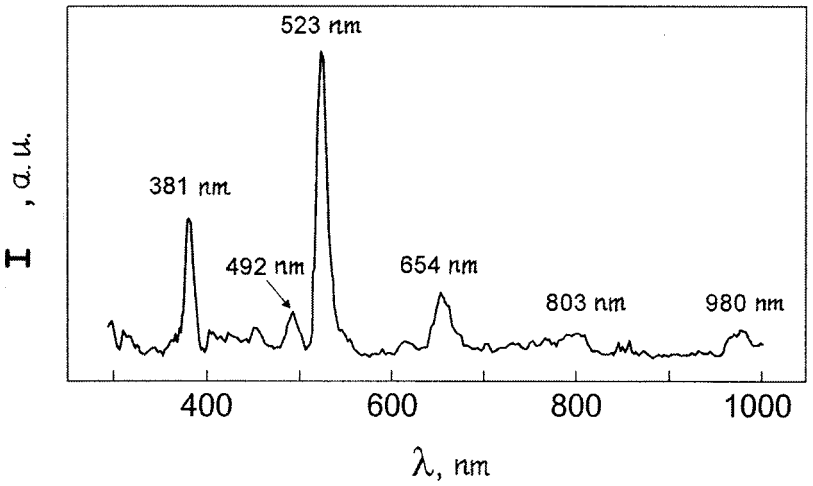

FIG. 2. Photoexcitation spectrum of erbium-doped oxidized porous silicon ($\lambda = 1532$ nm).

an 11–12 μm wide central part with constant concentration 0.3 at. %. Scanning a cleavage face of the waveguide (Fig. 1c) showed that the erbium concentration increases from 0.3 at. % at the surface to 0.6 at. % at a depth of 2.5 μm and remains at this level to 4.5 μm, after which it decreases to 0.1 at. % at depths greater than 7 μm. Comparing the erbium distribution profiles with the waveguide section shows that erbium is introduced predominantly into the core of the channel. This result is very important, because guided waveguide modes propagate precisely along the central part of the waveguide.[2–4]

It is known[7] that to produce efficient optical amplifiers the erbium concentration in the fiber should be at least 0.001 at. % with an optical fiber several tens of meters long. In integrated waveguide structures the waveguide can be only several centimeters long, and to obtain amplification the erbium concentration should be at least 0.1 at. %.[7] The erbium concentration levels obtained in waveguide channels of oxidized PS in the present work satisfy this requirement.

Figure 1d shows the the PL spectra of an erbium-doped waveguide whose surface is irradiated with a focused laser radiation. An intense peak at 1540 nm and an additional peak at 1545 nm are observed in the spectra measured at 4.2 K. These peaks are due to transitions between the first excited level $^4I_{13/2}$ and the ground state $^4I_{15/2}$ of erbium ions.[7] At 4.2 K the widths of the main and additional peaks are 4.8 and 6–7 nm, respectively, and are determined by Stark splitting of the excited and ground states of erbium ions in the matrix field of oxidized PS. Two PL peaks are also observed at the measurement temperatures 77 and 300 K. The intensity of the main peak decreased by a factor of 3 as temperature increased from 4.2 to 300 K. We observed a small difference in the spectral position of these peaks as a function of the measurement temperature. The main peak recorded at 1540 nm shifts to 1532 nm as the measurement temperature increases from 77 to 300 K. The width of the main peak was observed to increase from 4.8 to 21 nm as the measurement temperature increased from 4.2 to 300 K.

To investigate the mechanisms for exciting erbium in oxidized PS, measurements of the PLE spectra of the center emitting at 1532 nm were performed. The PLE spectrum presented in Fig. 2 shows a distinct band structure, attesting to direct optical excitation of Er^{3+} ions in the oxidized PS. The position of the peaks in the spectrum correspond to excitation by light with wavelength 381, 492, 523, 654, 803, and 980 nm, which correlates well with the position of the optical absorption bands due to transitions inside erbium ions: $^4I_{15/2} \rightarrow {}^4G_{11/2}$ (380 nm), $^4I_{15/2} \rightarrow {}^4F_{7/2}$ (490 nm), $^4I_{15/2} \rightarrow {}^2H_{11/2}$ (524 nm), $^4I_{15/2} \rightarrow {}^4F_{9/2}$ (657 nm), and $^4I_{15/2} \rightarrow {}^4I_{11/2}$ (980 nm).[7–9] The weak peak obtained by excitation with 803 nm light corresponds to the transition $^4I_{15/2} \rightarrow {}^4I_{9/2}$ (810 nm).

As follows from Fig. 2, the PL intensity is greatest when erbium ions are excited by 381 and 523 nm light, i.e., such radiation is optimal for pumping 1532 nm PL in optical amplifiers based on oxidized PS. The transitions corresponding to these peaks are ordinarily called supersensitive transitions.[9]

In summary, electrochemical deposition of erbium in PS followed by oxidation of the porous layer makes it possible to introduce erbium into the core of the waveguide channel and preserve the waveguide properties of oxidized PS. It was shown that erbium in the waveguide is in an optically active state. Radiation with wavelength 381 and 523 nm is most effective for pumping 1532 nm PL in optical waveguides based on oxidized PS.

This work was supported in part by the CRDF (grant BE2–108).

[1] V. Bondarenko, V. Varichenko, A. Dorofeev *et al.*, Tech. Phys. Lett. **19**, 463 (1993).
[2] S. Nagata, C. Domoto, T. Nichimura, and K. Iwameji, Appl. Phys. Lett. **72**, 2945 (1998).
[3] V. Bondarenko, A. Dorofeev, and N. Kazuchits, Microelectron. Eng. **28**, 447 (1995).
[4] G. Maiello, S. La Monica, A. Ferrari *et al.*, Thin Solid Films **297**, 311 (1997).
[5] A. Tomov, V. Filippov, and V. Bondarenko, Tech. Phys. Lett. **23**, 410 (1997).
[6] H. Arrand, T. Benson, A. Loni *et al.*, Electron. Lett. **33**, 1724 (1997).
[7] A. Polman, J. Appl. Phys. **82**, 1 (1997).
[8] T. Kimura, A. Yokoi, H. Horiguchi *et al.*, Appl. Phys. Lett. **65**, 983 (1994).
[9] T. Kojan, V. Kuznetzova, P. Pershukevich *et al.*, J. Appl. Spectrosc. **63**, 992 (1996).

Translated by M. E. Alferieff

Photoinduced surface-relief grating in a cubic crystal in a constant electric field

A. M. Kirillov, S. M. Shandarov, and N. I. Burimov

Tomsk State University for Control Systems and Radio Electronics, Russia
(Submitted January 21, 1999)
Pis'ma Zh. Tekh. Fiz. **25**, 74–77 (September 12, 1999)

A theoretical model gibing a time-independent description of a photorefractive surface-relief grating in a cubic crystal placed in an external constant electric field is proposed. The model is used to calculate the height of the surface barrier of a $Bi_{12}TiO_{20}$ crystal for the (001) cut, where there is no interaction of light beams in the interior volume of the medium. © *1999 American Institute of Physics.* [S1063-7850(99)01309-9]

The periodic relief photoinduced during the formation of photorefractive gratings by the interference pattern of two light waves on the surface of sillenites placed in a constant external field has been investigated experimentally in Refs. 1–3. Its presence is due to elastic deformations, which accompany the space-charge field of the photorefractive grating as a result of the piezoelectric effect.[4] A theoretical analysis of the surface structure of a photorefractive grating has been performed for crystals to which an external field was not applied.[5–7]

In the present letter we present a theoretical model describing the structure of the electric and elastic fields of a photorefractive grating in the stationary regime for crystals with an applied constant field. We consider a photorefractive grating with wave vector $\mathbf{k}_g$, oriented along the [110] crystallographic axis in a cubic crystal with symmetries 23 and $43m$ (see Fig. 1). It is formed with a symmetric geometry of interaction of light beams, such that the bisector of the angle between the beams lies along the [001] axis of the sample. An electric field is applied to the crystal along the [110] axis and is oriented in the same direction as the vector $\mathbf{k}_g$. We assume that the boundary $x=0$ of the crystal is mechanically free, and the permittivity of the dielectric medium for $x>0$ is ε_0.

Neglecting self-diffraction, we represent the light intensity distribution in the crystal as

$$I(z)=I_0[1+m\cos(k_g z)], \tag{1}$$

where I_0 is the total intensity of the signal and reference beams, $k_g=|\mathbf{k}_g|=2\pi/\Lambda$, m is the degree of modulation of the light, and Λ is the period of the interference pattern. In the stationary regime and under conditions such that the dark conductivity and saturation of traps can be neglected, the electron density in the conduction band is related linearly with the light intensity. Using the electrostatic potential to describe the space-charge field and the continuity equation, we obtain an equation describing the distribution of the amplitude of the first spatial harmonic $\varphi_m(x)$ of the potential in the crystal

$$\frac{\partial^2\varphi_m}{\partial x^2}-k_g^2\varphi_m=-m\left(\frac{k_BT}{e}k_g^2+ik_gE_0\right), \quad \text{for} \quad x\leqslant 0, \tag{2}$$

where k_B is Boltzmann's constant, T is the absolute temperature, e is an elementary electric charge, and E_0 is the amplitude of the external electric field. Using the continuity of the potential and the fact that the normal component of the current is zero at the boundary $x=0$, it can be shown that the amplitude of the space-charge field in the sample, assuming a fixed distribution of photoelectrons in the conduction band, is independent of the transverse coordinate x. Therefore, if the grating of the electric field is prescribed,[6] whose potential distribution in our case has the form

$$\varphi(z)=\frac{m}{k_g}(E_D\cos(k_gz)-E_0\sin(k_gz)), \quad \text{for} \quad x\leqslant 0, \tag{3}$$

where $E_D=k_gk_BT/e$ is the diffusion field, is valid for the dielectric boundary in the stationary regime.

We shall determine the structure of the elastic fields from the equations of elastostatics, which in our case, taking account of the symmetry of the tensor of elastic moduli $\hat{C}$ and the tensor of piezoelectric constants $\hat{e}$, assume the form

$$\sqrt{2}C_{44}^E\frac{\partial^2U_z}{\partial x^2}+\frac{1}{2}(C_{11}+C_{12}+2C_{44}^E)\frac{\partial^2U_z}{\partial z^2}+\sqrt{2}(C_{12}+C_{44}^E)\frac{\partial^2U_x}{\partial x\partial z}=0, \tag{4}$$

$$(C_{12}+C_{44}^E)\frac{\partial^2U_z}{\partial x\partial z}+C_{11}\frac{\partial^2U_x}{\partial x^2}+C_{44}^E\frac{\partial^2U_x}{\partial^2 z}=-e_{14}\frac{\partial^2\varphi}{\partial^2 z}, \tag{5}$$

where U_x and U_z are the components of the vector of elastic displacements normal and tangential, respectively, to the boundary of the crystal, and from the boundary conditions for the elastic stress tensor $\hat{T}$

$$C_{44}^E\frac{\partial U_x}{\partial z}+C_{44}^E\frac{\partial U_z}{\partial x}=-e_{14}\frac{\partial\varphi}{\partial z}, \quad \text{at} \quad x=0, \tag{6}$$

$$C_{11}\frac{\partial U_x}{\partial x}+C_{12}\frac{\partial U_z}{\partial z}=0, \quad \text{at} \quad x=0. \tag{7}$$

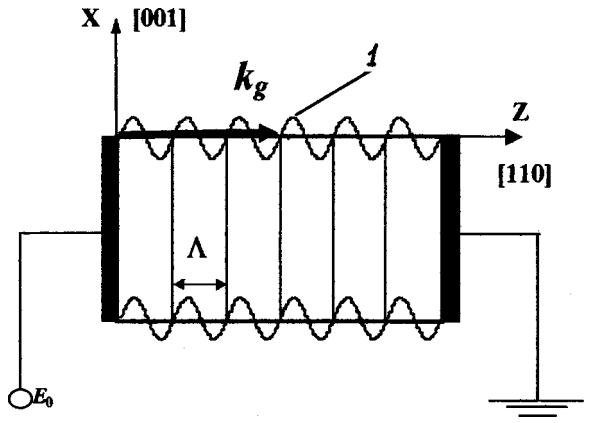

FIG. 1. Orientation of the crystallographic axes and lattice vector. The crystal occupies the half-space $x \leqslant 0$. *1*—surface relief.

It follows from Eqs. (4)–(7) that the tangential component U_z of the elastic displacement is zero, and the amplitude U_{xm} of the component transverse to the grating vector is constant in the entire volume of the sample, so that

$$U_x(z) = \left(-\frac{e_{14}}{C_{44}} m \right) \left[\left(\frac{k_B T}{e} \right) \cos(k_g z) + \frac{E_0}{k_g} \sin(k_g z) \right]. \tag{8}$$

The existence of the component U_x in the elastic field of the photorefractive grating causes bending of the (001) planes of the crystal and formation of a periodic relief on the entrance and exit faces of the sample. The contribution of the diffusion mechanism to the surface relief does not depend on its spatial period and is characterized, depending on the sign of the piezoelectric constant e_{14}, by a phase shift 0 or π relative to the interference pattern. The drift mechanism makes a contribution proportional to the grating period and is characterized by a phase shift $\pi/2$ or $-\pi/2$. The values of the amplitude of the surface relief and the resulting phase shift ϕ in the grating, which were calculated for a $Bi_{12}TiO_{20}$ crystal for various values of the spatial period Λ and amplitude E_0 of the external field, are presented in Table I for $m = 0.1$.

TABLE I.

		ϕ, grad	$\lvert U_x \rvert$, m
$E_0 = 1$ kV/cm	$\Lambda = 3\ \mu$m	−118.5	2.468×10^{-13}
	$\Lambda = 30\ \mu$m	−93.1	2.173×10^{-12}
$E_0 = 10$ kV/cm	$\Lambda = 3\ \mu$m	−93.1	2.173×10^{-12}
	$\Lambda = 30\ \mu$m	−90.3	2.17×10^{-11}

Note that in this cut (001) there is no interaction between the light beams in the interior volume of the sample.[8] However, the existence of surface relief makes it possible to observe in this case diffraction processes in a reflection geometry, investigated in Refs. 2 and 3 for the (110) cut of $Bi_{12}TiO_{20}$ and $Bi_{12}SiO_{20}$ crystals.

We thank S. I. Stepanov for helpful discussions.

[1] A. M. Bliznetsov, M. P. Petrov, and A. V. Khomenko, Pis'ma Zh. Tekh. Fiz. **10**, 1094 (1984) [Sov. Tech. Phys. Lett. **10**, 463 (1984)].
[2] S. Stepanov, N. Korneev *et al.*, Appl. Phys. Lett. **72**, 879 (1998).
[3] M. P. Petrov, A. P. Paugurt *et al.*, Pis'ma Zh. Tekh. Fiz. **24**(22), 11 (1998) [Tech. Phys. Lett. **22**, 873 (1998)].
[4] S. M. Shandarov, Zh. Tekh. Fiz. **56**, 583 (1986) [Sov. Phys. Tech. Phys. **31**, 352 (1986)].
[5] S. M. Shandarov and V. M. Shandarov, Zh. Tekh. Fiz. **60**, 106 (1990) [Sov. Phys. Tech. Phys. **35**, 199 (1990)].
[6] G. Fogarty and M. Gronin-Golomb, Opt. Lett. **20**, 2276 (1995).
[7] S. M. Shandarov and N. I. Burimov, Izv. Vyssh. Uchebn. Zaved. Fiz. No. 9, 75 (1997).
[8] M. P. Petrov, S. I. Stepanov, and A. V. Khomenko, *Photorefractive Crystals in Coherent Optical Systems* (Springer, Berlin, 1991; Nauka, St. Petersburg, 1992), 317 pp.

Translated by M. E. Alferieff

Radiation-stimulated point defects in $Li_2B_4O_7$ single crystals

E. F. Dolzhenkova, M. F. Dubovik, A. V. Tolmachev, V. N. Baumer, L. A. Grin', and V. A. Tarasov

Institute of Single Crystals, Ukrainian National Academy of Sciences, Khar'kov, Russia
(Submitted April 15, 1999)
Pis'ma Zh. Tekh. Fiz. **25**, 78–83 (September 12, 1999)

Using thermally stimulated luminescence, optical absorption, and x-ray crystallographic analysis methods, it is established that oxygen vacancies appear near Li ions in lithium tetraborate single crystals after the crystals are irradiated with (Sr:Y)-90 β particles with dose 7×10^5 Gy and that these vacancies are capable of trapping one or two electrons, which are freed at temperatures 565 and 630 K, respectively. It is shown that hole localization on oxygen ions, joining triply and quadruply coordinated boron ions near Li vacancies, and freeing of the holes at 414 K are possible. © *1999 American Institute of Physics.* [S1063-7850(99)01409-3]

Crystalline lithium tetraborate $Li_2B_4O_7$ (LTB) activated by Cu and Mn is described as an effective high-temperature dosimetric material.[1] It has been shown[2] that the output signal of the thermally stimulated luminescence (TSL) of LTB obtained for doses ranging from 0.5 to 500 Gy consists of three intense peaks at 433, 533, and 578 K and a series of low-intensity peaks. In Ref. 3, after irradiation of LTB with a flux of 4 MeV electrons ($\Phi=5\times10^{16}\,\mathrm{cm}^{-2}$), two sharp peaks were observed on the thermally stimulated conductivity curve at temperatures 423 and 458 K, and it was suggested that the trapping centers could be oxygen vacancies with different symmetry of the environment, triply- and quadruply-coordinated boron ions, respectively.[4] More complete information about trapping centers for electronic excitations in LTB is not available in the literature. In the present letter we study in detail the nature of the radiation-stimulated point defects in LTB.

LTB single crystals were grown by the Czochralski method. The basic crystallographic characteristics of the crystals corresponded to the data of Ref 5. Polar-cut, $10\times10\times2$ mm, plane-parallel plates were prepared for the investigations. The samples were irradiated at room temperature with β particles from a radionuclide source (strontium-90:yttrium-90) with 2 Ci activity (dose $D=7\times10^5$ Gy). The method for measuring the TSL is described in Refs. 6 and 7. Three peaks were observed in the TSL curves at temperatures 414, 473, and 538 K with trapping levels at 0.83, 0.96, and 1.0 eV, respectively. For the weak peak at 365 K this energy was 0.73 eV (Fig. 1a).

The induced optical absorption (OA) spectra were recorded with a SPECORD40 spectrophotometer relative to an unirradiated sample. LTB single crystals are transparent in the experimental wavelength range 200–900 nm.[7,8] A weak band with $\lambda_m=235$ nm and a wide band, without a distinct maximum, in the range 260–375 nm were observed in the induced OA spectra. Analysis of the contour of the OA band distinguished four Gaussians with $\lambda_m=235$, 285, 321, and 352 nm (Fig. 1b). The figure also shows the induced OA spectra of LTB subjected to thermal bleaching (TB). As one can see, thermal decay of bands with $\lambda_m=235$ and 285 nm occurs at 414 K, while for bands with $\lambda_m=321$ and 352 nm it occurs at temperatures 565 and 630 K, respectively. Comparing the TB and TSL shows that the thermal bleaching of

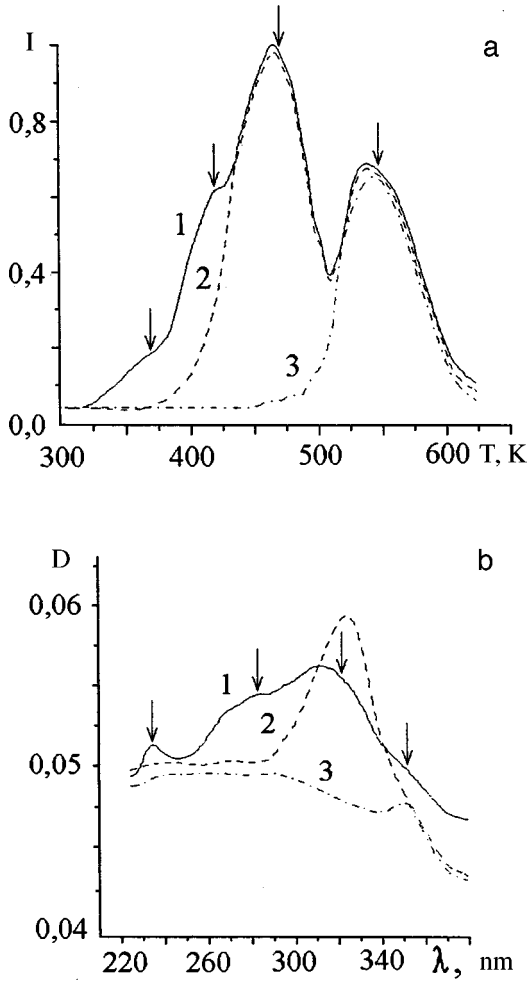

FIG. 1. Normalized thermally stimulated luminescence curves (a) and induced optical absorption spectra (b) of $Li_2B_4O_7$ single crystals: before thermal annealing and after annealing for 5 min at 414 K (2) and 565 K (3). The arrows indicate the positions of the peaks of the Gaussian components.

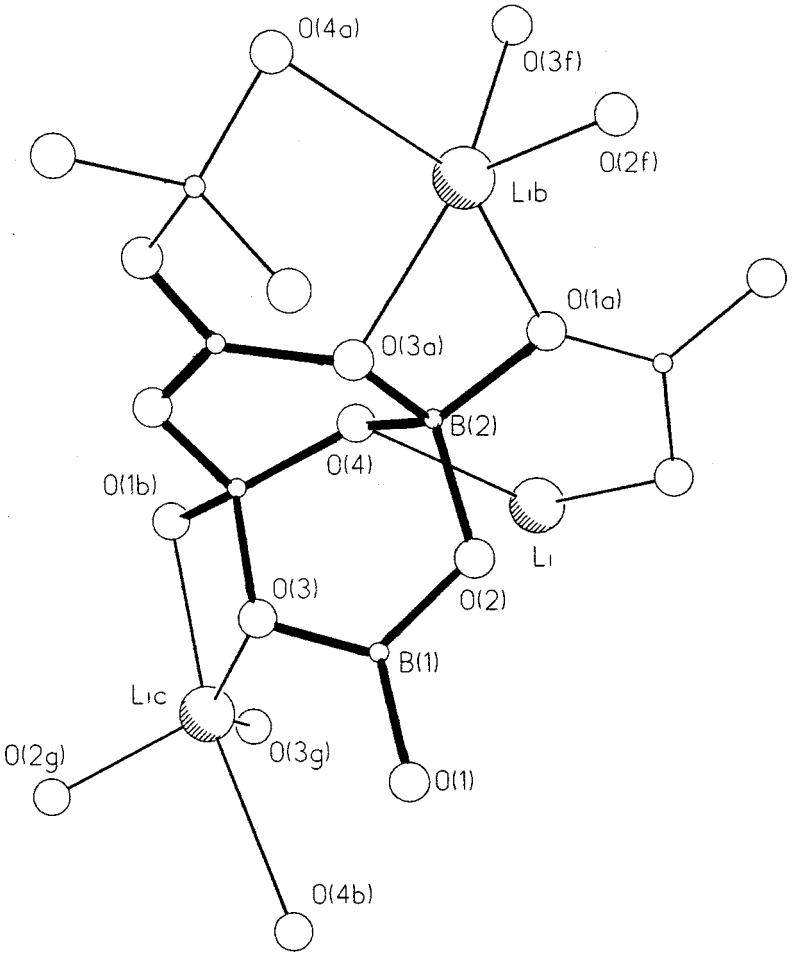

FIG. 2. Structure of $Li_2B_4O_7$. The fragment B_4O_9 is singled out.

LTB occurs in the region of the main TSL peaks.

According to Ref. 9, the computed model of a F^+ center in LiB_3O_5 crystals in the form of a vacancy at the location of an oxygen atom in an environment of quadruply coordinated boron ion, which captures an electron, should have an absorption band with $\lambda_m = 320$ nm. In an irradiated gadolinium–gallium garnet crystal, F centers are responsible for the absorption band with $\lambda_m \approx 345$ nm.[10] Similar models of centers have been observed in alkali-borate glasses:[11] an electron localized on an oxygen vacancy near an alkali ion. For this reason, in our case the induced OA bands with $\lambda_m = 321$ and 352 nm could be due to one and the same defect in a different charge state, specifically, an oxygen vacancy which has captured one (F^+ center) or two (F center) electrons, respectively.

The absorption bands with $\lambda_m = 235$ and 285 nm seem to be associated with the main and additional trapping levels of a O^- hole center, recorded in a LiB_3O_5 crystal after electron bombardment.[12] The trapped hole is localized in a *p* orbital of the oxygen ion, connecting triply and quadruply coordinated boron ions near a negatively charged stabilizing defect, for example, a Li vacancy.[13]

An additional correspondence between the $\lambda_m = 321$ and 365 nm absorption bands and F^+ and F centers, respectively, is the character of the temperature dependence of their intensity (Fig. 1b). It is known that in BeO crystals in the region of thermal decay of a hole center the concentration of F centers decreases: $F + e^+ \rightarrow F^+$, as a result of which the number of F^+ centers increases.[14] In our case the character of the bleaching of the $\lambda_m = 352$ nm and 321 nm bands is similar and therefore can result from F centers capturing holes freed through thermal decay of an O^- center.

X-Ray structural investigations of the LTB crystals were performed on a Siemens P3/PC D500 diffractometer in monochromatized Mo radiation. The results were analyzed with the SHELTXL-PLUS program package. The strongest peaks (up to 0.7 e/Å^3) in the irradiated crystal in the difference Fourier synthesis near O(1), O(2), and O(3) ions point to oxygen vacancies arising at the location of these ions (Fig. 2). The indicated O ions, connecting triply and quadruply coordinated boron ions, are the nearest neighbors of the Li ion. The occupation factor, determined more accurately in the calculation of the structure of irradiated LTB crystals, showed a deficiency of O(1) atoms in their crystallographic positions—$K = 0.986$. Therefore the most likely candidate for the formation of an oxygen vacancy is an O(1) atom, connecting the neighboring structural blocks. A hole center can be realized on O(1)–O(3) atoms. This possibility is indicated by the presence of Li vacancies ($K = 0.929$) in irradiated LTB crystals.

[1] El. D. R. Vij, *Thermoluminescent Materials*, (PRT Prentice-Hall, Inc., 1993), p. 452.

[2] Y. Kutomi, M. H. Kharita, and S. A. Durrani, Radiat. Meas. **24**, 407 (1995).
[3] Ya. V. Burak, B. N. Kopko, I. T. Lyseĭko *et al.*, Neorg. Mater. **25**, 1226 (1989).
[4] S. F. Radaev, L. A. Muradyan, L. F. Malakhova *et al.*, Kristallografiya **34**, 1400 (1989) [Sov. Phys. Crystallogr. **34**, 842 (1989)].
[5] B. P. Nazarenko, E. F. Dolzhenkova, and A. B. Levin, Functional materials **1**, 146 (1994).
[6] M. F. Dubovik, A. N. Shekhovtsov, L. A. Grin' *et al.*, in *Proceedings of the 1998 IEEE International Frequency Control Symposium*, May, 27–29 1998, Pasadena, CA USA, pp. 766–769.
[7] V. N. Baumer, L. A. Grin', and E. F. Dolzhenkova, Functional materials **6**, 154 (1999).
[8] O. T. Antonyak, Ya. V. Burak, I. T. Lyseĭko *et al.*, Opt. Spektrosk. **61**, 550 (1986) [Opt. Spectrosc. **61**, 345 (1986)].
[9] A. V. Kuznetsov, A. B. Sobolev, I. N. Ogorodnikov, and A. V. Kruzhalov, Fiz. Tverd. Tela (St. Petersburg) **36**, 3530 (1994) [Phys. Solid State **36**, 1876 (1994)].
[10] V. G. Kostishin, L. M. Letyuk, O. E. Bugakova, and E. R. Senderson, Neorg. Mater. **33**, 853 (1997).
[11] S. Arafa and A. Bishay, Phys. Chem. Glasses **10**, 192 (1969).
[12] I. N. Ogorodnikov, A. V. Porotnikov, A. V. Kruzhalov *et al.*, Fiz. Tverd. Tela **40**, 2008 (1998) (St. Petersburg) [Phys. Solid State **40**, 1817 (1998)].
[13] I. N. Ogorodnikov, A. V. Porotnikov, S. V. Kudyakov *et al.*, Fiz. Tverd. Tela **39**, 1535 (1997) (St. Petersburg) [Phys. Solid State **39**, 1366 (1997)].
[14] S. V. Gorbunov, K. N. Giniyatulin, A. V. Kruzhalov *et al.*, Fiz. Tverd. Tela (Leningrad) **28**, 606 (1986) [Sov. Phys. Solid State **28**, 340 (1986)].

Translated by M. E. Alferieff

Theory of the Lesage–Jeans instability in a linear chain of dust particles in plasma

A. E. Dubinov, D. V. Selemir, and V. Sh. Shaĭdullin

Russian Federal Nuclear Center, All-Russia Scientific-Research Institute of Experimental Physics; M. V. Lomonosov Moscow State University

(Submitted April 27, 1999)
Pis'ma Zh. Tekh. Fiz. **25**, 84–89 (September 12, 1999)

The dynamics of the Lesage–Jeans instability in a linear infinite periodic chain of dust particles in plasma is studied theoretically by deriving and numerically solving the nonlinear wave equation. [S1063-7850(99)01509-8]

The dynamics of the dust component has recently been actively investigated in plasma physics. It It was found to be so unusual that in a number of cases it is difficult to find familiar analogs compatible with its collective motion. An enormous number of facts confirming this thesis can be marshalled. We indicate only the most dramatic:

formation of a stable ordered structure of dust particles in plasma—plasma–dust crystal (see reviews Refs. 1 and 2);

tendency of a dust plasma to self-compress and assume a compact form.[3]

A new direction in investigations of plasma-dust crystals has already been formulated—plasma–dust crystallography. The number of works in this field in now in the hundreds, whereas we know of very few works on the instability of self-compression of dust plasma and its compact state.[3,4] At the same time, it is this instability that is most interesting for practical purposes, for example, for increasing the confinement time of a low-temperature plasma in a compact form.

The reason for crystallization and self-compression of the dust component can be indicated at an elementary level: the existence of long-range attractive forces between the dust particles. The mechanism leading to the appearance of such forces, proposed in Refs. 5–7 and based on the relative shadowing of the ion and dust fluxes, gives rise to an interaction similar to gravity

$$F_{1,2} \propto n T_i \frac{a_1^2 a_2^2}{R^2}, \tag{1}$$

where n is the plasma concentration, T_i is the ion temperature of the plasma, a_1 and a_2 are the radii of the dust particles, and R is the distance between the centers of the dust particles. As indicated in Ref. 6, this formula was derived in the 18th century by Lesage, who attempted to explain gravity on the basis of the ether concept.

The results of experimental investigations[8,9] confirming the existence of attractive forces between macrobodies in a plasma are consistent on the whole with theoretical ideas.[5–7]

It is easy to see that in the presence of attraction a Jeans instability can develop in an ensemble of dust particles in plasma. In addition, self-compression can be regarded as a particular case of this instability. Since, as will be shown below, for a dust plasma this instability has certain special features that distinguish it from the classical gravitational instability, we decided to call it the Lesage–Jeans instability.

The aim of the present work was to investigate theoretically the dynamics of this instability in a linear infinite periodic chain of dust particles in plasma, the most illustrative configuration which admits a simple solution. Such chains (of course, with a finite number of dust particles) have been obtained experimentally and investigated in Refs. 10 and 11.

In what follows, the nonlinear wave equation describing the instability is derived, and an example of its numerical solution is presented.

Let us consider an infinite periodic chain of identical spherical dust particles in an isotropic and uniform unbounded collisionless plasma. The collisionless nature of the plasma presupposes that the mean free path of all plasma particles in the absence of the dust particles is much longer than all characteristic length scales in the problem. We shall assume that the period d in the chain and the radius a of the dust particles satisfy $d < a \ll r_d$, where r_d is the Debye radius. The geometry of the problem is shown in Fig. 1.

Let us determine the force acting on an individual dust particle. This force consists of the mutual attractive forces with two neighboring dust particles, one on each side. It is important that the subsequent dust particles do not interact with the dust particle under consideration, since they are located in the geometric shadow of the dust particles closest to it. This shadowing (or in other words, screening) is the key point that distinguishes the problem under study from the classical gravitational Jeans instability.

Therefore each dust particle interacts according to the law (1) with only its nearest neighbors. Therefore the Toda-chain formalism is entirely applicable to this chain.[12]

It is easy to see that the periodic chain is in equilibrium, since the attractive forces on both sides of each dust particle balance one another. However, a small perturbation will take the system out of equilibrium.

We write the equation of motion of the $(n+1)$-st and nth dust particles as

$$\frac{d^2\Delta_{n+1}}{dt^2} = \frac{\mu}{m}\left(\frac{1}{x_{n,n+1}^2} - \frac{1}{x_{n+1,n+2}^2}\right), \tag{2}$$

$$\frac{d^2\Delta_n}{dt^2} = \frac{\mu}{m}\left(\frac{1}{x_{n-1,n}^2} - \frac{1}{x_{n,n+1}^2}\right), \tag{3}$$

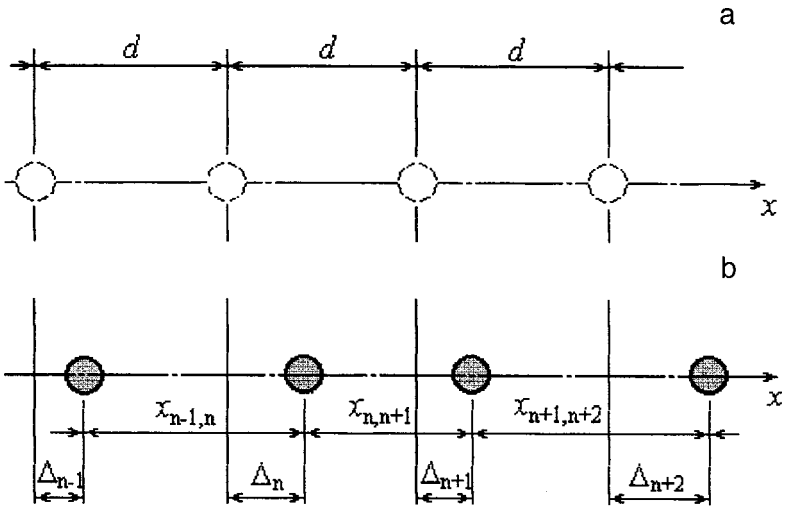

FIG. 1. Geometry of the problem: a—Unperturbed position of the dust particles; b—instantaneous position of the dust particles during the development of the instability.

where Δ_n is the displacement of the nth dust particle from its position of equilibrium, $x_{n,m}$ is the instantaneous distance between the nth and mth dust particles, and $\mu \propto nT_i a^2$ is the constant force (1). Subtracting Eq. (3) from Eq. (2) gives

$$\frac{d^2}{dt^2}(d+\Delta_{n+1}-\Delta_n) = -\frac{\mu}{m}\left(\frac{1}{x_{n+1,n+2}^2} - \frac{2}{x_{n,n+1}^2} + \frac{1}{x_{n-1,n}^2}\right). \tag{4}$$

We note that the function $d+\Delta_{n+1}-\Delta_n = x_{n,n+1}$ appears on the left-hand side of Eq. (4).

We now transform from a discrete chain to its continuous analog. For this, it is convenient to introduce a linear dust particle density $\rho = x^{-1}$. Then Eq. (4) can be rewritten as

$$\frac{d^2}{dt^2}\rho_{n+1,n}^{-1} = -\frac{\mu}{m}(\rho_{n+1,n+2}^2 - 2\rho_{n,n+1}^2 + \rho_{n-1,n}^2). \tag{5}$$

The expression in parentheses in Eq. (5) is the difference form of the second derivative with respect to the spatial variable x. Therefore we can write

$$\frac{d^2}{dt^2}\rho^{-1} + \frac{\mu}{m}\frac{d^2}{dx^2}\rho^2 = 0, \tag{6}$$

and performing the differentiation we obtain finally the desired wave equation

$$\rho\rho_{tt} - 2\rho_t^2 + \frac{\mu}{m}(\rho^3\rho_x^2 + \rho^4\rho_{xx}) = 0. \tag{7}$$

This equation together with the profiles of the initial perturbation $\rho(x,0)$ and $\rho_t(x,0)$ constitutes a Cauchy problem, which makes it possible to describe the dynamics of the Lesage–Jeans instability of an infinite chain of dust particles in plasma.

As an example, we consider a localized perturbation of the chain

$$\rho(x,0) = \rho_0 + \frac{\rho'(x/b)}{1+(x/b)}, \quad \rho_t(x,0) = 0, \tag{8}$$

where ρ' and b are constants such that $\rho' \ll \rho_0 = d^{-1}$ and $b \ll d$.

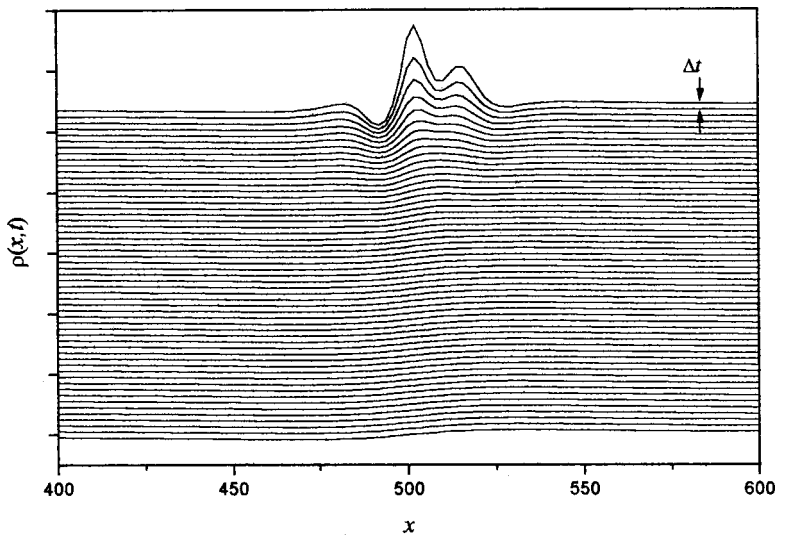

FIG. 2. Evolution of the density distribution.

The problem (7)–(8) was solved numerically by the factorization method. In so doing, the time scale $t_0=(m/\mu)^{1/2}$ was used to represent Eq. (7) in dimensionless form. The relative integration error was less than 10^{-10}. Figure 2 shows the evolution of the density distribution ρ with time step $\Delta t=0.005$.

Figure 2 clearly shows the tendency of the system of dust particles to cluster together, which qualitatively agrees with the well-known Jeans gravitational instability. However, as a result of screening, the growth rate of the Lesage–Jeans instability is nevertheless appreciably smaller.

[1] V. N. Tsytovich, Usp. Fiz. Nauk **167(1)**, 57 (1997).
[2] A. P. Nefedov, O. F. Petrov, and V. E. Fortov, Usp. Fiz. Nauk **167(11)**, 1215 (1997).
[3] V. N. Tsytovich and D. Rezendes, Fiz. Plazmy **24**(1), 71 (1998) [Plasma Phys. Rep. **24**, 65 (1998)].
[4] A. M. Ignatov, Fiz. Plazmy **22**(8), 731 (1998) [Plasma Phys. Rep. **24**, 677 (1998)].
[5] A. M. Ignatov, Kratk. Soobshch. Fiz. FIAN, No. 1–2, 58 (1995).
[6] A. M. Ignatov, Fiz. Plazmy **22**(7), 648 (1996) [Plasma Phys. Rep. **22**, 585 (1996)].
[7] Ya. K. Khodataev, R. Bingham, V. P. Tarakanov, and V. N. Tsytovich, Fiz. Plazmy **22**(11), 1028 (1996) [Plasma Phys. Rep. **22**, 932 (1996)].
[8] A. E. Dubinov, V. S. Zhdanov, A. M. Ignatov *et al.*, Kratk. Soobshch. Fiz. FIAN, No. 7–8, 40 (1997).
[9] A. E. Dubinov, V. S. Zhdanov, A. M. Ignatov *et al.*, in *Proceedings of a Conference on the Physics of Low-Temperature Plasma, ''Plasma, 20th Century,''* Petrozavodsk, 1998, p. 701.
[10] S. Peter, A. Homann, A. Melzer, and A. Piel, Phys. Lett. A **223**, 389 (1996).
[11] A. Homann, A. Melzer, S. Peter, and A. Piel, Phys. Rev. E **56**, 7138 (1997).
[12] M. Toda, *Theory of Nonlinear Lattices*, 2nd ed. (Springer, New York, 1989; Mir, Moscow, 1984).

Translated by M. E. Alferieff

On the conditions for contraction of a multielectrode corona discharge in He/Ar, Kr, Xe mixtures

A. K. Shuaibov

Uzhgorod State University
(Submitted April 30, 1999)
Pis'ma Zh. Tekh. Fiz. **25**, 90–94 (September 12, 1999)

The results of an investigation of the contraction of a corona discharge in ''needle–grid'' and ''needle–plane'' electrode systems maintained by a constant negative voltage are presented. The discharge was ignited in working media of infrared lasers on $p-d$ transitions of atoms of heavy inert gases (He/Ar, Kr, Xe mixtures). Investigation of the current–voltage characteristics showed that in the mixtures He/Ar/Kr there is no hysteresis on the rising section of the current–voltage characteristic, while hysteresis does appear for a corona discharge in the mixture He/Xe. For voltages $\geqslant 5.5$ kV on the needles and ballast resistance $R_b \geqslant 0.5$ MΩ dynamical contraction of a corona discharge together with current pulses with $f=3-5$ kHz and hysteresis loops were found on the descending section of the curve $I=f(U)$, where I and U are the average current and voltage on the discharge gap. The maximum content of atoms of heavy inert gases for [He]=200–300 kPa is [Ar]$\leqslant$12, [Kr]$\leqslant$8, and [Xe]$\leqslant$4 kPa. © *1999 American Institute of Physics.* [S1063-7850(99)01609-2]

A multielectrode corona discharge (CD) ignited in ''needle–grid (plane)'' electrode systems with the mixtures He/Ar, Kr, Xe=100/1 ($P=100-350$ kPa) using a stationary negative voltage exists in the form of a spatially uniform plasma close to a transverse glow discharge.[1] The attained power densities fed into the plasma, $\leqslant 1$ W/cm^3, make such discharges promising for the development of simple lasers based on $p-d$ and $p-s$ transitions of heavy inert gases (R) in a stationary operating state.[2] The main factor preventing the development of such lasers is the nonthermal contraction of this CD, manifested at high supply voltages and content R. The contraction of a discharge in inert gases (for $P \leqslant 10$ kPa) has been investigated in greatest detail in a stationary longitudinal discharge and appeared as a contraction of current to the center of the cylindrical discharge tube.[3–5] It ws was shown that the contraction appears in the form of stationary and dynamic regimes, and the dynamic regime is accompanied by current pulsations ($f=5-10$ kHz) in the presence of a megohm ballast resistance in the supply circuit. Contraction of a stationary high-pressure discharge obtained in working media $R(p-d;p-s)$ with a nearly transverse electrode system of a CD has not been studied.

In the present letter we report the results of an investigation of the conditions of contraction of a multielectrode CD in the working media of high-pressure electric-discharge lasers using atoms of heavy inert gases.

The CD was ignited in two extended electrode system of the ''needle–plane'' (unipolar, UP) and ''needle–grid'' (bipolar, BP) types up to 5 cm long. The interelectrode distance was 2 cm. The electrode system consisted of two rows of needles with a 0.5 mm tip radius and with the needles (and rows of needles) separated by 1 cm. The other experimental conditions are similar to those described in Refs. 2 and 6.

Figures 1 and 2 show the CVCs of a CD in the mixtures He/R with different pressures. All CVCs of the CD in the mixtures He/Xe had a rising dependence $I=f(U)$ and hysteresis, which appeared even with near-threshold driving voltages. At high He/Xe mixture pressures ($P \geqslant 250$ kPa) the CVC was nearly quadratic, $I=\alpha(U-U_0)^2$, where α is a constant and U_0 is the ignition potential of the discharge. For $P \leqslant 150$ kPa the region of stable existence of these CDs with respect to the magnitude of the voltage on the discharge gap decreased from 2.0 to 0.3 kV, and the CVC acquired a linearly rising form similar to the CVC of a recombination-controlled glow discharge (under our conditions this is a dissociative recombination reaction of R_2^+ ions with slow electrons).[7] For $U=6.3$ kV and mixture pressure $P=300$ kPa (curves *3* and *4* in Fig. 2) contraction of the discharge was observed, expressed as fading of a uniform discharge between conical needles and a grid (or plate) and formation of a bright current channel at the point where the voltage is applied to the needles. Negative-resistance regions (negative slope of the CVC) were not observed, and a discharge with $U \leqslant 6.3$ kV burned in a stationary regime.

When the Xe atoms were replaced by lighter Ar and Kr atoms, hysteresis vanished almost completely on the initial section of the CVC and negative-resistance regions appeared. Contraction of the discharges in the range $U=6.0-6.3$ kV was accompanied by current pulsations with frequency $f=3-5$ kHz and was not as distinct. A current channel in this range of U existed against the background of a glow discharge, whose radiation brightness and uniformity decreased substantially. For all cases the ignition potential of the BP CD was 1.0–1.5 kV lower than for a UP CD in the same working mixture. Adding a small quantity (20–50 Pa) of hydrogen chloride molecules eliminated the current hysteresis in the CVC. In this case the discharge retained its bulk character, but the maximum current at the uncontracted stage

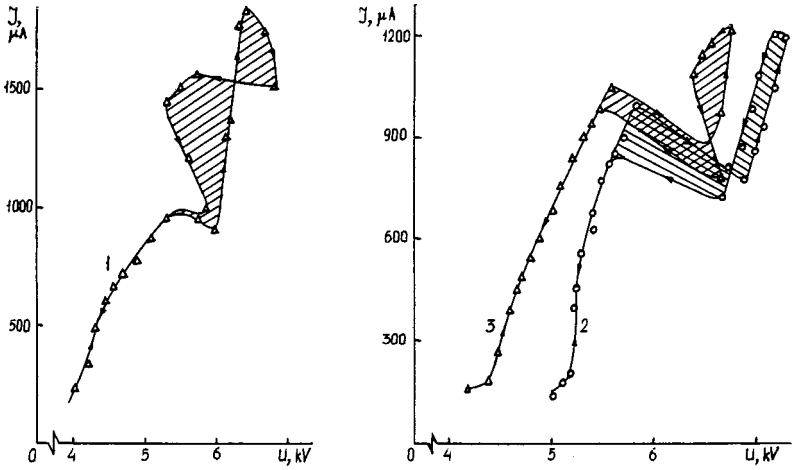

FIG. 1. CVCs of a negative CD in the ''needle–grid'' (*1*, *3*) and ''needle–plane'' (*2*) electrode systems. The discharge was ignited in the mixtures He/Ar=300/2.8 (*1*) and He/Kr=300/2.8 kPa (*2*, *3*).

decreased by a factor of 1.5–2. The appearance of current hysteresis for a CD in inert gases is due mainly to metastable atoms R(m) and molecules $R_2(m)$ which enter into a chemiionization reaction with one another.[8] For this reason, the presence of HCl molecules in plasma (due to efficient ''harpoon'' reactions with formation of excimer molecules (RCl*)[9] and quenching R(m) by HCl molecules) decreases the density of metastable atoms R and hysteresis vanishes.

Depending on the kind and content of R atoms in the gas mixtures, the conditions of a transition of a CD into a contracted state change. In our experiment, for high He pressures in the mixtures ($P \geqslant 200$ kPa) an uncontracted discharge was ignited for [Xe]$\leqslant$4, [Kr]$\leqslant$8, and [Ar]$\leqslant$12 kPa. The appearance of current pulsations in some regimes of a given CD can be interpreted as a manifestation of dynamic contraction of the discharge similarly to a longitudinal average-pressure glow discharge in Ar.[3] In this case the current pulsations are due to the presence of a negative-resistance section in the CVC and buildup of self-excited oscillations (with a ballast resistance $R_b \geqslant 0.5$ MΩ), since the electric circuit of the discharge always possesses a parasitic inductance and capacitance ($C=50-100$ pF), forming the oscillatory system.

The physical reasons for contraction of a given discharge are the nonlinear dependence of the ionization rate (chemiionization R(m) and $R_2(m)$) on the electron density, the presence of Coulomb collisions, and nonuniform heating of the gas medium. A detailed quantitative investigation of the mechanism leading to the contraction of a multielectrode CD requires numerical simulation of the kinetics of the processes in the plasma and calculation of the discharge characteristics.

In summary, the investigation of contraction of a multielectrode CD in the working media of lasers on R($p-d$) (the mixtures He/Ar, Kr, Xe=100/1; $P=100-300$ kPa) showed that the CVCs of the discharge are characterized by hysteresis, while in He/Ar, Kr mixtures negative-resistance sections are observed and lead to the development of self-excited oscillations in the system (current pulsations $f=3-5$ kHz) when a certain value of U, the mixture pressure, or the content of atoms of heavy inert gases is exceeded.

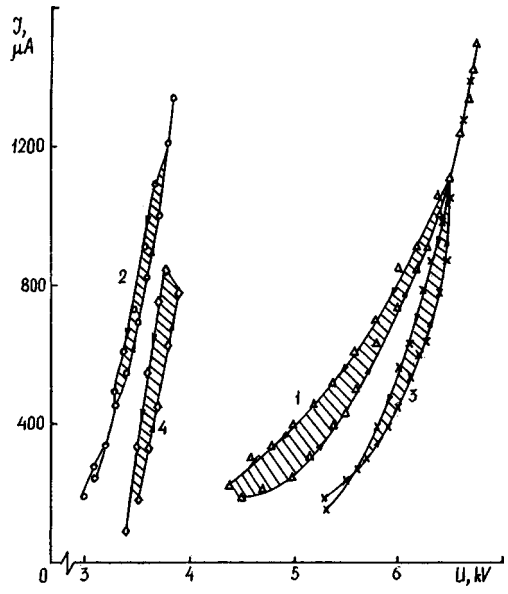

FIG. 2. CVCs of a CD in the mixtures He/Xe=300/4 (*1*, *3*) and 150/4 kPa (*2*, *4*): *1*, *2*—bipolar; *3*, *4*—unipolar.

[1] A. K. Shuaibov and I. V. Shevera, Zh. Tekh. Fiz. **67**(11), 15 (1997) [Tech. Phys. **42**, 1254 (1997)].
[2] A. K. Shuaibov, I. V. Shevera, and A. I. Dashchenko, Kvantovaya Elektron. **24**, 519 (1997).
[3] N. I. Lipatov, A. P. Mineev, V. I. Myshenkov *et al.*, Zh. Tekh. Fiz. **55**, 1730 (1985) [Sov. Phys. Tech. Phys. **30**, 1011 (1985)].
[4] A. V. Eletskiĭ and R. V. Chiflikyan, in *Reviews of Plasma Chemistry*, *Vol. 15*, Ed. B. M. Smirnov (Consultants Bureau, New York, 1994; Energoatomizdat, Moscow, 1988, pp. 266–293).
[5] Yu. B. Golubovskiĭ, V. O. Nekuchaev, and E. B. Pelyukov, Zh. Tekh. Fiz. **66**(3), 43 (1996) [Tech. Phys. **41**, 254 (1996)]; **66**(10), 76 (1996) [**41**, 1011 (1996)].
[6] A. K. Shuaibov, A. I. Dashchenko, I. V. Shevera, and A. I. Minya, Fiz. Plazmy **23**, 960 (1997) [Plasma Phys. Rep. **23**, 886 (1997)].
[7] Yu. P. Raĭzer, *Gas Discharge Physics* (Springer, New York, 1991) [Russian orig. Nauka, Moscow, 1987].
[8] A. A. Belevtsev, in *Abstracts of Reports at the 4th All-Union Conference on the Physics of Gas Discharges*, Makhachkala, Dagestan State University, Part 1, pp. 15–16.
[9] A. K. Shyaibov, Zh. Prikl. Spektrosk. **65**, 205 (1998).

Translated by M. E. Alferieff

1/*f* Noise in inhomogeneous condensed media: relation with a nonequilibrium phase transition

Yu. V. Gudyma

Yu. Fed'kovich Chernovtsy State University
(Submitted April 15, 1999)
Pis'ma Zh. Tekh. Fiz. **25**, 1–5 (September 26, 1999)

An approach in which the spectral density of a noise signal, varying inversely as the frequency with a fractal exponent close to 1, is due to the inhomogeneity of the medium is proposed. In the critical region the nucleation process serves as the source of inhomogeneity. © *1999 American Institute of Physics.* [S1063-7850(99)01709-7]

An enormous amount of information on observations of $1/f$ noise in various, often completely dissimilar, systems has now been accumulated.[1–3] Especially valuable in this respect are recent experiments on the observation of such fluctuations near a nonequilibrium first-order phase transition.[4–6] It is now clear that the existence of $1/f$ noise cannot be unambiguously attributed to the existence of a continuous spectrum of relaxation times with a uniform distribution of their logarithm in the system. The lack of theoretical concepts which are adequate for the phenomenon under study is stimulating an intense search for a satisfactory solution of this problem.

This letter proposes an approach that assumes the noise signal, whose spectral density varies inversely as the frequency with fractal exponent close to 1, due to phase transformations to be directly related with an inhomogeneity whose source is nucleation. A quite general model of an inhomogeneous condensed medium is considered: nuclei of a different phase which are randomly distributed in a uniform matrix. The random motion of charge carriers has a microscopically short characteristic time scale: the free travel time τ_k between two nearest clusters. Thus, $1/f$ noise can be represented as a random sequence of pulses associated uncorrelated motion in the matrix being replaced by correlated motion in the nuclei. It is obvious that they (the pulses) all have approximately the same form. The correlation function of the stationary process can be simply approximated as[7]

$$\varphi(t)=\langle(\Delta n/n)^2\rangle\exp(-\omega|t|), \tag{1}$$

where $[\langle(\Delta n/n)^2\rangle]^{1/2}$ is the rms fluctuation of the carrier density. Since in the present case the decrease of the correlation function is characterized by a relaxation time $1/\omega(1/L)$, where L is the characteristic size of the critical nuclei, the desired function of time has the form

$$\varphi(t)=\int_{-\infty}^{+\infty}\langle(\Delta n/n)^2\rangle\exp(-\omega(\tau/L)t)d^4(r/L), \tag{2}$$

where d is the dimension of the space.

In the region of strong fluctuations (close to a phase transition) the correlation radius becomes greater than any linear dimension, including the critical dimensions of the nuclei. As a result, the similarity hypothesis for critical fluctuations can be applied to the quantity under study and its relaxation time:

$$\langle(\Delta n/n)^2\rangle=\overline{(\Delta n)^2}n^{-2}x^{-2\alpha},\quad \omega(x)=\lambda x^{-\beta},\quad x=r/L, \tag{3}$$

and since the function $\varphi(t)$ is even and positive-definite, we put the expression (2) into the form

$$\varphi(t)=2\int_0^{\infty}\overline{(\Delta n)^2}n^{-2}x^{-2\alpha}\exp(-\lambda x^{-\beta}t)d^dx. \tag{4}$$

Here $\overline{(\Delta n)^2}$ is the mean-square amplitude of the carrier-density fluctuations. The approximation (3) actually means that we assume not only the charge carrier density but also the related energy to be anomalously fluctuating quantities.

Performing the integration and using the identity $\Gamma(z)\Gamma(1-z)=\pi/\sin(\pi z)$, we obtain the final expression for the correlation function

$$\varphi(t)=8\pi^2\overline{(\Delta n)^2}n^{-2}\beta^{-1}(\lambda t)^{-\frac{2\alpha-d}{\beta}}\times\left[\Gamma\left(1-\frac{2\alpha-d}{\beta}\right)\sin\left(\pi\frac{2\alpha-d}{\beta}\right)\right]^{-1}, \tag{5}$$

which is valid with the natural bound $2\alpha-\beta<d$. Integrals of this type have been encountered in calculations of the relaxation of a system with ''residual'' memory.[8]

Since the events are independent, it can be assumed that the quantities τ_k are distributed according to Poisson's law. Electrons in a nucleus of a new phase are described by the function (2); for $x>1$, for simplicity, we shall assume the motion to be completely uncorrelated (in principle, a zero reference level is not necessary; it is sufficient that the correlation of the motion be constant outside nuclei). Then the noise signal is a linear superposition of individual pulses

$$F(t)=\sum_k\varphi(t)\theta(t-\tau_k), \tag{6}$$

where $\theta(t-\tau_k)$ is a unit step function, equal to 1 for $t>\tau_k$ and zero for $t<\tau_k$. The appearance of a random process of the form (6) is a result of single scattering of current carriers

by inhomogeneities (nuclei) randomly dispersed in the medium. In accordance with Carson's theorem,[9] the spectral density of the signal can be represented as

$$\overline{S_x(f)} = 2\nu|\Phi(f)|^2. \tag{7}$$

Here $\Phi(f)$ is the Fourier transform of the shape function of a single pulse, ν is the average frequency of events, and the overbar on the left side of the expression signifies averaging over a large number of tests (i.e., an average over a set).

After appropriate transformations, for $(2\alpha - d)\beta \to 1/2$ we obtain

$$\overline{S_x(f)} \to 16\pi^2 \nu \beta^{-1} \lambda^{-1/2} \overline{(\Delta n)^2} n^{-2} f^{-1}. \tag{8}$$

We note that the advances made in the theory of self-organization are based mainly on the fact that dissipative thermodynamically nonequilibrium systems in a stationary state with detailed balance are formally indistinguishable from nonquilibrium systems.[10] The existence of detailed balance in a system is equivalent to the condition that the functional of the distribution be represented in a potential form. This means, for example, that

$$P(n) = Ae^{-Y(n)}. \tag{9}$$

The mean-square of the fluctuation deviation of the carrier density should be determined for the functional (9). For low nonequilibrium carrier densities

$$V(n) = V(0) - \frac{\beta n^2}{2}. \tag{10}$$

The distribution (9) in this case becomes Gaussian, and the expression (8) becomes

$$\overline{S_x(f)} \to 8\pi^2 \nu \beta^{-1} \lambda^{-1/2} N^{-1} f^{-1}. \tag{11}$$

The exponent of the frequency for real phase transitions is of the order of 1.6. In the present theory it is obtained by choosing appropriate values for α and β. The theory presented above relates the indicated exponent with the fractal geometry of the phase space. The expression (11) correctly describes the increase in the noise amplitude with increasing inhomogeneity of condensed media and corresponds to Hooge's empirical law, whence it follows that the spectral density of $1/f$ noise is inversely proportional to the total number of charge carriers in the sample.[9] The theoretical result of this work agrees with the results of investigations performed in the last few years, which relate the nature of $1/f$ noise in random media to internal disorder in such systems.[11] The spectral composition of $1/f$ noise does not depend on the geometric dimensions of the system as a whole or on the dimensions of the clusters which appear.

In accordance with Eq. (1) $1/f$ noise should be regarded to be stationary process. This result can be used to explain the low-frequency critical nonequilibrium regime,[4–6] if the nuclei of a new phase are assumed to be the source of the inhomogeneity. Real calculations in the latter case must be modified to take account of the effect of evolution of such nuclei on the noise process under study. In addition, the true distribution (9) should be used in the expression (8). All this complicates the computational problem, but it will not be reflected in the fundamental results of the present analysis.

The conventional interpretation of $1/f$ noise as a superposition of a large number of Lorentzian spectra has been criticized in Ref. 12. Different aspects of the model of $1/f$ noise as a random series of pulses, which was employed in our work, have been discussed in Refs. 12 and 13.

[1] M. B. Weissman, Rev. Mod. Phys. **60**, 537 (1988).
[2] M. J. Kirton and M. J. Uren, Adv. Phys. **38**, 367 (1989).
[3] G. P. Zhigal'skiĭ, Usp. Fiz. Nauk **167**, No. 6, 623 (1997).
[4] V. P. Koverda, V. N. Skokov, and V. P. Skripov, JETP Lett. **63**, 775 (1996).
[5] V. P. Koverda, V. N. Skokov, V. P. Skripov, Zh. Éksp. Teor. Fiz. **113**, 1748 (1998) [JETP **86**, 953 (1998)].
[6] L. A. Bityutskaya and G. D. Seleznev, Pis'ma Zh. Tekh. Fiz. **24**(14), 24 (1998) [Tech. Phys. Lett. **24**, 551 (1998)].
[7] L. D. Landau and E. M. Lifshitz, *Statistical Physics* (Pergamon Press, New York) [Russian original, Nauka, Moscow, 1995].
[8] R. R. Nigmatullin, Fiz. Tverd. Tela (Leningrad) **27**, 1583 (1985) [Sov. Phys. Solid State **27**, 958 (1985)].
[9] M. J. Buckingham, *Noise in Electronic Devices and System* (Ellis Horwood Limited, John Wiley Sons, New York, 1983; Mir, Moscow, 1986).
[10] H. Haken, *Advanced Synergetics* (Springer-Verlag, Berlin, 1983; Mir, Moscow, 1985).
[11] K. V. Abkemeier and D. G. Grier, Phys. Rev. B **54**, 2723 (1996).
[12] F. N. Hooge and P. A. Bobbert, Physica B **239**, 223 (1997).
[13] A. G. Gudarin, Dokl. Akad. Nauk SSSR **359**, 615 (1998) [Doc. Ophthalmol. Proc. Ser. **43**, 218 (1998)].

Translated by M. E. Alferieff

Ti:Al_2O_3 laser pumped by radiation from a copper-vapor laser

S. V. Kruzhalov, Yu. M. Mokrushin, and V. A. Parfenov

St. Petersburg State Technical University
(Submitted May 14, 1999)
Pis'ma Zh. Tekh. Fiz. **25**, 6–11 (September 26, 1999)

A scheme enabling spatial matching of copper-vapor laser radiation, which pumps a mode of an Al_2O_3:Ti laser cavity, has been developed and implemented. It is shown that copper vapor lasers as pump sources for titanium–sapphire lasers are fully capable of competing with conventional pump sources. © *1999 American Institute of Physics.* [S1063-7850(99)01809-1]

Titanium sapphire ($Al_2O_3:Ti^{3+}$) lasers remain among the most promising lasers for obtaining near-IR radiation (680–1100 nm) as well as UV and blue-green radiation using nonlinear frequency conversion.[1] Numerous works devoted to their investigation have made it possible to produce a tunable radiation source with unique characteristics. Titanium–sapphire lasers can operate in the most diverse regimes — single-frequency, mode-locking, with frequency tuning — in pulsed and in continuous-wave regimes.

The absorption curve of the active medium of this laser has a maximum near 500 nm,[2] so that in most works argon laser radiation (515, 488 nm) and the second harmonic of the YAG:Nd laser (532 nm) are used for pumping it. The few existing works on coherent pumping of an Al_2O_3:Ti laser by a copper-vapor laser[3] have not been further elaborated; the output power level and efficiency attained in them are much lower than those of the systems mentioned above.

In our view, the current situation does not correspond to the potential possibilities of copper lasers, since among commercial systems they make it possible to obtain the highest average power level in the visible range (up to 70 W) using simple power supply and cooling sources. The periodic-pulse operating regime characteristic of copper lasers provides a high rate of pumping of the active medium and makes it easier to satisfy the lasing conditions.

Among the factors that can negatively affect the efficiency of such lasers in practice, we note the large diameter of the output beam, which makes it difficult to match the pump field and a cavity mode of Al_2O_3:Ti laser, and the presence of two separated lines ($\lambda_1 = 510.6$ nm and λ_2

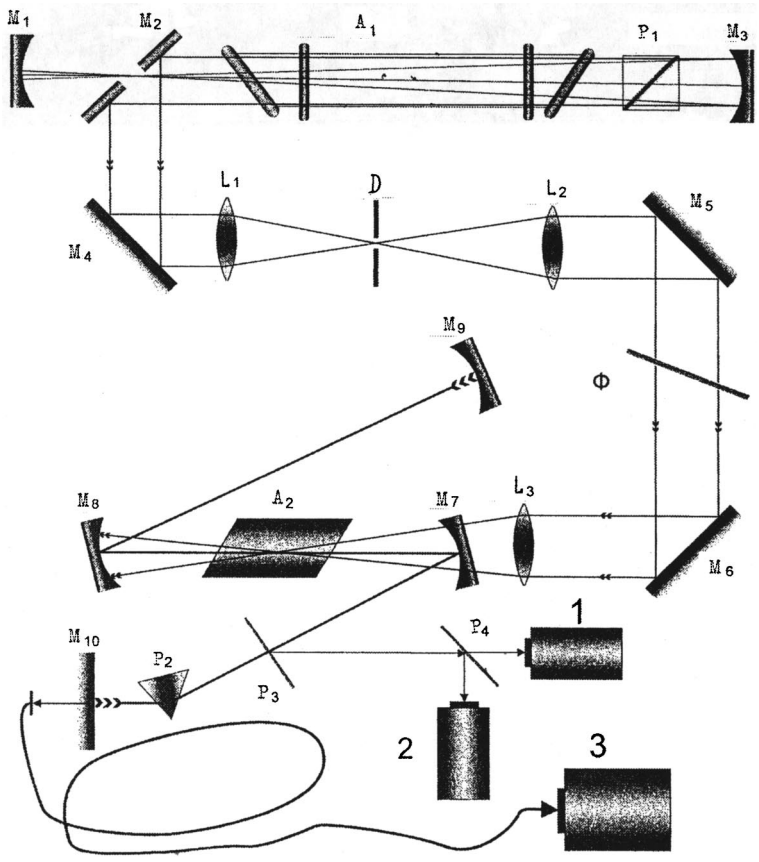

FIG. 1. Experimental arrangement.

$=578.2$ nm) with strongly different absorption cross sections ($\sigma_1 = 8.3\times10^{-20}$ cm^2 and $\sigma_2 = 3.8\times10^{-20}$ cm^2) in the emission spectrum.

Our objective in the present work is to develop a scheme that would make it possible to obtain spatial matching of the pump beam with a mode of the Al_2O_3:Ti cavity and to compare the efficiency of pumping of the Al_2O_3:Ti laser by two different spectral emission lines of a copper-vapor laser.

The experimental arrangement is displayed in Fig. 1. A GL-201 sealed gas-discharge tube was used as the active component A_1. A polarization prism P_1 placed inside the cavity gave the required polarization of the radiation. An unstable telescopic cavity with gain $M = R_3/R_1 \approx 37$, where R_1 and R_3 are the radii of curvature of the mirrors M_1 and M_3, was used to decrease the divergence of the copper-laser radiation. In addition, an inverted telescope, formed by the lenses L_1 and L_2, was positioned in the path of the beam extracted from the cavity using a flat mirror M_2 containing a coupling opening. A diaphragm D operating as a spatial filter was placed at the focal point of the lenses L_1 and L_2. These measures decreased the divergence of the radiation to 3.5×10^{-4} rad. Replaceable dichroic mirrors Φ made it possible to vary the ratio between the green and yellow components of the pump spectrum, as required to determine their relative efficiency.

The copper laser operated at 15.6 kHz and generated 20 ns light pulses. The average power measured after the mirror M_7 reached a 7 W level with the green/yellow ratio of 3/4.

The cavity of the titanium–sapphire laser consisted of a standard Z-shaped scheme with compensation of astigmatism. A 5 mm in diameter and 15 mm long Al_2O_3:Ti^{3+} active element A_2 with Brewster ends was placed between the spherical mirrors M_7 and M_8 with 10 cm radii of curvature. The transmission of the active element was $T_{p_1} = 1.8\%$ at $\lambda_{p_1} = 510.6$ nm and $T_{p_2} = 16.8\%$ at $\lambda_{p_2} = 578.2$ nm. The distances between the mirrors $M_7 - M_{10}$ and $M_8 - M_9$ were 30 cm. The reflection coefficients of all mirrors at the center of the tuning range exceeded 99%. The pump radiation passed through the lens L_3 with focal length 20 cm and was directed through the mirror M_7 with high transmission in the pump range onto the active element A_2. A measurement of the intensity distribution of the pump radiation in the waist showed that the light spot is a circle with a diameter of approximately 100 μm, close to the size of the cavity mode. Two mirror assemblies for the ranges 680–850

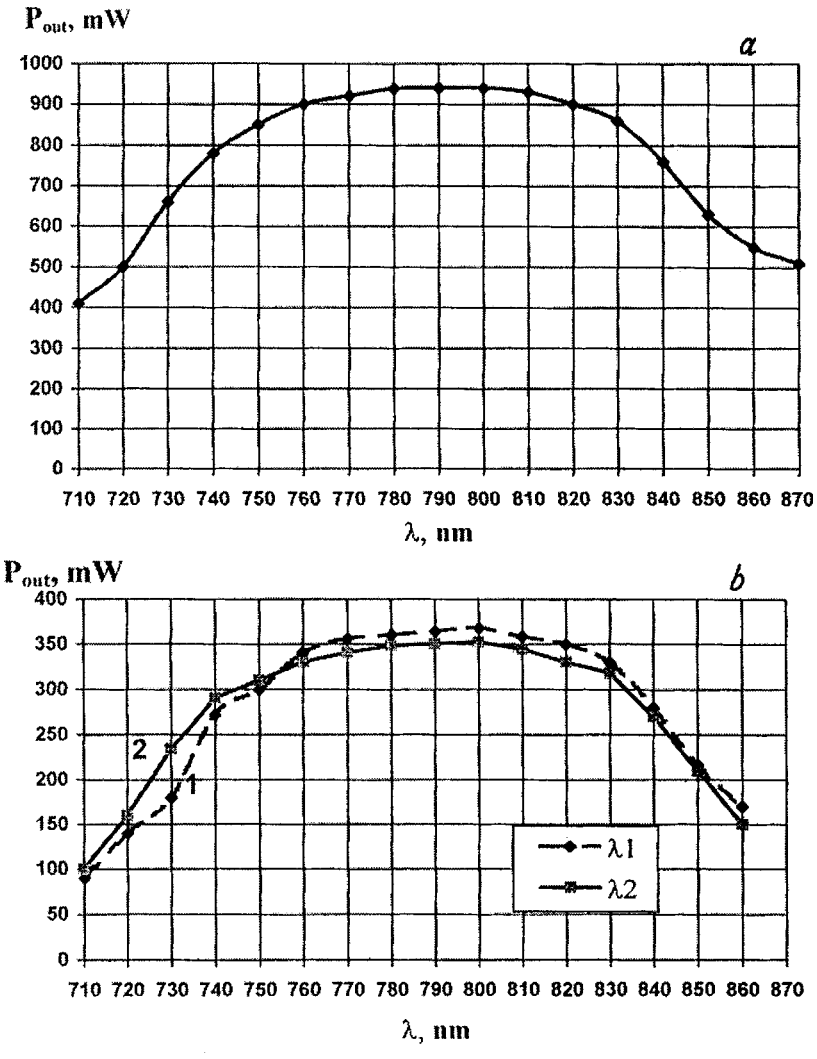

FIG. 2. Output power of a titanium–sapphire laser versus the lasing wavelength: a — Pumping by both emission lines simultaneously; b — separate pumping, $\lambda_1 = 510.6$ nm and $\lambda_2 = 578.2$ nm.

and 850–980 nm were used in the experiments. A Brewster glass prism P_2 was used to tune the lasing wavelength and a thin plane-parallel glass plate P_3, set at an angle to the axis of the cavity of the titanium–sapphire laser, was used to extract radiation from the cavity. Power meters *1* (IMO-2) were used to measure the average lasing and pump powers. A photocell *2* (PK-19) was used to record the temporal characteristics of the radiation. Radiation was directed along a lightguide to the input of the spectrometer *3* (SFK-601) to measure the wavelength.

The tuning characteristics were studied at a 16% cavity load, determined by rotating the plate P_3. The lasing region obtained with the mirror assemblies was 710–970 nm. As an illustration, the tuning characteristic of an $Al_2O_3:Ti^{3+}$ laser using a mirror assembly whose spectral characteristic was centered at $\lambda = 790$ nm is presented in Fig. 2a. The total pump power in both lines was 6 W in this case.

The spectral characteristics of the laser pumped separately with $\lambda_1 = 510.6$ nm and $\lambda_2 = 578.2$ nm radiation are presented in Fig. 2b. We note that the pump power in each line was 3 W. As one can see from the plots presented, despite the strong difference in the absorption cross sections, the efficiency of conversion of the pump radiation and the tuning ranges are essentially the same in both cases.

The results obtained can be explained using an expression for the differential efficiency[4,5]

$$\eta = \frac{\lambda_p}{\lambda_g} \times \frac{T}{(T+\delta)} \times (1 - T_p), \tag{1}$$

where λ_p and λ_g are the pump and lasing wavelengths, T are the transmission losses of the laser mirrors, δ are the passive losses in the cavity, and T_p is the transmission of the crystal at the pump wavelength.

It is easy to obtain from Eq. (1) a relation for the relative efficiency of pumping at the wavelengths λ_{p_1} and λ_{p_2}

$$\eta_1 / \eta_2 = \frac{\lambda_{p_1}}{\lambda_{p_2}} \times \frac{(1 - T_{p_1})}{(1 - T_{p_2})}. \tag{2}$$

Substituting into Eq. (2) the values of the quantities corresponding to the experimental conditions we obtain $\eta_1 / \eta_2 = 1.04$, which agrees well with our data. Actually, this means that in the two-frequency pumping case studied the effects associated with the difference of the Stokes shift and absorption in the active medium compensate one another.

The maximum output power was obtained by increasing the load to 40%, and at the center of the tuning characteristic it was $P = 1.32$ W ($\lambda = 790$ nm) for the first mirror assembly and $P = 1.2$ W ($\lambda = 900$ nm) for the second one. The differential efficiencies were 26.4 and 24%, respectively.

The output power level, the tuning range, and the efficiency obtained in this work show that copper lasers as sources for pumping titantium–sapphire lasers are fully capable of competing with the conventionally used systems. The existence of alternative pumping sources, in our view, expands the possibilities of titanium–sapphire lasers, making it possible to select the optimal variant for a specific problem.

[1] P. E. Moulton, J. Opt. Soc. Am. B No. 3, 125 (1986).
[2] R. Moncorge, G. Boulon, D. Vivien, A. M. Lejns, R. Collongues, V. Djevahirdjian, K. Djevahirdjian, and R. Cagnard, IEEE J. Quantum Electron. No. 4, 1049 (1988).
[3] S. G. Bartoshevich, V. V. Zuev, S. Yu. Mirza *et al.*, Kvant. Élektron. **16**, 212 (1989) [Sov. J. Quantum Electron. **19**, 138 (1989)].
[4] A. Sancher, A. J. Strauss, R. L. Aggarwal, and R. E. Fahey, IEEE J. Quantum Electron. **24**, 995 (1988).
[5] T. T. Basiev, P. G. Zverev, A. G. Papashvili, and V. V. Fedorov, Kvant. Elektron. (Moscow) **24**, 591 (1997).

Translated by M. E. Alferieff

^{13}C enrichment of fullerenes

D. V. Afanas'ev, G. A. Baranov, A. A. Bogdanov, G. A. Dyuzhev, A. K. Zinchenko, V. I. Karataev, and A. A. Kruglikov

A. F. Ioffe Physicotechnical Institute, Russian Academy of Sciences, St. Petersburg; Center for Laser Technology, Scientific-Research Institute for Electrophysical Apparatus

(Submitted May 24, 1999)
Pis'ma Zh. Tekh. Fiz. **25**, 12–18 (September 26, 1999)

It is shown experimentally that fullerenes can be enriched with ^{13}C as a constituent of CO_2 gas molecules. A qualitative model of the processes that correctly reflects the experimental laws is proposed. © *1999 American Institute of Physics.* [S1063-7850(99)01909-6]

In scientific research, especially in chemistry, biology, and medicine, it is convenient to have fullerenes enriched with the carbon isotope ^{13}C. This is because this isotope is a reference for nuclear magnetic resonance methods.

^{13}C-tagged fullerenes can be quite easily obtained, if graphite consisting of ^{13}C carbon is available. Preparing an anode from a mixture of such graphite with conventional graphite with 1.1% ^{13}C makes it possible to obtain different degrees of ^{13}C enrichment of fullerene in a conventional ''fullerene'' arc.[1–4] This method was used in Ref. 4, in a study of the mass spectra of fullerenes obtained in discharges with different ratios of ^{12}C and ^{13}C in the anode, to obtain the first experimental proof that fullerenes are formed from carbon atoms and not from large fragments of graphite planes, which, as was assumed, can evaporate from the anode. However, ^{13}C graphite is a unique and expensive material. $^{13}CO_2$ gas obtained by laser enrichment of freon, followed by chemical treatment, and using gas centrifuges[5] is much more readily available and cheaper. Our objective in the present work was to determine experimentally the possibility of obtaining ''tagged'' fullerenes using $^{13}CO_2$ gas.

This possibility is not at all obvious. In order for ^{13}C to be incorporated in fullerene, the cold gas enriched with the isotope must effectively seep into the hot zone of the discharge and dissociate there into atomic carbon, while the CO molecules, which are unavoidably present in the fullerene formation zone, must not radically disrupt their formation process.

The experiments were performed in the conventional fullerene production apparatus[6,7] with vertical electrodes. The electrodes consisted of 6 mm in diameter graphite rods with the natural ^{13}C content. The anode rod was secured to a mobile holder, which was inserted into the chamber through the top flange using a Wilson seal. Before the arc discharge was ignited, the chamber was evacuated and filled with the mixture He + $^{13}CO_2$; the ^{13}C content in the carbon dioxide gas was 99%. The total mixture pressure before the discharge was 100 torr, the $^{13}CO_2$ partial pressure ranged from 33 to 65 torr, the discharge current was 60 and 80 A, and the discharge duration was several minutes.

Two phases of an arc discharge are observed in the mixture He + CO_2. After ignition, soot particles are not formed for discharge burning times $t_d < \tau_0$,[7] in contrast to the conventional fullerene arc in pure helium where soot particles fill the vacuum chamber virtually uniformly even several seconds after the arc is ignited. Experimentally, not only the absence of ''smoke'' in the vacuum chamber but also the constancy of the intensity of a laser beam passed through the vacuum chamber outside the discharge zone indicated the absence of soot formation.

The absence of soot formation indicates that in the hot zone of an arc discharge carbon dioxide is converted into CO. The characteristic conversion time will be determined by the ratio of the total number of oxygen atoms in the chamber, which is proportional to the initial CO_2 pressure and the chamber volume V, to the flux of carbon atoms evaporated from the anode, which depends primarily on the discharge current and the interelectrode distance.[6] The quantity τ_0 can be determined experimentally from the attenuation of the laser radiation or it can be estimated from the formula

$$\tau_0 = \frac{p_{CO_2} \cdot V}{kT \cdot q}, \tag{1}$$

where p_{CO_2} is the initial CO_2 pressure in the chamber, T is the temperature of the chamber walls, and q is the experimental value of the erosion of the anode. For one of the investigated regimes, an estimate from Eq. (1) gives $\tau_0 = 100$ s, while the experimental value is $\tau_0 = 70$ s.

One other experimental fact indicates complete conversion of CO_2 into CO — a large increase in pressure in the chamber at the initial stage of the discharge. The pressure increase in the vacuum chamber measured after the discharge was switched off and the gas has cooled is equal to the initial CO_2 partial pressure in the mixture He + CO_2.

We note that the C binds with O not only in the discharge volume but apparently also on the anode surface, since for the same arc current the erosion in the gas mixture is 1.5–2 times greater than in pure helium.

For $t_d > \tau_0$ fullerenes and soot particles are formed in the arc and settle on the walls of the vacuum chamber. After completion of the discharge the soot is collected from the chamber walls and the fullerene content in it is determined.[6] The fullerene content α in soot was about 5%, which is the

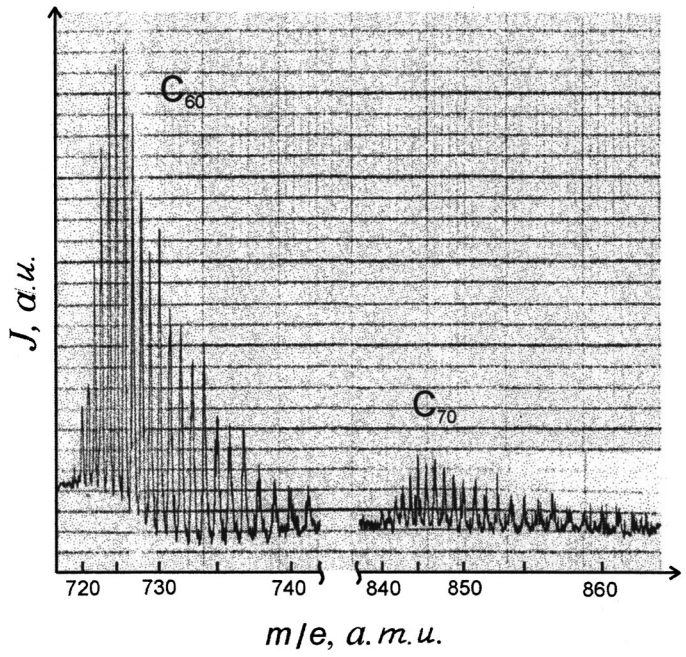

FIG. 1. Experimental mass spectrum of ^{13}C-enriched fullerenes: $p_{He}=70$ torr, $p_{CO_2}=33$ torr, $I=80$ A, and $t_d=270$ s.

same as the values of α obtained in discharges in the mixture He + O_2.[7]

The soot samples were analyzed in a mass-reflectron time-of-flight mass spectrometer.[8] Figure 1 shows the mass spectrum of fullerene soot for one of the experimental regimes. It is evident that substantial enrichment of the fullerenes C_{60} and C_{70} with the isotope ^{13}C has occurred. The distribution of ^{13}C over the mass spectrum for C_{60} and C_{70} is approximately the same. The experiments showed that the form of the mass spectrum depends on the current, the initial pressure p_{CO_2}, and the burning time of the discharge.

We shall consider a qualitative model of the processes occurring. If ^{13}C and ^{12}C atoms are present in the zone where fullerenes are formed, then the formation probability of the fullerene $^{13}C_n\,^{12}C_{60-n}$ is

$$W_n(t)=C_{60}^n p^n(1-p)^{60-n}, \tag{2}$$

where $C_{60}^n=(60!/n!(60-n)!)$ and $p(t)$ is the relative concentration of ^{13}C in carbon gas.

Therefore the form of the function $p(t)$ must be found. Since the energy required to rupture a C–O bond is much greater than the energy required to rupture a C–C bond, on leaving the hot zone of the arc, where all components are in an atomic state, at first CO molecules will form first, after which the carbon atoms which are not bound by oxygen start to form fullerenes and soot. The CO molecules formed, which are carried by the gas flow into the fullerene production zone soon or later once again enter the hot zone of the discharge. For this reason it is obvious that $p(t)$ will decrease with time only because of ^{13}C ''leaves'' with the fullerenes and soot particles. Hence

$$dp/dt=-p(t)/\tau \tag{3}$$

and

$$p(t)=p_0\exp\left(-\frac{t}{\tau}\right). \tag{4}$$

It is obvious that the time constant τ will depend on the total amount of the isotope ^{13}C in the vacuum chamber before the discharge is ignited and on the ''rate of substitution'' of the isotope ^{12}C for the ^{13}C in CO molecules, which will obviously be determined by the erosion of the anode. For this reason, τ can be related with the characteristic time τ_0 as

$$\tau=\alpha\tau_0, \tag{5}$$

where α is a variable parameter.

The constant p_0, equal to the ratio of the concentrations of ^{13}C carbon atoms entering the fullerene production zone to the total carbon concentration in this zone at the start of soot formation, is likewise a variable parameter of the problem.

It is obvious that the soot extracted from the chamber after completion of the discharge contains fullerenes which were produced at different times during the burning of the discharge. The total mass spectrum of fullerenes obtained in a discharge buring for a long time can be found by integrating the instantaneous mass spectrum

$$W_n=\int_0^t W_n(t)dt, \tag{6}$$

where $t=t_d-\tau_0$.

Varying the parameters α and p_0 in the calculation, the least-squares method can be used to fit the mass spectrum to the experimental spectrum. Figure 2 displays the results of such a fit for three regimes, differing by the initial pressure

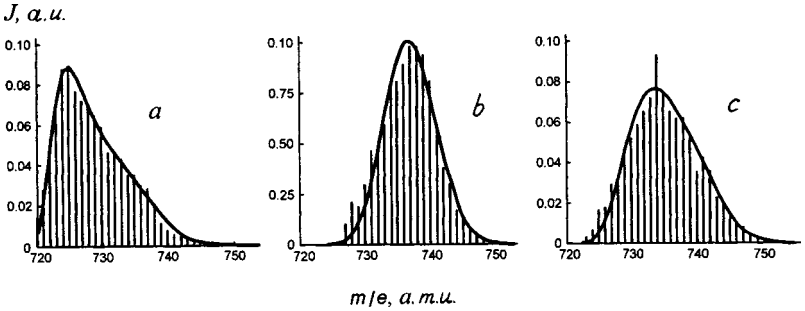

FIG. 2. Comparison of the experimental mass spectra with calculations.

TABLE I.

	Experiment						Calculation		
	p_{He}, torr	p_{CO_2}, torr	I, A	t_d, s	q, mg/s	τ_0, s	t, s	α	p_0
a	70	33	80	300	7	40	260	3.6	0.31
b	33	65	80	200	7	80	120	4.1	0.33
c	30	66	60	440	–	140	300	2.6	0.37

p_{CO_2}, the discharge burning time t_d, and the erosion of the anode. The solid curves in this figure show the computational results.

It is evident that the calculation conveys well the qualitative features of the experimental mass spectra. Considering the roughness of the proposed model, it can be asserted that the parameters α and p_0 remain approximately constant for all three regimes.

In summary, the experiments performed have shown that fullerenes can be enriched with the isotope ^{13}C as a constituent of gas molecules, and the proposed qualitative model correctly reflects the experimental laws.

This work was supported by the International Science and Technology Center (Projects Nos. 012 and 0.12b).

[1] J. R. Heath, *Fullerenes: Synthesis, Properties and Chemistry of Large Carbon Clusters*, edited by G. S. Hammond and V. J. Kuck (ACS Symposium Series 481, Washington, 1992), pp. 1–23.
[2] C. S. Jannoni, P. P. Bernier, D. S. Bethune, and G. Meier, J. Am. Chem. Soc. **113**, 390 (1991).
[3] A. P. Ramirez, A. R. Kortan, M. J. Rosseinsky, and S. J. Duclos, Phys. Rev. Lett. **68**, 1058 (1992).
[4] T. W. Ebbesen, J. Tabuchi, and K. Tanigaki, Chem. Phys. Lett. **191**, 336 (1992).
[5] A. V. Astakhov, G. A. Baranov, V. Ju. Baranov in *12th International Symposium on Gas Flow and Chemical Lasers and High-Power Laser Conference*, St. Petersburg, 31.08–5.09.1998, Proceedings of SPIE, pp. 408–414.
[6] D. Afanas'ev, I. Blinov, A. Bogdanov *et al.*, Zh. Tekh. Fiz. **64**(10), 76 (1994) [Tech. Phys. **39**, 1017 (1994)].
[7] D. V. Afanas'ev *et al.*, Zh. Tekh. Fiz. (1999) [Tech. Phys.], in press.
[8] V. I. Mamyrin and B. A. Mamyrin, Mol. Mater. **4**, 195 (1994).

Translated by M. E. Alferieff

Motion of a ''drift island'' in a toroidal magnetic confinement device with Coulomb scattering of the particles

A. A. Shishkin, Osamu Motojima, and É. I. Polunovskiĭ

Institute of Plasma Physics, National Science Center ''Khar'kov Physicotechnical Institute,'' Ukraine; National Science Institute for Fusion Science, Tokyo 509–5292, Japan; Khar'kov State University, Ukraine

(Submitted September 15, 1998)
Pis'ma Zh. Tekh. Fiz. **25**, 19–27 (September 26, 1999)

A resonant drift trajectory of a charged-particle in a magnetic field (a ''drift island'') can be used to remove high-energy impurities from a thermonuclear plasma and to introduce (inject) high-energy particles into the plasma. As a rule, these effects are studied neglecting the Coulomb scattering, i.e., in the collisionless approximation. In the present letter, the effect of Coulomb scattering of a particle with a resonant trajectory by plasma particles is studied. The conditions under which the drift resonance is maintained are found, i.e., the plasma densities and plasma density profiles for which the ''drift island'' can still move over the transverse section of the plasma are determined. © *1999 American Institute of Physics.* [S1063-7850(99)02009-1]

I. INTRODUCTION

The sets of tracks of the trajectories of a charged particle with different starting points in a confinement device with rotational transformation in a distinguished meridional section of the torus form a family of drift surfaces. Sections of these surfaces can be a closed curve such as a circle, ellipse, or a triangle with smoothed corners. If any drift surface possesses a rotation angle i^* which is a rational number n/m, i.e., $i^* = n/m$, and a perturbing magnetic field with ''wave numbers'' n and m is present in the magnetic confinement device, then a chain of islands forms at the location of the drift surface. There are m such islands in the meridional section and each island rotates n times over the length of the torus. If the condition $i^* = n/m$ can be made to move along the transverse section of the plasma by some method, then the particle moves in a transverse section of the plasma.[1,2] In Refs. 2 and 3 it was proposed that the main helical magnetic field in a toroidal confinement device be varied slowly and it was shown that in this manner high-energy impurities, for example, cooled α particles, can be removed from the plasma center or high-energy ions from the plasma periphery can be introduced into the plasma center, for example, tritium can be injected as fuel into a thermonuclear reactor. In so doing it is important that the time of variation of the helical field be matched with the time of formation of a drift island.[2,3] In this manner it is possible to use transit particles with a high value of the parameter $V_\parallel/V$, the so-called pitch-velocity parameter. It is obvious that Coulomb scattering of particles, which changes the parameter $V_\parallel/V$, can disrupt the drift resonance and interrupt the extraction or injection of high-energy ions. However, the plasma density and the density profile influence this entire process. What kind of plasma density profile is required so that drift resonance is preserved and can be used to influence the behavior of a particle? We shall consider how this occurs for the thermonuclear confinement device Large Helical Device (LHD),[4] which has been put into operation at the National Institute for Fusion Science in Tokyo, Japan. A superconducting helical coil with $l=2$, producing a magnetic field $B_0=4$ T, is used in this device. A special coil producing a perturbing magnetic field with $m=1$ and $n=1$ is installed in the system. A magnetic island, arising at the location of the magnetic surface with a rotational transformation angle of 1, should make it possible to divert hot plasma and to weaken the contact of the plasma with the wall. The duration of a plasma pulse in LHD should reach 1000 s. In such a system it makes sense to control the motion of distinguished particles by slowly varying the helical magnetic field.

II. BASIC EQUATIONS

1. For our study we assume that the particle motion can be described by the equations for a guiding center[5]

$$\frac{d\mathbf{r}}{dt} = V_\parallel \frac{\mathbf{B}}{B} + \frac{M_j c(2V_\parallel^2 + V_\perp^2)}{2eB^3}[\mathbf{B}\cdot\nabla B],$$

$$\frac{dW}{dt} = \frac{M_j V_\perp^2}{2B}\frac{\partial B}{\partial t},$$

$$\frac{d\mu}{dt} = 0. \tag{1}$$

Here W is the kinetic energy of a particle, $V_\parallel$ and $V_\perp$ are the parallel and perpendicular components of the particle velocity, M_j and e are the particle mass and charge, $\mathbf{B}$ is the magnetic field vector, μ is the transverse adiabatic invariant of the particle ($\mu=(M_j V_\perp^2)/2B$), and $\mathbf{r}$ is the radius vector of the guiding center of the particle.

2. The main magnetic field ($\mathbf{B}=\nabla\Phi$) is modeled with the scalar potential

$$\Phi = B_0\left[R\varphi - \frac{R}{m}\sum_n \varepsilon_{n,m}(r/a_h)^n \sin(n\vartheta - m\varphi) + \varepsilon_{1,0} r\sin\vartheta\right], \quad (2)$$

where B_0 is the magnetic field on the circular axis of the torus, R and a_h are the major and minor radii of the torus on whose surface the helical conductors lie; r, ϑ, and φ are the coordinates of the observation point which are related with the circular axis of the torus: r is the radial distance from the circular axis of the torus to the observation point and ϑ and φ are the angular variables along the major and minor circumferences of the torus, ϑ is measured from the direction opposite to the principal normal to the circular axis of the torus; the metric coefficients of the coordinates are: $h_r = 1$, $h_\vartheta = r$, $h_\varphi = R + r\cos\vartheta$; the summation index m in our case is the number m_h of periods of the magnetic field on the length of the torus, the summation index n in our case is the number l of poles of the helical coil, and $\varepsilon_{n,m}$ are the coefficients of the harmonics of the magnetic field.

The following parameters were chosen for our investigation: $l = 2$, $m_h = 10$, $R = 3.9$ m, $a_h = 0.975$ m, and $B_0 = 3$ T. We give the coefficients of the helical harmonics in the form

$$\varepsilon_{n,m} = \varepsilon_{n,m,0} + \varepsilon_{n,m,1}\sin(\Omega_{n,m}t + \delta_{n,m}), \quad (3)$$

where in our case $\varepsilon_{2,10,0} = 0.94$, $\varepsilon_{2,10,1} = 0.06$, $\varepsilon_{3,10} = -0.032$, $\varepsilon_{1,10} = -0.056$ (the satellites to the helical harmonics are assumed to remain unchanged in time), and all other coefficients $\varepsilon_{n,m}$ are assumed to be zero. The phase $\delta_{2,10} = -\pi/2$ and $\varepsilon_{1,0} = 0.045$, which corresponds to the presence of a transverse magnetic field equal to 4.5% of the main longitudinal field. A magnetic configuration with a displacement of the magnetic axis into the torus is obtained for this value of the transverse magnetic field. The magnetic-field frequency $\Omega_{2,10}$ is 5750 rad/s when dynamic control of the drift resonance is realized.

The perturbing magnetic field can be described with the potential

$$\Phi_p = B_0 a_h \frac{\varepsilon_{n,m,p}}{m}(r/a_h)^m \sin(m\vartheta - n\varphi + \delta_{n,m,p}). \quad (4)$$

In our case the ''wave'' numbers of the perturbing magnetic field are $m = 1$ and $n = 1$, and the amplitude of the perturbing magnetic field is $\varepsilon_{1,1,p} = 0.0003$ and $\delta_{n,m,p} = \pi/2$.

3. We take as a test particle a deuterium ion with energy $W = 350$ keV and initial value of the parameter $V_\parallel/V = 0.9$. The coordinates of the starting point of the ion are $r_0 = 20$ cm, $\vartheta_0 = 0$, and $\varphi_0 = 0$.

4. The test particle is scattered by particles of the main plasma, whose density profile is $N = N(0)[1 - \Psi/\Psi(a_{pl})]^k$. The parameters $N(0)$ and k are variable in our analysis. The function Ψ describes a section of the magnetic surface and has the form

$$\Psi = (r/a_h)^2 + 2(R/a_h)^2/m^2 \times \sum_n n\varepsilon_{n,m}(r/a_h)^n \cos(n\vartheta - m\varphi). \quad (5)$$

Here the summation extends over $n = l$, $l-1$, $l+1$; the function $\Psi(a_{pl})$ describes the section of the magnetic surface coinciding with the plasma boundary; a_{pl} is the plasma radius, and in our case $a_{pl} = 43$ cm. In the presence of Coulomb scattering, the momentum $\mathbf{p}$ of the test particle varies according to the rule[6]

$$\frac{d\mathbf{p}}{dt} = -\frac{4\pi e^2}{V^3}\mathbf{V}\sum_* \frac{L(e^*)^2(M + m^*)}{Mm^*} N\Phi_1(b^*V), \quad (6)$$

where $\Phi_1(x) = \Phi(x) - x(d\Phi/dx)$, and $\Phi(x)$ is the error function. The parameter $b^* = \sqrt{m^*/2T^*}$; L is the Coulomb logarithm; e^*, m^*, and T^* are the charge, mass, and temperature of the plasma particles; the temperature is assumed to be given by $T^* = T^*(0)[1 - \Psi/\Psi(a_{pl})]$. The summation in Eq. (6) extends over the index * denoting the type of particle. Results are presented below for the case of a test particle scattered by the plasma electrons. The plasma temperature at the center is taken to be $T(0) = 10$ keV. The variation of $V_\parallel$ and $V_\perp$ in time according to Eq. (6) is taken into account at each step of the integration in the numerical solution of the system of equations (1).

III. DRIFT RESONANCE WITH COULOMB SCATTERING

In the collisionless approximation deuterium ions with energy $W = 350$ keV and $V_\parallel/V = 0.9$ can be introduced from the plasma periphery into the center of the magnetic confinement device with helical magnetic fields, using the resonance $i^* = 1/1$.[2] A drift island can arise at the location of the drift surface with rotation angle $i^* = 1$ under the action of a magnetic perturbation with the ''wave numbers'' $n = 1$ and $m = 1$. For $\varepsilon_{2,10} = 0.88$ a drift island is formed by the particle trajectory with the initial coordinates $r_0 = 20$ cm, $\vartheta_0 = 0$, and $\varphi_0 = 0$ (Fig. 1a); for $\varepsilon_{2,10} = 1.0$ a drift island is formed by a particle trajectory with the initial coordinates $r_0 = 7$ cm, $\vartheta_0 = 0$, and $\varphi_0 = 0$ (Fig. 1a). As $\varepsilon_{2,10}$ varies in time from 0.88 to 1.0 in accordance with the relation (3), the drift island moves from the periphery into the center of the plasma (Fig. 1b). The motion is followed for $\tau = 4.9\times10^{-4}$ s. In the figure the tracks left by the trajectory in the section single out are connected by a line for clarity, making it possible to follow the sequence of tracks. The main physical conclusion is that a deuterium ion enters the center of the magnetic confinement volume.

When the Coulomb scattering is taken into account for plasma with $N(0) = 5\times10^3$ cm^{-3} and $k = 3$ and $k = 4$ the drift island moves (''drifts'') from the pperiphery into the center of the plasma in essentially the same manner as in the case shown in Fig. 1b. For a profile which is not so sharp, specifically, $k = 2$ and $N(0) = 5\times10^{13}$ cm^{-3}, there is no drift island, i.e., resonance breaks down. Decreasing $N(0)$ partially restores the drift resonance. Thus, for $N(0) = 1\times10^{13}$ cm^{-3} the drift angle of rotation becomes closer to 1: $i^* = 1.069$. A particle starting at a point with the initial coordinates $r_0 = 20$ cm, $\vartheta_0 = 0$, and $\varphi_0 = 0$ moves in a manner so that the resonance $i^* = 1$ is satisfied at the start of the path — the outlines of a moving drift island can be seen (Fig. 2a), but then the ''island structure'' is replaced by the tracks of a trajectory which are characteristic for an ordinary transit par-

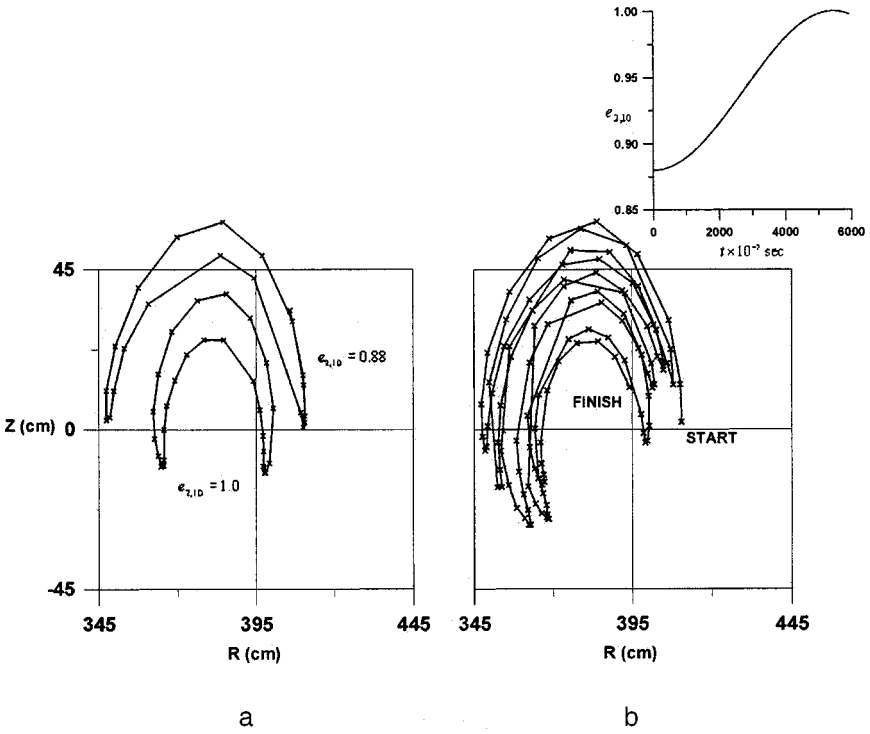

FIG. 1. Drift island formed by a transit deuterium ion with a starting point with coordinates $r_0=20$ cm, $\vartheta_0=0$, and $\varphi_0=0$ with $\varepsilon_{2,10}=0.88$ and $r_0=7$ cm, $\vartheta_0=0$, $\varphi_0=0$ with $\varepsilon_{2,10}=1.0$ (a); motion of a drift island with $\varepsilon_{2,10}$ varying in time (b). Plasma density $N(0)=0$.

ticle, i.e., resonance is disrupted. For $N(0)=0.1\times10^{13}$ cm^{-3} and $k=2$ the drift resonance is completely restored.

However, the decrease in the density at plasma center cannot be regarded as an acceptable solution to the problem, while an attempt can be made to control the plasma profile by choosing, for example, the method of heating. For a sharp density profile, i.e., $k=3$ and $N(0)=1\times10^{13}$ cm^{-3}, a ''drift resonance'' occurs (Fig. 2b). The drift island moves freely even for high density $N(0)=10\times10^{13}$ cm^{-3} (Fig. 2c). The deuterium ion reaches the plasma center.

IV. DISCUSSION

An important step in the assessment of the effect of dissipative mechanisms on the satisfaction of the conditions for

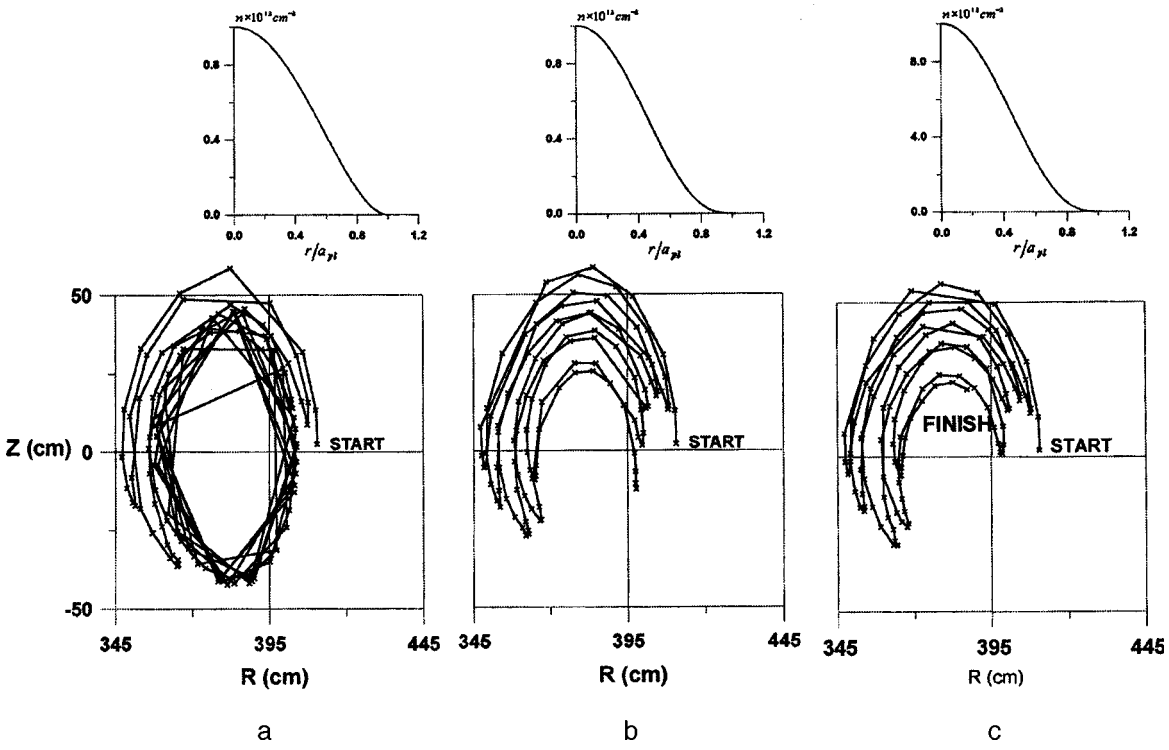

FIG. 2. Disruption of a drift resonance for $N(0)=1\times10^{13}$ cm^{-3}, $k=2$ (a) and restoration of the drift resonance for $N(0)=1\times10^{13}$ cm^{-3}, $k=3$ (b), motion of a drift island for $N(0)=10\times10^{13}$ cm^{-3}, $k=3$ (c).

a drift resonance of a particle was taken using a combined approach employing the equations for a guiding center to describe the motion of a test particle and the Coulomb scattering of the test particle by the plasma particles. The drift resonance is sensitive to the value of the density and the density profile of the plasma. The closer the plasma profile to ''bell shaped,'' the weaker the effect of Coulomb scattering on the ''motion of a drift island'' is. The present investigation took account of the change in the momentum of a test particle. Preliminary results show that the change in the kinetic energy of a test particle in Coulomb scattering does not fundamentally change the physical picture.

V. CONCLUSIONS

The following conclusions can be drawn fromour investigation of the effect of Coulomb scattering of particles on the dynamics of a drift resonance (the motion of a ''drift island'') in a slowly varying helical magnetic field.

1. For a plasma density profile $N=N(0)[1-\Psi/\Psi(a_{pl})]^k$, $N(0)=1\times10^{13}$ cm^{-3}, and $k=2$, a drift resonance with $i^*=1/1$ is disrupted, and a resonant particle transforms into a transit particle with a nonresonant angle of rotation.

2. For a sharper density profile, specifically, for $k=3$, the drift angle of rotation retains its resonant value and the particle forms a ''drift island'' under the action of a perturbing magnetic field with the ''wave numbers'' $m=1$ and $n=1$. A profile with $k=3$ ensures that the conditions for drift resonance are satisfied for $N(0)=10\times10^{13}\,\mathrm{cm}^{-3}$ and right up to $N(0)=100\times10^{13}$ cm^{-3}.

3. A drift island in a slowly varying helical magnetic field (and with Coulomb scattering of a test particle by the plasma particles) moves in the transverse section of the plasma. Ions with high energy and high longitudinal velocity can reach the plasma center. This mechanism can be used to introduce fuel into a thermonuclear reactor and to introduce high-energy ions in order to change the electric field profile in the plasma.

[1] H. E. Mynick and N. Pomphrey, Nucl. Fusion **34**, 1277 (1994).
[2] O. Motojima and A. A. Shishkin, Plasma Physics and Controlled Fusion (in press).
[3] A. A. Shishkin and O. Motojima, and É. I. Polunovskiĭ, Pis'ma Zh. Tekh. Fiz. (1999) [Tech. Phys. Lett.], in press.
[4] O. Motojima *et al.*, Plasma Phys. Controlled Fusion **38**, A77 (1996).
[5] A. I. Morozov and L. S. Solov'ev, *Reviews in Plasma Physics*, edited by Academician M. L. Leontovich (Consultants Bureau, New York, 1966), Vol. 2, pp. 201–297.
[6] D. V. Sivukhin D. V., *Reviews in Plasma Physics*,, edited by Academcian M. L. Leontovich (Consultants Bureau, New York, 1966), Vol. 4, pp. 93–241.

Translated by M. E. Alferieff

Interaction of hydrogen with a metal–oxide–semiconductor structure containing an additional solid-electrolyte layer

V. Filippov, A. Vasil'ev, A. Terent'ev, and V. Morits

Russian Science Center ''Kurchatov Institute,'' Moscow; Humboldt University, Berlin, Germany
(Submitted April 23, 1999)
Pis'ma Zh. Tekh. Fiz. **25**, 28–32 (September 26, 1999)

The effect of hydrogen on the flat-band voltage of the structure $Pt/LaF_3/SiO_2/SiC$, which is the sensitive element of a high-temperature fluorochlorocarbons sensor, is investigated. It is shown that at 441 K temperature and 10^{-2}% hydrogen concentration in air, the capacitance–voltage characteristic of the structure shifts in the direction of negative voltages by about 160 mV. Increasing the temperature decreases this amount, apparently because of the catalytic oxidation of oxygen on the platinum electrode of the structure. The hydrogen sensitivity of the structure investigated can affect the kinetics of the response of a sensor interacting with hydrogen-containing fluorochlorocarbons. [S1063-7850(99)02109-6]

Increasing the operating temperature of sensors with sensitive elements based on a metal–insulator–semiconductor structure extends the range of detectable gases. As a result of the dissociation of complex molecules, products that influence the electrophysical properties of the structure are produced on the catalytically active electrode. Replacing silicon in the hydrogen-sensitive structure catalytically active metal–silicon dioxide–silicon[1] by wide-gap silicon carbide makes it possible to raise the operating temperature of a $Pt/SiO_2/SiC$ sensor to 1000 K and to detect methane and other saturated hydrocarbons reliably.[2] A structure with an additional subgate layer of the solid electrolyte $Pt/LaF_3/SiO_2/SiC$ exhibits high sensitivity to fluorine even at room temperature,[3] and at temperatures above 600 K it is sensitive to fluorochlorocarbons (freons).[4] However, as a result of high-temperature catalytic dissociation of complex molecules, such as Freon 134 (CF_3CH_2F), Freon 22 ($CHClF_2$), and so on, hydrogen in one form or another can form on the gas–metal–solid three-phase electrolyte boundary. Our objective in the present work is to investigate the sensitivity of the structure $Pt/LaF_3/SiO_2/SiC$ to hydrogen.

Structures of the type described in detail in Ref. 5 were used as experimental samples. A solid layer of the electrolyte LaF_3 (240 nm thick) was deposited by thermal deposition on a semiconductor silicon carbide substrate with an epitaxial 6H–SiC layer (n type, carrier density $10^{15}-10^{16}$ cm^{-3}, thickness 5 μm) and a layer of the oxide SiO_2 (35 nm thick). A high-temperature ohmic contact consisting of annealed nickel was formed on the substrate. A catalytically active platinum electrode (0.7 mm in diameter, 30 nm thick) was deposited on the solid-electrolyte layer by magnetron sputtering. A sensor, located on top of the heater, was placed into the measuring gas cell. The cell was connected to a dynamic-mixing gas stand, which made it possible to deliver to the cell ''steps'' of hydrogen concentration in synthetic air ranging from 10^{-3} to 10^{-1}%.

Hydrogen-induced change in the flat-band voltage U of the structure was detected. The relaxation curves $U=f(t)$ with ''steps'' of hydrogen concentration in air introduced into the measuring cell were obtained for the temperatures of the structure 298, 441, and 603 K.

No reversible changes in U with cylced action of hydrogen in synthetic air was observed at room temperature. When the operating temperature of the structure is increased, a reversible change appears in the flat-band voltage on the structure. The signal obtained at 441 K temperature is shown in Fig. 1. A characteristic, for metal–insulator–semiconductor structure with catalytically active electrodes, response to the action of hydrogen — a shift of the capacitance–voltage characteristic in the direction of negative voltages — is observed. We note that the response of a structure with an additional subgate layer of the solid electrolyte LaF_3 on interaction with fluorine has the opposite sign — the capacitance–voltage characteristic shifts in the direction of positive voltages.

The quantity ΔU, equal to the difference of the stationary values of U in air and in an air–hydrogen medium can serve as the sensor signal that is correlated with the hydrogen concentration. Figure 2 shows ΔU versus the hydrogen concentration in synthetic air for the two temperatures 441 and 603 K. The decrease in the sensor response with increasing temperature is probably due to heterogeneous oxidation of hydrogen on the platinum electrode.[6] If a simple oxidation–reduction reaction occurs on the hydrogen–platinum–solid electrolyte three-phase boundary, then ΔU is related with the hydrogen concentration P_{H_2} by the Nernst equation

$$\Delta U=(kT/Ze)\cdot \ln P_{H_2},$$

where k is Boltzmann's constant, Z is the number of electrons participating in the reaction, and e is the electron charge. Fitting a relation of this type to the experimental points (solid lines in Fig. 2) gives $Z=1.6\pm 0.2$ for both temperatures. This is close to the value $Z=2$, which corresponds to simple dissociative absorption of hydrogen at the interface

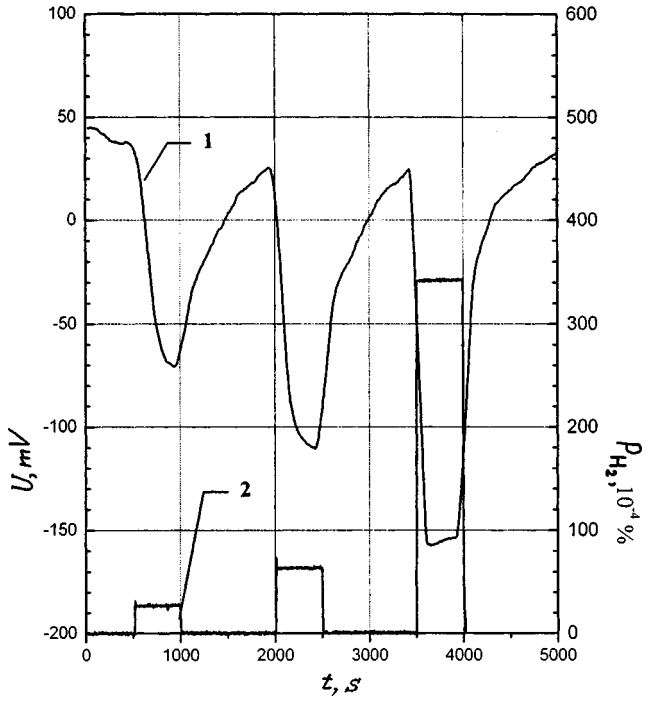

FIG. 1. Relaxation curve (*1*) showing the variation of the flat-band voltage of the structure as ''steps'' of oxygen concentration in air (*2*) are introduced into the measuring cell. The operating temperature of the structure is 441 K.

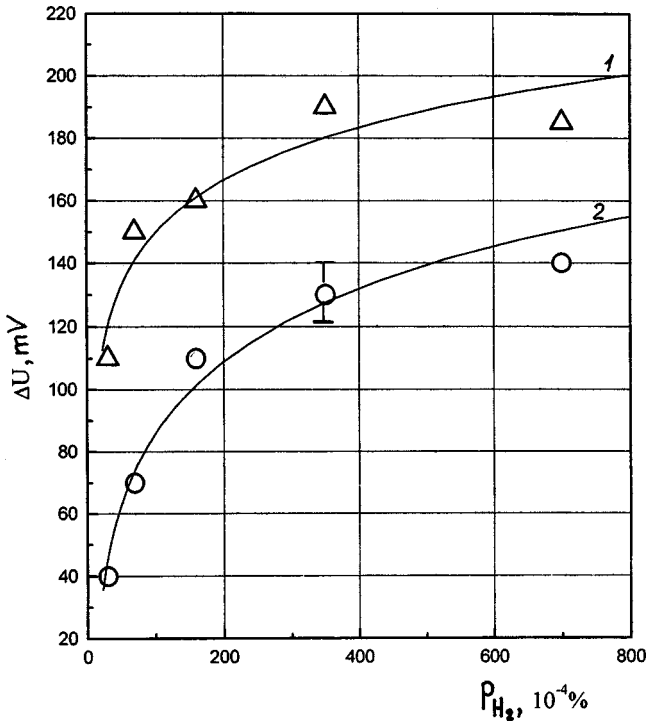

FIG. 2. Stationary change ΔU of the flat-band voltage of the structure $Pt/LaF_3/SiO_2/SiC$ versus the hydrogen concentration P_{H_2}. Dots — experimental data (*1* — temperature of the structure 441 K, *2* — temperature of the structure 603 K), solid lines — fit of the Nernst equation with $Z=1.6$.

followed by the formation of a charged double layer. This process can be described by the reaction $H_2 \rightarrow 2H - 2e \rightarrow 2H^+$. However, the experimental points in the entire concentration range are poorly described by the Nernst equation. The concentration dependence tends to saturate at hydrogen concentrations in air above 3×10^{-2}%. Additional study is required to determine the mechanism of the interaction of hydrogen with the $Pt/LaF_3/SiO_2/SiC$ structure and the influence of oxygen on this process. The results obtained in this work show that the interaction of hydrogen with a structure with a subgate layer of the solid electrolyte LaF_3 changes its flat band voltage. Therefore the hydrogen formed (on the Pt/LaF_3 interface) as a result of the high-temperature dissociation of freons can introduce characteristic features into the kinetics of the sensor response.

This work was supported by the Volkswagen Foundation, grant No. 1/70–753.

[1] I. Lundström, M. S. Shivaraman, and C. M. Svemson, J. Appl. Phys. **46**, 3876 (1975).
[2] A. Arbab, A. Spetz, and I. Lundström, Sens. Actuators B **15–16**, 19 (1993).
[3] W. Moritz, S. Krause, A. Vasiliev *et al.*, Sens. Actuators B **24–25**, 194 (1995).
[4] W. Moritz, V. Filippov, A. Vasiliev *et al.*, J. Fluorine Chem. **93**, 61 (1999).
[5] W. Moritz, V. Filippov, L. Bartolomäus *et al.*, in *Proceeding of 11th European Conference on Solid State Transducers*, Warsaw, Poland, 21–24 September 1997, pp. 111–114.
[6] V. Grabchak, A. Terent'ev, V. Filippov *et al.*, Zh. Anal. Khim. **48**, 450 (1993).

Translated by M. E. Alferieff

Fast magnetosonic and fast Alfvén waves in an elliptic plasma cylinder

D. L. Grekov, V. I. Lapshin, and M. M. Yakovlev

Institute of Plasma Physics, National Science Center ''Khar'kov Physicotechnical Institute,'' Ukraine
(Submitted December 15, 1998)
Pis'ma Zh. Tekh. Fiz. **25**, 33–38 (September 26, 1999)

The propagation of ion–cyclotron waves in an extended cylindrical plasma is analyzed analytically. The results obtained show progress in constructing a two-dimensionally–nonuniform analytical theory. © *1999 American Institute of Physics.* [S1063-7850(99)02209-0]

Together with numerical methods, the plasma-cylinder model is one of the most popular models for planning and analyzing the results of experiments on rf heating of plasma in the ion-cyclotron frequency range. In many setups the plasma filament has an elliptic cross section, so that it is of interest to investigate the effect of the shape of the filament on the distribution of rf fields in the plasma. This problem was first studied in Ref. 1, where the deviation of the shape of the filament from a circle was assumed to be small.

The present letter is devoted to an analytic investigation of the propagation of fast magnetosonic (FMSWs) and fast Alfvén (FAWs) waves in an elliptic plasma cylinder in an axial magnetic field $B_0 \| Oz$. The characteristic oscillations of such a cylinder are investigated as a first step. We employ elliptic coordinates (ξ,φ,z). They consist of a system of confocal ellipses $\xi=\xi_i$ (ξ is the analog of the radial coordinate) and hyperbolas $\varphi=\varphi_i$ (φ is the analog of the azimuthal coordinate). The focal distances of all ellipses are $2h=2a\varepsilon=2a/\cosh\xi$, and $\varepsilon=\sqrt{1-b^2/a^2}$. Here a is the major axis and b is the minor axis of the ellipse, ε is the eccentricity, $\varepsilon\to 0$ ($\xi\to\infty$) corresponds to a circle, and $\varepsilon\to 1$ ($\xi\to 0$) corresponds to a slit. We note that even a small deviation from a circle ($a=100$ cm, $b=99$ cm) leads to $\varepsilon=0.14$, and for the JET setup $\varepsilon=0.7$.

We assume the plasma to consist of two types of ions and electrons and $E_z=0$. We write the rf field in the form $\mathbf{B}\sim\mathbf{B}(\xi,\varphi)e^{i\mathbf{k}\| z}$. Then we have for B_z

$$\frac{\partial}{\partial\xi}\left(\frac{1}{N_\perp^2}\frac{\partial B_z}{\partial\xi}\right)-i\frac{\partial}{\partial\xi}\left[\frac{\varepsilon_2}{N_\perp^2(\varepsilon_1-N_\|^2)}\right]\frac{\partial B_z}{\partial\varphi}$$

$$+\frac{1}{N_\perp^2}\frac{\partial^2 B_z}{\partial\varphi^2}+\frac{\omega^2h^2}{c^2}(\cosh^2\xi-\cos^2\varphi)B_z=0, \qquad (1)$$

where

$$N_\perp^2=N_\perp^2(\xi)=\frac{(\varepsilon_1-N_\|^2)^2-\varepsilon_2^2}{(\varepsilon_1-N_\|^2)},$$

$$\varepsilon_1=1-\frac{\omega_{p1}^2}{\omega^2-\omega_{c1}^2}-\frac{\omega_{p2}^2}{\omega^2-\omega_{c2}^2}+\frac{\omega_{pe}^2}{\omega_{ce}^2},$$

$$\varepsilon_2=-\frac{\omega}{\omega_{c1}}\frac{\omega_{p1}^2}{\omega^2-\omega_{c1}^2}-\frac{\omega}{\omega_{c2}}\frac{\omega_{p2}^2}{\omega^2-\omega_{c2}^2},$$

ω_{p1}, ω_{p2}, and ω_{pe} are the ion and electron plasma frequencies, and ω_{c1}, ω_{c2}, and ω_{ce} are the ion and electron cyclotron frequencies.

For a uniform plasma Eq. (1) admits separation of variables $B_z(\xi,\varphi)=\mathbf{u}(\xi)\cdot\nu(\varphi)$. Then the field in the plasma can be described by the Mathieu equations

$$\frac{\partial^2\mathbf{u}}{\partial\xi^2}-(C-2q\cdot\cosh 2\xi)\cdot\mathbf{u}=0,$$

$$\frac{\partial^2\nu}{\partial\varphi^2}+(C-2q\cdot\cos 2\varphi)\cdot\nu=0, \qquad (2)$$

where $q=(N_\perp\omega h)/2C)^2=(h/2\lambda_\perp)^2$ is the main parameter of the problem. Let us assume that the plasma is surrounded by a metal wall with $\xi=\xi_0$. Then the boundary condition has the form

$$-i\varepsilon_2\left.\frac{\partial B_z}{\partial\varphi}\right|_{\xi=\xi_0}+(\varepsilon_1-N_\|^2)\left.\frac{\partial B_z}{\partial\xi}\right|_{\xi=\xi_0}=0. \qquad (3)$$

We write the solution of Eqs. (2) in the form

$$B_z(\xi,\varphi)=\sum_{m=0}^{\infty}C_m\,\mathrm{Ce_m}(\xi,q)\,\mathrm{ce_m}(\varphi,q)$$

$$+\sum_{m=0}^{\infty}S_m\,\mathrm{Se_m}(\xi,q)\,\mathrm{se_m}(\varphi,q). \qquad (4)$$

Here $\mathrm{ce_m}$ and $\mathrm{se_m}$ are the ordinary and $\mathrm{Ce_m}$ and $\mathrm{Se_m}$ the modified Mathieu functions.[2] For small $q/4$ one azimuthal harmonic can be retained in the expression (4) (the neighbor-

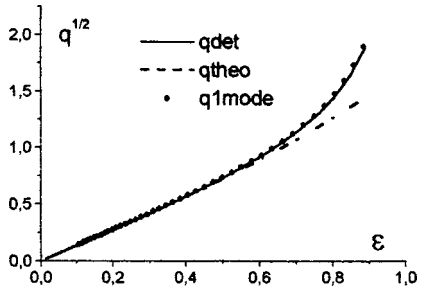

FIG. 1.

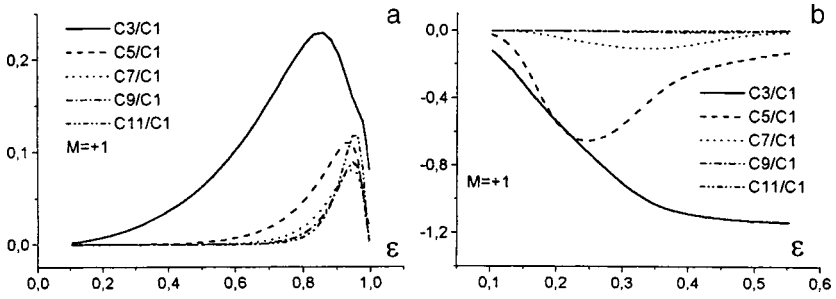

FIG. 2.

ing harmonics are proportional to $q/4$). Then, using Eq. (3), we obtain a dispersion equation for the characteristic oscillations of the elliptic cylinder

$$\frac{\varepsilon_2^2 \cdot m^2}{(\varepsilon_1 - N_\parallel^2)^2} \frac{\mathrm{Ce_m}(\xi_0, q_i)}{\mathrm{Ce'_m}(\xi_0, q_i)} = \frac{\mathrm{Se'_m}(\xi_0, q_i)}{\mathrm{Se_m}(\xi_0, q_i)}, \tag{5}$$

which determines the eigenvalues q_i. Taking the three leading terms in the expansions of $\mathrm{Ce_m}$ and $\mathrm{Se_m}$ in Bessel functions, we obtain from Eq. (5)

$$\sqrt{q_l} = \frac{(k_{\perp l} r)_{\mathrm{cir}}}{2} \varepsilon (1 + \varepsilon^2/4),$$

$$(k_{\perp l} a)_{\mathrm{el}} = (k_{\perp l} r)_{\mathrm{cir}} (1 + \varepsilon^2/4), \tag{6}$$

where $(k_{\perp l} r)_{\mathrm{cir}}$ is the solution of Eq. (5) for a ''circular'' cylinder, whose radius is equal to the major axis of the ellipse. From the solution (6) (Fig. 1, the curve ''qtheo'') follows that a change in the shape of the plasma filament with the cross-sectional area remaining constant does not affect $k_{\perp l}$ (or the eigenfrequencies $\omega_l^{(0)}$). The exact solution obtained numerically for the dispersion equation (5) is shown in Fig. 1 (curve ''q 1 mode''). Analyzing a solution in the form (4) with the boundary condition (3), we arrive at the conclusion that for $q \geqslant 1$ it consists of a set of coupled elliptic harmonics. The dispersion equation in this case can be obtained by setting to zero the determinant originating from Eq. (3) (Fig. 1, curve ''qdet''). Comparing the curves ''q 1 mode'' and ''qdet,'' we see that Eq. (5) gives the correct values of $k_{\perp l}$ even outside its range of applicability (for $q/4 \geqslant 1$).

We shall now study the azimuthal structure of the solutions obtained. Formally, it is completely different from the azimuthal waves existing in a ''circular'' cylinder. From Eq. (4) we obtain

$$S_m = i \frac{\varepsilon_2}{\varepsilon_1 - N_\parallel^2} \cdot m \cdot C_m \frac{A_m^m}{B_m^m} \frac{\mathrm{Ce_m}(\xi, q)}{\mathrm{Se'_m}(\xi, q)},$$

while for traveling waves

$$S_m = \pm i \cdot C_m \frac{A_m^m}{B_m^m} \frac{\mathrm{Ce_m}(\xi, q)}{\mathrm{Se_m}(\xi, q)},$$

where A_m^m and B_m^m are the coefficients in the Fourier expansions of $\mathrm{ce_m}$ and $\mathrm{se_m}$ in terms of $\cos l\varphi$ and $\sin l\varphi$, respectively. Figure 2 shows the eccentricity dependence of the amplitudes of the satellites with respect to the fundamental ($m = +1$) azimuthal harmonics normalized to the amplitude of the fundamental harmonic (a — first radial mode, b — seventh radial mode). The azimuthal dependence of the wave field is shown in Fig. 3 (a — first radial mode; b,c — seventh radial mode; $j\Sigma$ — sum of the harmonics). For comparison, a plot of $\cos\varphi$ corresponding to a ''circular'' cylinder is presented. For the first radial mode no substantial change in the azimuthal behavior of the oscillations is observed. However, for the seventh radial mode the azimuthal structure of the oscillations changes radically. The maxima of the field shift to the minor axis of the ellipse. The sinusoidal components of the field will also demonstrate a similar shift toward the minor axis.

We shall write out the corrections to the frequencies of the characteristic oscillations of the plasma cylinder which

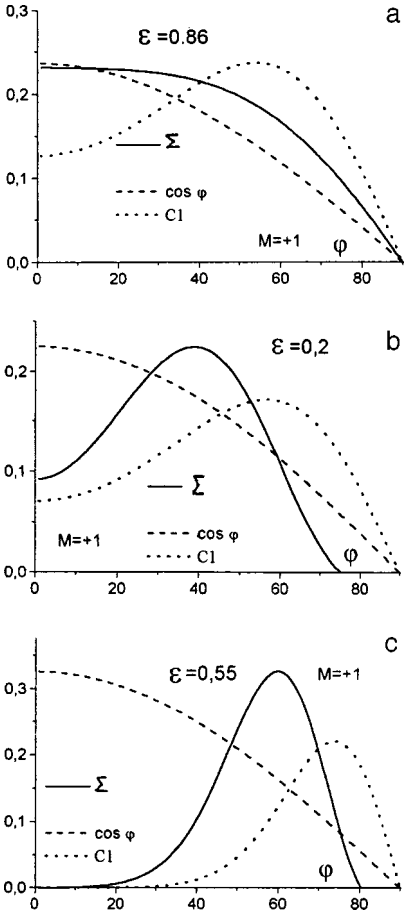

FIG. 3.

are due to the ellipticity. In the frequency range $\omega \approx \omega_{ci}$, $\omega < \omega_{ci}$ for $N_\parallel^2 \gg N_A^2$ FAWs with

$$\omega_{\mathrm{el}} = \omega^{(0)}\left(1 + \frac{k_\perp^2/k_\parallel^2}{1+k_\perp^2/k_\parallel^2}\,\frac{\varepsilon^2}{4}\right),$$

$$\omega^{(0)} = \omega_{ci}\left(1 - \frac{\omega_{ci}^2}{k_\parallel^2 \nu_A^2}\,\frac{k_\parallel^2 + k_\perp^2/2}{k_\parallel^2 + k_\perp^2}\right) \tag{7}$$

are excited. For FMSWs ($N_A^2 = c^2/\nu_A^2 \gg N_\parallel^2$, ν_A is the Alfvén velocity, $\omega^{(0)} = k\nu_A$) we have

$$\omega = \omega^{(0)}(1 + \varepsilon^2/4). \tag{8}$$

The results (7) and (8) are of the same order of magnitude as the results obtained in Ref. 1.

Thus, without assuming the deviation of the ellipse from a circle to be small, a dispersion equation for the characteristic oscillations of an elliptic plasma cylinder was derived and the eigenfrequencies and eigenvectors were found. It was shown that ellipticity substantially changes the azimuthal structure of the fields.

[1] I. A. Girka and K. N. Stepanov, Ukr. Fiz. Zh. **36**(7), 1051 (1991).
[2] *Handbook of Mathematical Functions*, edited by M. Abramowitz and I. Stegun (Dover, New York, 1965; Nauka, Moscow, 1979).

Translated by M. E. Alferieff

Structure of a picosecond electron beam inside a vacuum diode

K. A. Zheltov and I. G. Turundaevskaya

Scientific-Research Institute of Pulsed Technology, Moscow, Russia
(Submitted March 25, 1999)
Pis'ma Zh. Tekh. Fiz. **25**, 39–45 (September 26, 1999)

The structure of a picosecond ($\sim$150 ps) electron beam in the cathode–anode gap of a vacuum diode is determined. The electron beam is modeled in the form of flat quasiparticles with a definite charge density which follow one after another in equal time intervals. It is shown that the expansion of concentric layers of the beam under the action of the electric and magnetic self-fields strongly depends on the current strength. The experimental confirmation of the computed estimates is illustrated by recording the structure of the electron beam at the anode using a film which is sensitive to electron radiation. © *1999 American Institute of Physics.* [S1063-7850(99)02309-5]

In high direct current electron accelerators, in which a picosecond ($\sim 10^{-10}$ s) high-voltage burst is obtained by discharging a short ($\sim$1 cm) accumulator on a long line through a strongly overvoltaged ($\sim$700 kV/mm) spark gap,[1] propagating along the line to the vacuum diode, the incident voltage U can be described by the relation

$$U = U_m \cdot \sin^2(\pi t/2T), \quad 0 \leqslant t \leqslant 2T, \tag{1}$$

where U_m is the amplitude of the incident picosecond pulse and T is the duration at half-amplitude.

In the picosecond accelerators developed thus far, the amplitude of the incident pulse, as a rule, lies in the range 350–700 kV and the average duration is $\sim$150 ps with the electron-beam current varying from hundreds of amperes to several kiloamperes. If the electron beam must be extracted through the ''transparent'' anode, high-impedance vacuum diodes, in which the ''internal resistance'' is much greater than the wave impedance of a long line ($Z_l \ll Z_{wl}$), are ordinarily used. The maximum possible cathode–anode distances ($\sim$9 mm) and relatively small cathode areas are characteristic for such diodes. A high impedance makes possible the formation on the cathode–anode gap of a reflected pulse with the same polarity, as a result of which the accelerating voltage is essentially twice the incident amplitude. In many cases the energy of the electron beam can be much greater than 1 MeV.

The structure of an electron beam in a vacuum diode[2–4] is determined by the electric (Coulomb) and magnetic (Lorentz force) fields. A picosecond burst of current of a beam of

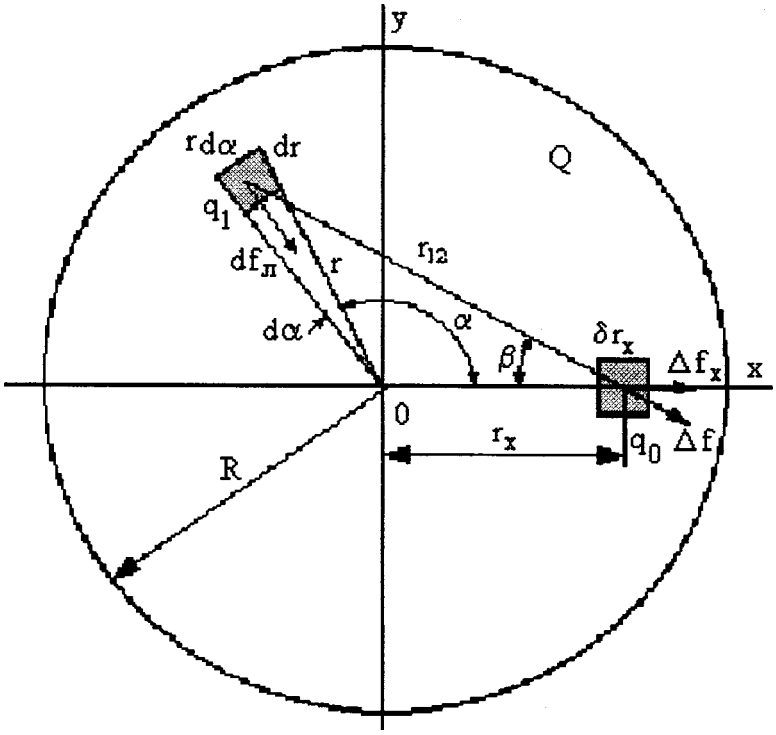

FIG. 1. Transverse section of an electron beam on the cathode surface — quasiparticle initially: R — cathode radius, r_x — initial radius of a beam layer.

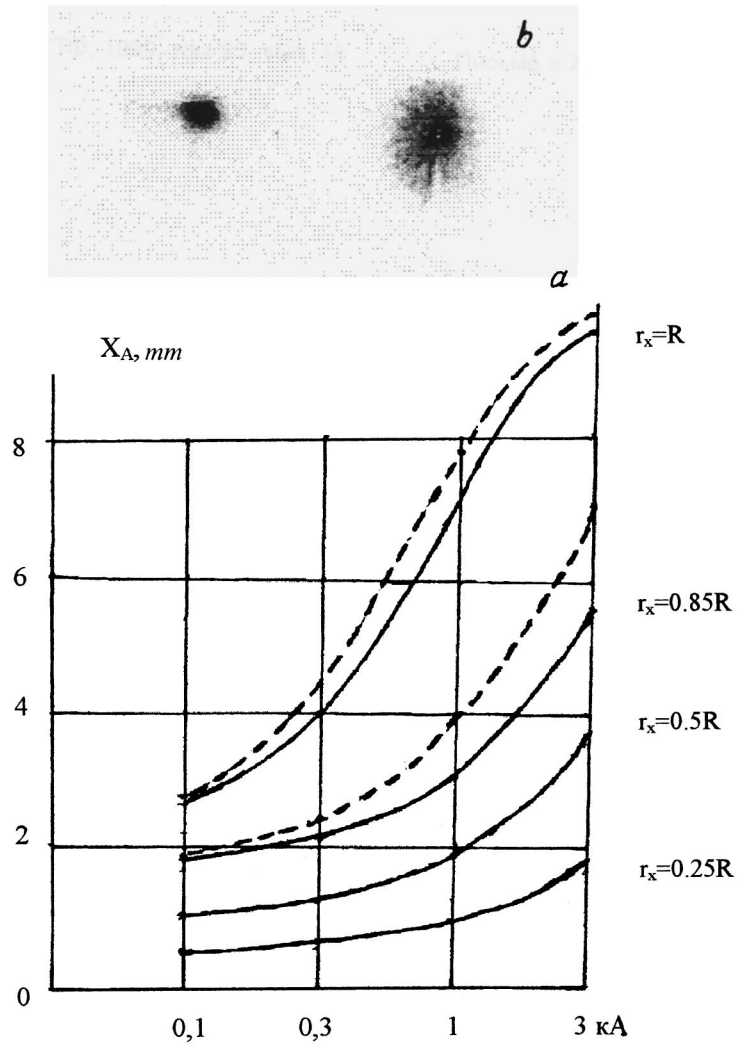

FIG. 2. a — Radius X_A of a beam layer on the anode versus the maximum current inside a vacuum diode for various layers (r_x). b — Structure of the electron beam at the anode with currents ~0.3 and ~2 kA (picosecond pulse duration $T \sim 150$ ps).

fast electrons, which is proportional to the difference of the incident and reflected voltage pulses, for large reflection coefficients β is described by approximately the same relation as Eq. (1) with the current amplitude $I_m = U_m(1-\beta)$. In numerical simulation, the time dependence of the beam current is divided into several intervals (~ 15) in which the volume charge density is approximately constant. The electrons in each interval are combined into a single quasiparticle with the total electric charge in this interval. The electron beam is therefore represented in the form of quasiparticles following one another with the same intervals but with a different charge density distribution.

The electrostatic repulsion of the distributed charge Q of a quasiparticle (Fig. 1) is due to the total effect of the Coulomb forces Δf on a charge element q_0 from all charge elements q_1

$$\Delta f = q_0 \cdot q_1 / 4 \cdot \pi \cdot \varepsilon_0 \cdot r_{12}^2, \tag{2}$$

where $q_1 = \rho_v r d\alpha dr$, $q_0 = (\delta r_x)^2 \rho_v$, $\varepsilon_0 = 8.85 \times 10^{-12}$ F/m, and ρ_v is the charge density of the distributed electrons.

The total force $\Sigma \Delta f$ acting on all elements q_1 in the relativistic case with $\Delta f \parallel v$ (Ref. 5) is proportional to the mass m_q of the charge q_0 and the acceleration dv/dt, where v is the instantaneous velocity,

$$\sum \Delta f = m_q (1 - v^2/c^2)^{-3/4} dv/dt. \tag{3}$$

Here $m_q = (\delta r_x)^2 m_v$, $m_v = \rho_v (m_e/e)$ is the mass density of the distributed charge ($m_e = 9.1 \times 10^{-31}$ kg and $e = 1.6 \times 10^{-19}$ C are the electron mass and charge).

For a quasiparticle corresponding to the current amplitude in the beam I_m with interval $\Delta\tau$ ($\sim 10^{-11}$ s), the distributed charge density is $\rho_v = I_m \Delta\tau / \pi R^2$, where R is the radius of the cathode of the vacuum diode, and for $\Delta\tau \approx R/c$ the quasiparticles do not affect one another. After appropriate transformations of the expressions (3), taking account of Eq. (2), we obtain a system of equations for the electrostatic expansion of the distributed charge:

$$\left.\begin{aligned} \frac{\rho_v^2}{2\pi\varepsilon_0} \int_0^{\pi} \int_0^{R} \frac{(r_x - r\cos\alpha) r \, d\alpha \, dr}{(r^2 + r_x^2 - 2 r r_x \cos\alpha)^{3/2}} &= \frac{m_v}{\sqrt{(1 - v^2/c^2)^{3/2}}} \times \frac{dv}{dt}, \\ V &= \frac{dx}{dt}, \end{aligned}\right\} \tag{4}$$

where r_x is the radius of a layer of the electron beam, x is the expansion coordinate, and $c = 3 \times 10^8$ m/s is the speed of light.

The magnetic field compressing a paraxial electron beam is due to the Lorentz force, $df_{\mathrm{L}} \approx q_1[cB]$, and the magnetic induction B at the boundary of the beam layer with radius r is determined by the relation

$$B = \frac{\mu_0 r}{2\pi R^2} I_m . \tag{5}$$

Hence the Lorentz force F_{L} for the corresponding layer is

$$F_{\mathrm{L}} = \int_0^{\pi} \int_0^{r_x} \frac{\mu_0 I_m}{\pi R^2} c\rho_v r \, dr \, d\alpha. \tag{6}$$

The system of equations that takes account of the electric and magnetic fields and makes it possible to determine the expansion of the layers of the electron beam inside a vacuum diode and on the anode has the form

$$\left.\begin{aligned} &\frac{R^2\rho_v^2}{2\varepsilon_0}\int_0^{\pi}\int_0^{R}\frac{(r_x - r\cos\alpha) r \, d\alpha \, dr}{(r^2 + r_x^2 - 2rr_x\cos\alpha)^{3/2}} \\ &- \frac{\mu_0 c\rho_v I_m}{\pi R^2}\int_0^{\pi}\int_0^{r_x} r^2 dr \, d\alpha = \frac{\pi R^2 m_v}{\sqrt{(1 - v^2/c^2)^{3/2}}} \times \frac{dv}{dt}, \\ &v = \frac{dx}{dt}. \end{aligned}\right\} \tag{7}$$

The results of calculations of the expansion of an electron beam inside a vacuum diode with a cold flat cathode with radius $R = 2$ mm and a 9 mm cathode–anode gap are presented in Fig. 2a. The expansion of the beam near the anode (X_A) depends strongly on the maximum current I_m flowing between the cathode and the anode. The inner layers with radius $r_x < 0.5$ R of the beam expand very little, and the outer layers ($r_x \approx 0.85R$) and especially the boundary layers ($r_x \approx R$) experience substantial electrostatic repulsion. Expansion is mainly due to electrostatic forces. The magnetic field has a smaller effect. This is illustrated by the family of curves in Fig. 2a for the beam layers $r_x = 0.85R$ and $r_x = R$. The dashed curves show the expansion (X_A) under the action of electrostatic forces only, and the solid lines show the combined effect with a magnetic field. For weak electron-beam currents (< 0.3 kA), beam expansion is relatively small, but for currents ~ 1 kA and higher the boundary and adjoining layers move apart substantially. The experimental confirmation of the computed estimates is given in Fig. 2b, which shows the electron-beam structure (track) recorded at the anode by a sensitive film placed on the backside of the anode, for which thin-walled beryllium or titanium, which are transparent to high-energy electrons, is used. For the maximum beam current ~ 0.3 kA the track essentially corresponds to the cathode area (the beam divergence is small), but for a ~ 2 kA current the track covers an area with a much larger radius than the cathode radius — the beam expands strongly, as a result of not only the boundary but also the adjoining inner layers.

The computational estimates presented could be helpful for determining the impedances of a vacuum diode in the picosecond channels of electronic radiation of high direct current accelerators.

This work was supported by the International Science and Technology Center, project No. 510–97, financed by the European Society.

[1] K. A. Zheltov, S. A. Korobkov, A. N. Petrenko, and V. F. Shalimanov, Prib. Tekh. Éksp. No. 1, 37 (1990).
[2] A. A. Rukhadze, L. A. Bogdankevich, S. U. Rosinskiĭ, and V. G. Rukhlin, *The Physics of High-Current Relativisitic Electron Beams* (Atomizdat, Moscow, 1980).
[3] A. N. Didenko, V. P. Grigor'ev, and Yu. P. Usov, *High-Power Electron Beams and Their Applications* (Atomizdat, Moscow, 1977).
[4] I. V. Alyamovskiĭ, *Electron Beams and Electron Guns* (Sov. Radio, Moscow, 1966).
[5] B. M. Yavorskiĭ and A. A. Detlaf, *Handbook of Physics* (GIFML, Moscow, 1963), p. 488.

Translated by M. E. Alferieff

Application of resonant Raman scattering of light for plasma diagnostics

G. T. Razdobarin, R. R. E. Salomaa, M. I. K. Santala, and S. Yu. Tolstyakov

A. F. Ioffe Physicotechnical Institute, Russian Academy of Sciences, St. Petersburg, Russia; Helsinki University of Technology, Helsinki, Finland

(Submitted June 16, 1999)
Pis'ma Zh. Tekh. Fiz. **25**, 46–54 (September 26, 1999)

An application of a diagnostics method based on the scattering of laser radiation by atoms in plasma is discussed. The high sensitivity of the method is due to resonant enhancement of the Raman scattering cross section with a small offset from the exact optical resonance with an intermediate level. The measurements of the spatial distribution of the excited argon atoms were performed in the plasma of a high-frequency induction discharge in a wide range of offsets from exact resonance under the conditions of linearity and with saturation of the scattering intensity. The results of the experiments are used to analyze the sensitivity of the method and to formulate the requirements for diagnostics so as to optimize the experimental conditions. [S1063-7850(99)02409-X]

Raman scattering of light is conventionally used in spectroscopic investigations as an effective method for studying the structure of molecules and their interaction with a medium. The use of tunable lasers has greatly expanded the range of objects accessible for investigation. This is due to, first and foremost, the possibility of selecting a lasing wavelength near an optical resonance, as a result of which the Raman scattering cross section is many orders of magnitude larger.[1] The results of theoretical and experimental investigations of near-resonance Raman scattering are presented in many works. Some of them are relevant to plasma diagnostics.[2–4] The essence of the diagnostics method is that the plasma is illuminated by laser radiation at a wavelength close to an optical resonance of an absorption line. The scattered radiation is observed directly at the laser wavelength or at other wavelengths corresponding to combination frequencies for a transition from a virtual into shifted levels. We note that Raman scattering is preferable for plasma diagnostics problems because the large difference between the probe and the scattered radiation wavelengths makes it possible to eliminate noise from the parasitic scattering signal. For the same reason there is no noise due to scattering of light by electrons. The radiation studied is collected from a small volume of the plasma, where the laser beam overlaps with the cone of observation rays and therefore contains information about local parameters of the plasma. The offset from exact resonance makes it possible to eliminate the possible measurement errors due to reabsorption, which is especially important when studying plasma with a large optical thickness. As a result of the offset, there is no background due to the characteristic plasma radiation on the line of the optical transition, which is the main source of noise for plasma diagnostics by the resonance fluorescence method.[5]

The specific features arising in Raman scattering as a result of the large contribution of collisional relaxation must be taken into account in the formulation of plasma diagnostics experiments. For plasma with a sufficiently high charged-particle density the ratio of the transverse and longitudinal relaxation rates can be much greater than 1.[6] This has a large effect on the population dynamics of the levels of the transition excited in the field of a light wave[7] and ultimately makes the analysis of scattering processes more complicated. The new diagnostics method is aimed at optimizing the experimental conditions so as to eliminate, when possible, any influence of the model constraints due to collisional (transverse) relaxation and to increase sensitivity. The main problem of the experiments performed was methodological work, first and foremost, the investigation of scattering signals in a wide range of offsets from exact resonance and also the dependence of the scattering intensity on the flux density of the probe beam.

The Raman scattering experiments were performed in the argon plasma of an induction rf discharge in a gas flow at atmospheric pressure. The typical electron densities and temperatures for such a discharge are $n_e \sim 10^{15}$ cm^{-3} and $T_e \leqslant 1$ eV.[8] A simplified scheme of the levels of the excited transitions is shown in Fig. 1. A dye laser with controllable offset from exact resonance with the $1s_5-2p_2$ transition at wavelength 696.5 nm was used to excite the scattering signal. The scattered radiation was observed near the wavelength 772.4 nm of the $2p_2-1s_3$ transition. The oscillator strengths for the chosen transitions are $f_{1s_5-2p_2}=0.03$ and $f_{1s_3-2p_2}=0.34$. The energy and duration of the probe pulse were 1–2 mJ and 10 ns, and the pulse repetition frequency reached 25 Hz. The scattering volume was projected with two-fold reduction onto the input slit of a monochromator. Radiation at the output of the device was detected with a photomultiplier. In various experiments the scattering volume was chosen from $\sigma \sim 10^{-4}$ to $\sim 10^{-3}$ cm^3. The solid angle for collecting the scattered radiation in a direction perpendicular to the probe axis was 5.6×10^{-3} sr. To increase the measurement accuracy, multipassage probing of the plasma was used (Fig. 2), and the scattered signals were accumulated over several tens of laser pulses. Absolute calibration of the sensitivity of the apparatus was performed by

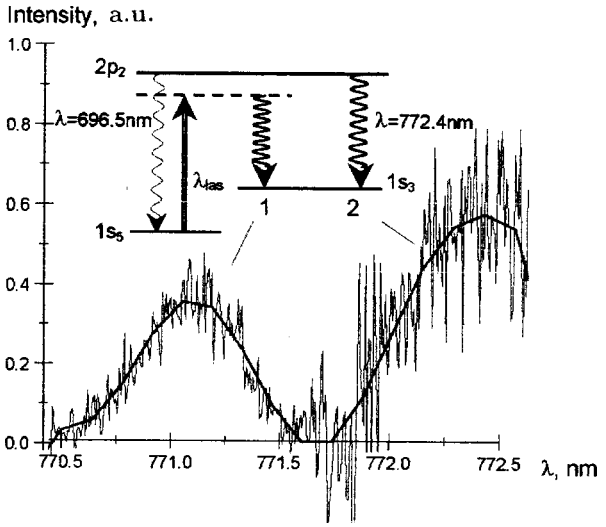

FIG. 1. Trace of Raman signals *1* and fluorescence signals *2* (spectral resolution 0.65 nm, laser wavelength offset from exact resonance 1 nm). A simplified scheme of the levels of the excited transitions is shown at the top of the figure.

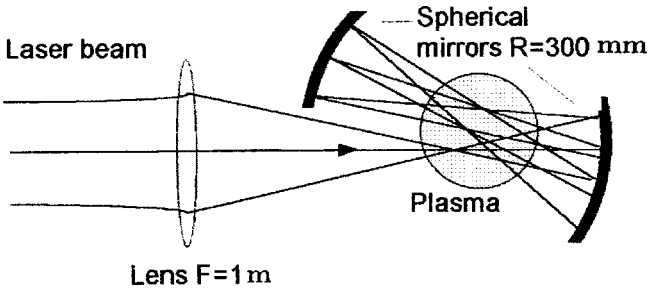

FIG. 2. Multipassage probe scheme.

the well-known method of Raman scattering by nitrogen molecules at frequencies corresponding to rotational transitions.[9] The spectral sensitivity of the apparatus was measured using a calibrated incandescent lamp.

Figure 1 shows Raman scattering and fluorescence signals on the background due to the characteristic plasma radiation, which were excited simultaneously by the laser radiation with a spectral offset of 1 nm from exact resonance. The fundamental difference of the long- and short-wavelength sections of the spectrogram which are presented in the figure is that the accuracy with which the fluorescence signals are detected is determined exclusively by the background due to the plasma line radiation, which is almost three orders of magnitude stronger than the continuum. At the same time, the accuracy of Raman signal detection depends on the strength of the signal itself (about 100 photoelectrons for the maximum readings in the spectrogram) and is virtually independent of the background due to the continuous spectrum.

The effect of the background due to the continuous spectrum could become substantial as the Raman scattering signal decreases with increasing offset. This is evident from Fig. 3, which shows the results of measurements of the Raman scattering signal intensity for different offsets of the laser wavelength up to 2 nm. The figure also shows the theoretical dependence of the scattering intensity $\sim\lambda^{-2}$ in accordance with the Lorentz function.

It is well known that as the flux density of the probe radiation increases, the scattering intensity ceases to depend linearly on the incident flux and reaches saturation in the limit.[10,11] Saturation of scattering creates definite conveniences for plasma diagnostics. Specifically, when the probe beam is collimated, observation of scattering from a small plasma volume increases the signal-to-background ratio. In addition, the strength of the detected signal with saturation of the scattering intensity no longer depends on the rates of collisional relaxation processes. We measured the nonlinear dependence of the Raman scattering intensity on the flux density of the probe radiation with a fixed offset of 1 nm from exact resonance. The measured values of the scattering signals for a number of values of the lasing energy (spot diameter 0.2 mm) are presented in Fig. 4. A least-squares

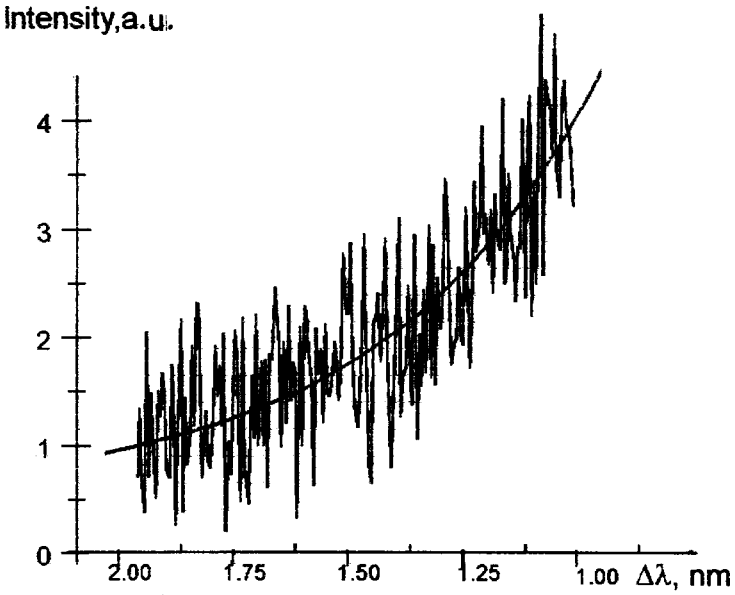

FIG. 3. Raman signal intensity versus the laser wavelength offset.

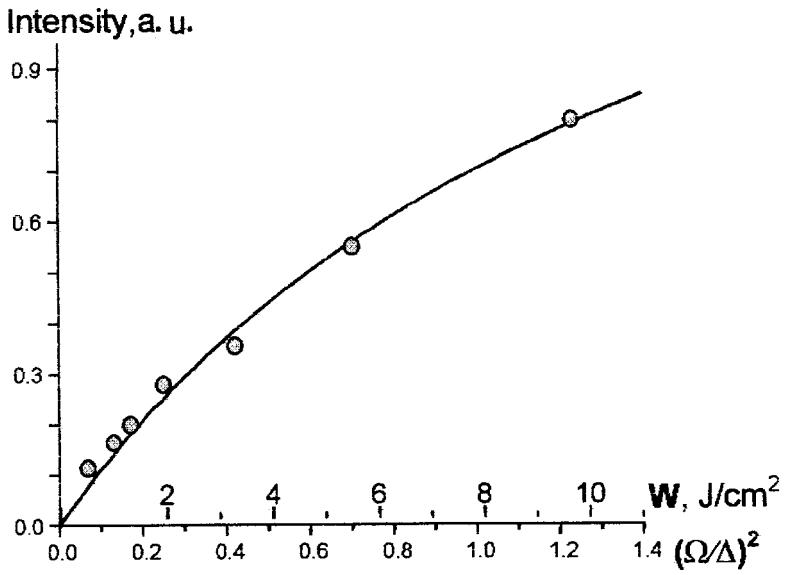

FIG. 4. Raman scattering intensity versus the probe energy density.

curve is drawn through the experimental points according to the data of Ref. 11 assuming that the collisional relaxation rate is much higher than the radiative decay rate. The squared Rabi frequency, scaled to the frequency offset $(\Omega/\Delta)^2$, corresponding to the best fit curve, are plotted along the abscissa together with the probe energy density. The quantity $(\Omega/\Delta)^2$ can be interpreted as the ratio of the flux density of the probe to its saturation value (saturation parameter). As one can see from the figure, for the chosen beam geometry and a 1 nm offset, the saturation condition $(\Omega/\Delta)^2=1$ corresponds to a probe energy density ~ 8 J/cm^2,

The results of measurements of the radial density distribution of excited argon atoms over the cross section of the flame are presented in Fig. 5. The measurements were performed by scanning the observation axis along the laser beam (across the plasma flame) with a 0.7 mm step and averaging the readings over several tens of laser pulses at each scanning step. The spatial resolution along the beam was 1 mm with the beam focused into a 0.5 mm in diameter spot. The measurements were performed in the absence of saturation of the scattering intensity. In this case, there was no need to take account accurately of the spatial nonuniformity of the beam, which has the same effect on the measurement results for the intensities of the useful and the calibration scattering signals. The measured density profile in Fig. 5 shows a detailed picture of the formation of the plasma flame with a large disruption of axial symmetry. We note that the observations of the 772.4 nm line, corresponding to the $2p_2-1s_3$ transition, along a chord do not give the true distribution of atomic densities because of radiation reabsorption.

Under the conditions of our experiment the background due to the continuous spectrum did not produce any special problems for plasma-to-probe beam diameter ratios ~ 10. Under these conditions the lower limit of the measurable atomic densities is determined by the statistical variance of the detected number of photoelectrons at the photocathode of the photomultiplier that correspond to the scattering signal. If the conditions of our experiment are extrapolated to other

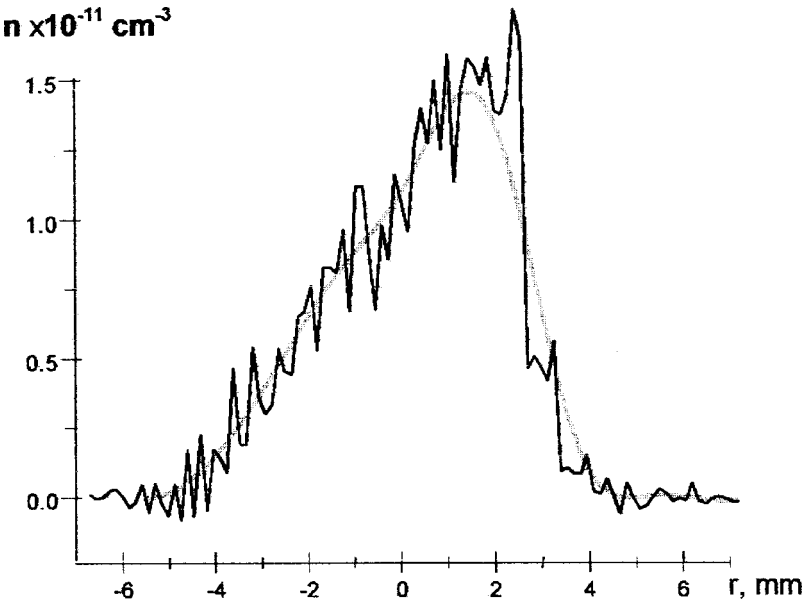

FIG. 5. Radial density distribution of excited argon atoms in the $1s_5$ level over the cross section of the flame.

large plasma objects, then for a saturating laser flux density the maximum measurable number of atoms in a single laser pulse in a resolvable volume ~ 1 cm^3 is $\sim 10^7$ for transitions at the Raman frequencies with oscillator strength ~ 1. For weaker lines, the limiting measurable densities increase inversely as the oscillator strength. On the basis of the saturation conditions, the laser energy should increase quadratically with increasing offset from exact resonance. According to the results of our experiments, for a detuning of 1 nm from exact resonance, probe wavelength 700 nm, and pulse duration ~ 10 ns the required beam energy density for $(\Omega/\Delta)^2 = 1$ is $\sim 0.25/f$ (J/cm^2), where f is the oscillator strength for a transition near the lasing line. The transmission of the spectrometers employed limits the decrease in the spectral offset beyond the limits of the Doppler width of the absorption contour. Fabry–Perot interferometer based spectrometers with higher transmission will make it possible to have for the same source dimensions a smaller spectral offset and thereby substantially to decrease the energy requirements for probing plasma.

[1] G. Placzek, *Handbook der Radiologie* (VI Akademische Verlagsgesellschaft, Leipzig, 1934) Vol. 2.
[2] H. F. Döbele and K. Hirsch, Phys. Lett. A **54** 267 (1975).
[3] W. G. Wrobel, K. H. Steuer, and H. Röhr, Phys. Rev. Lett. **37**, 1218 (1976).
[4] L. Vriens and M. Adriaansz, J. Appl. Phys. **45**, 4422 (1974).
[5] G. T. Razdobarin and I. P. Folomkin, Zh. Tekh. Fiz. **49**, 4422 (1974) [Sov. Phys. Tech. Phys. **24**, 753 (1974)].
[6] H. Griem, *Spectral Line Broadening by Plasmas* (Academic Press, New York, 1974; Mir, Moscow, 1978).
[7] S. G. Rautian, G. I. Smirnov, and A. M. Shalagin, *Nonlinear Resonances in the Spectra of Atoms and Molecules* (Nauka, Novosibirsk, 1979).
[8] J. M. De Regt, R. A. H. Engeln, F. P. J. de Groote *et al.*, Rev. Sci. Instrum. **66**, 3228 (1995).
[9] J. Hovard *et al.* J. Phys. D **12**, 1435 (1979).
[10] J. L. Carlsten, A. Szöke, and M. G. Raymer, Phys. Rev. A **15**, 1029 (1977).
[11] E. Courtens and A. Szöke, Phys. Rev. A **15**, 1588 (1977).

Translated by M. E. Alferieff

Growth of A^3N whiskers and plate-shaped crystals by molecular-beam epitaxy with the participation of the liquid phase

V. V. Mamutin

A. F. Ioffe Physicotechnical Institute, Russian Academy of Sciences, St. Petersburg, Russia
(Submitted May 26, 1999)
Pis'ma Zh. Tekh. Fiz. **25**, 55–63 (September 26, 1999)

It is shown that InN and GaN whiskers and plate-shaped crystals can be grown by molecular-beam epitaxy (MBE), and the growth mechanism on gallium arsenide and sapphire substrates is investigated. A comparison is made with the theory. It is proved that the growth mechanism corresponds to the vapor–liquid–solid (VLS) mechanism, and the parameters of the crystallization process are determined. The nanometer sizes of the crystals grown give hope that the crystals and the VLS growth method itself can be used to obtain quantum-size objects (quantum dots and wires) by MBE in the promising system of elements A^3B^5–AlGaInN.
 [S1063-7850(99)02509-4]

Spatial confinement of carriers in low-dimensional structures (quantum wells, wires, dots) gives rise to the special properties of such structures and the great interest in semiconductor devices (lasers, photodetectors, transistors, nonlinear switches, and so on). The production of such structures involves either self-organization or specific self-orientation during growth. The self-organization processes have been studied in many recent works,[1–3] whereas directed growth of low-dimensional crystals (whiskers, plate-shaped, and hollow) has receded somewhat into the background after its mechanism was discovered,[4] though the dimensions of the objects obtained are close to those obtained in the last few years (nanometer and subnanometer range) by methods such as the molecular-beam epitaxy (MBE).

To date there have been no reports of growth of such crystals in high vacuum, in which MBE is performed. A growth mechanism, called the ''vapor–liquid–solid'' (VLS) mechanism,[4] has been proposed and confirmed. The process must be conducted in the temperature and supersaturation range where kinetic constraints inhibit the thermodynamically possible reaction. In practice, this could mean that the temperature must be 100–200 °C lower than the usual epitaxy temperature. In the early works on the growth of A^3B^5 compounds from vapor, whiskers and dendritic crystals formed randomly and were viewed as a curiosity or an undesirable product of crystallization. After the discovery of the VLS mechanism, the deliberate growth of A^3B^5 whiskers was reported in a number of publications.[5,6] Little information is available on the oriented growth of such crystals, while this type of growth makes it possible to understand the mechanism itself and opens the way to practical applications of whisker structures. In addition, the literature on self-organizing processes contains absolutely no information on the growth of quantum-size objects by the VLS mechanism.

It is significant that the experimental facts obtained on such objects fit well within the modern ideas on nucleation, layered ($2D$) growth (layer-by-layer mechanism), the role of impurities in surface kinetics (so-called surfactant mechanism), and growth of liquid and quasiliquid phases even in processes presuming the existence of only gas and solid phases, as for example, MBE.[7] Surface force effects make it possible to measure many parameters of the process that are inaccessible for measurement under other conditions and to establish the most general laws of growth.

In the present work A^3B^5 whiskers and plate-shaped crystals were grown for the first time by MBE in a nitride system (the binary compounds InN and GaN which are now being widely investigated), a comparison was made with theory,[8,9] and their growth mechanism was analyzed. Growth on GaAs (311) substrates was conducted in the EP-1203 MBE system with a novel coaxial magnetron source of nitrogen plasma with rf capacitive excitation of the discharge[10] as well as on Al_2O_3 (0001) substrates using a source with electron cyclotron resonance (ECR) ASTEX (USA).

The crystals were studied with a CamScan (England) scanning electron microscope (SEM). The experimental data were analyzed mainly for InN whiskers, which give the brightest pattern of whisker and plate-shaped growth, when the usual planar growth is suppressed (possibly because of the much lower growth temperatures: 370–500 °C for InN instead of 600–800 °C for GaN). The typical SEM images are presented in Fig. 1. It is evident from the scale shown in the figures that the whiskers can vary strongly in size — from tens of nanometers in diameter to tens of microns in length.

If the possibility of the existence of the VLS mechanism is considered, then it is obvious that in order for a liquid drop of metal to exist on a surface and a crystal to grow beneath it at the same time, the arriving flux (J_{ads}) must equal the re-evaporated flux (J_{des}): $\Delta J^3=(J^3_{ads}-J^3_{des})=\Delta J^5=(J^5_{ads}-J^5_{des})$. Of course, a flat film can also grow ($2D$ growth) in this case, if the conditions for this are not artificially suppressed on the remaining surface (for example, by selecting a plane with a much lower growth rate, such as $\langle 111\rangle$ in many semiconductors).

The following possibilities occur.

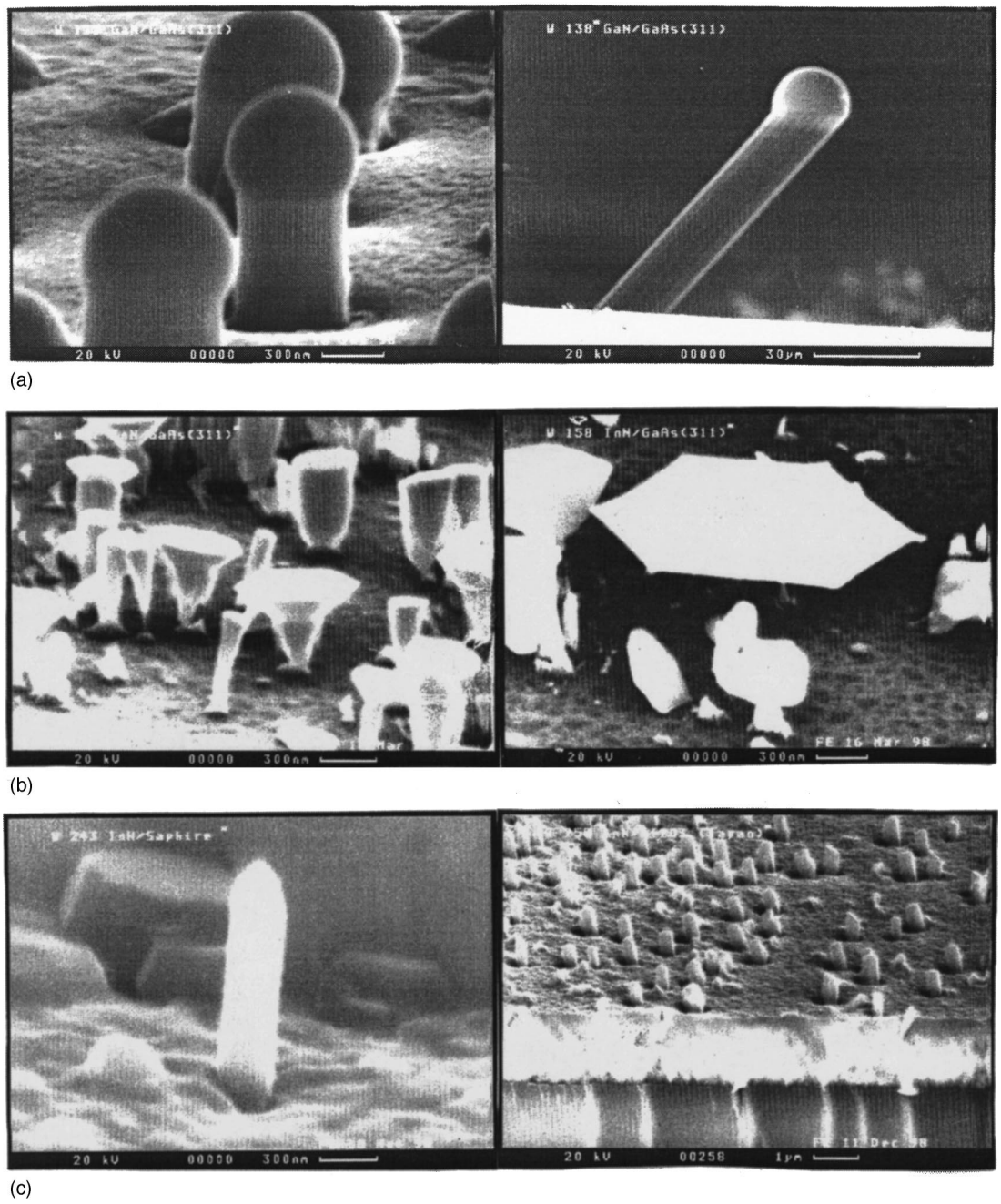

FIG. 1. SEM photographs of InN and GaN whiskers and plate-shaped crystals: a — GaN/GaAs(311), b — InN/GaAs(311), c — InN/Al_2O_3(0001).

1. $\Delta J^3 \geqslant \Delta J^5$. A drop increases in size continuously and rapidly, and supersaturation (growth rate) decreases in it. For large decreases of supersaturation, whisker growth stops. (Indium (A^3)-enriched growth conditions far from stoichiometry.)

2. $\Delta J^3 \geqslant \Delta J^5$. Conical crystals, expanding toward the vertex because of slow growth of drops or slowly growing drops on a flat layer, will grow. (A^3-enriched growth near stoichiometry (A^3: $B^5 \simeq 1:1$)).

3. $\Delta J^3 \leqslant \Delta J^5$. Conical crystals, tapering toward the vertex on account of the gradual decrease in the drop sizes, will grow. Planar growth without drops with an A^3 deficiency is possible. (Nitrogen-enriched growth near stoichiometry.)

4. $\Delta J^3 \ll \Delta J^5$. A drop can vanish or solidify in the form of a polycrystal, if the supersaturation exceeds a critical level at which spontaneous crystallization starts. (Nitrogen-enriched growth far from stoichiometry.)

The characteristic indicators of the VLS mechanism are as follows: 1) the length-to-diameter ratio of a whisker $L/d \geqslant 10$; 2) the growth rate is a quadratic function of the drop diameter: $V \sim f(1/d^2)$; 3) growth occurs predominantly in the direction of suppressed (or strongly reduced) planar growth under ordinary conditions; 4) faceting of the lateral surface of whiskers (planes of the plate); 5) bending of whiskers in definite crystallographic directions; 6) presence of a spherical liquid or crystallized particle (globules) at the vertex (in addition, its absence does not prove the absence of the VLS mechanism); 7) two-stage growth — rapid increase in whis-

TABLE I. The basic growth parameters of InN whiskers.

N_{samp}	L, 10^{-4} cm	V, 10^{-9} cm/s	d, 10^{-4} cm	b, 10^{-7} cm/s	$\Delta\mu/kT$
158	0.3	4.2	0.07	1.07	0.199
157	0.6	8.3	0.10	1.06	0.279
243	1.2	16.9	0.30	1.05	0.403
252	2.2	19.6	0.5	1.04	0.430

ker length followed by slow thickening (or growth of a flat plate on it).[9] These indicators were all observed in our samples of InN and GaN whiskers (plate-shaped crystals) grown on various substrates (Fig. 1). An ordered arrangement of the whiskers (and drops) along the distinguished directions and prismatic faceting of the whiskers and their vertices or plates — a characteristic indicator of the VLS mechanism — can be seen in the figure.[4]

Growth by the VLS mechanism includes the following stages: 1) transport in the vapor phase, 2) reaction at the vapor–liquid surface, 3) diffusion into the liquid, and 4) crystallization processes on the liquid–solid surface. In Ref. 9 it was shown that the limiting stage of the process is stage 4 — phenomena on the liquid–solid boundary. The law of growth is not known in advance, but it can be determined from experiment,[8] and the dependence of the growth rate on the whisker (drop) diameter can be expressed as[9]

$$\sqrt{V}=(\Delta\mu_0/kT)\sqrt{b}-(4\Omega\alpha_{vs}/kT)\sqrt{b}/d,$$

where $\Delta\mu_0$ is the difference of the chemical potentials on the flat vapor–liquid boundary (as $d\to\infty$), $\Delta\mu_0/kT$ is the effective supersaturation in the vapor phase above a flat surface, Ω is the specific volume, α_{vs} is the specific free energy of the vapor–solid phase boundary, k is Boltzmann's constant, T is the absolute temperature, and b is the kinetic coefficient of crystallization for the liquid–solid boundary (by definition, it does not depend on the supersaturation). The experimental data for several samples of InN whiskers grown with a magnetron source are presented in Table I. Here L is the whisker length, d is the whisker diameter (measured from SEM photographs), V is the whisker growth rate, and the last columns show the kinetic coefficient b and the supersaturation on the crystallization front $\Delta\mu/kT=\Delta\mu_0/kT-(4\Omega_{bs}/kT)/d$ calculated from the dependence $\sqrt{V}=f(1/d)$.[9]

The dependence $\sqrt{V}=f(1/d)$ itself is shown in Fig. 2. Besides the quantities indicated in Table I, d_{crit} — the drop diameter for the given effective supersaturations when the real supersaturations at the crystallization boundary vanish and growth stops — is found from the dependence. In other words, the value below which the increase in the chemical potential below a curved surface (the Gibbs–Thompson effect[9]) completely stops growth for the given supersaturation in the vapor phase. This value is $d=0.04$ μm (for $V=0$). Since the literature contains no data for InN, it was assumed that the specific free energy α_{vs} for InN does not differ much from the published values for Si (1617 ergs/cm^2), Ge (1500 ergs/cm^2), and GaAs (1090 ergs/cm^2),[9] and the value equal in order of magnitude for the compound A^3B^5–GaAs ($\sim$1000 ergs/cm^2) was taken. The slope of the dependence makes it possible to determine the kinetic coefficients for all processes, the saturation on the crystallization front $\Delta\mu/kT$, and the effective saturations $\Delta\mu_0/kT$ in the vapor phase. The latter quantity (for $\sim$700 K — the average growth temperature) was $\Delta\mu_0/kT=0.465$, and all other quantities are given in Table I. The saturated vapor pressure p in the vapor above the curved surface of the drop and above a flat surface (p_0) — the Gibbs–Thompson effect — was $p/p_0\sim\exp(4\Omega\alpha_{vs}/kTd_{cr})\sim1.6$.[9] As assumed, the kinetic coefficient does not change, being a phenomenological parameter expressing the dependence of the process on the driving force.[8]

In conclusion, in this work whiskers and plate-shaped crystals in the system A^3N were grown for the first time by MBE and their growth mechanism was investigated. It was shown that growth occurs by the VLS mechanism with the participation of the liquid phase. Since the main parameters (contact angle, coefficients of embedding, desorption, and adsorption) remain the same for this system of elements, these results can also be used to understand the planar

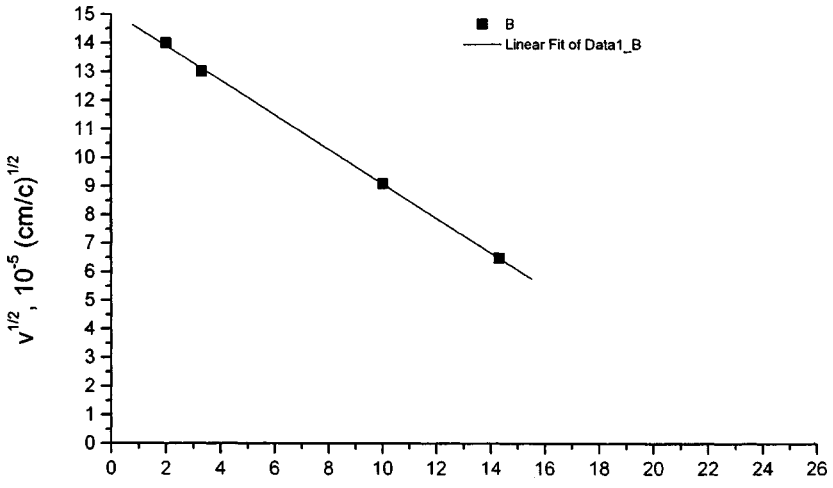

FIG. 2. Growth rate of InN whiskers versus the whisker diameter.

growth of A^3B^5 compounds by MBE, since in many cases it occurs with the participation of liquid or quasiliquid phases on the surface.[7] In addition, controllable growth of nanometer-size nonplanar objects gives hope for obtaining in the future quantum wires (dots) in the A^3N system by the VLS mechanism, opening up additional possibilities for controlling them.

I thank V. M. Busov for obtaining the SEM photographs and for productive discussions.

This work was performed as part of project N 99-02-17103 of the Russian Fund for Fundamental Research and was partially supported by the Russian Fund for Fundamental Research and the ''Physics of Solid-State Nanostructures'' program of the Ministry of Science of the Russian Federation.

[1] R. Notzel, J. Temmyo, and T. Tamamura, Nature **369**, 131 (1994).
[2] M. Yoshizawa, A. Kikuchi, and M. Mori, Jpn. J. Appl. Phys., Part 2 **36**, L459 (1997).
[3] M. Yoshizawa, A. Kikuchi, N. Fujita *et al.*, J. Cryst. Growth **189/190**, 138 (1998).
[4] R. S. Wagner and W. C. Ellis, Appl. Phys. Lett. **5**, 89 (1964).
[5] S. M. Polyakov, E. N. Laverko, and V. M. Marakhonov, Kristallogr. **15**, 598 (1970) [Sov. Phys. Crystallogr. **15**, 519 (1970)].
[6] M. Koguchi, H. Kakibyashi, and M. Yazawa, Jpn. J. Appl. Phys., Part 1 **31**, 2061 (1992).
[7] S. V. Ivanov, P. S. Kop'ev, and N. N. Ledentsov, J. Cryst. Growth **111**, 151 (1991).
[8] A. A. Chernov, Kristallogr. **16**, 842 (1971) [Sov. Phys. Crystallogr. **16**, 734 (1971)].
[9] E. I. Givargizov and A. A. Chernov, Kristallogr. **18**, 147 (1973) [Sov. Phys. Crystallogr. **18**, 89 (1973)].
[10] V. V. Mamutin, V. N. Zmerik, and V. A. Vekshin, Tech. Phys. Lett. **24**(6), 467 (1998).

Translated by M. E. Alferieff

Radar sounding of hydroacoustic disturbances of the sea surface

I. E. Ushakov and I. F. Shishkin

North-West Correspondence Polytechnical Institute, St. Petersburg, Russia
(Submitted May 12, 1999)
Pis'ma Zh. Tekh. Fiz. **25**, 64–73 (September 26, 1999)

The results of an experimental investigation of the interaction of hydroacoustic and electromagnetic fields at an air–water interface under laboratory conditions are reported. It is shown that this phenomenon can be used under natural conditions to transmit information from an underwater source to a receiver located in the atmosphere. © *1999 American Institute of Physics.* [S1063-7850(99)02609-9]

One of the pressing problems in monitoring the condition of the world's oceans is transmitting information from underwater sources to receivers located in the atmosphere. The optimal information carrier in dense conducting media, such as seawater, is an acoustic wave. However, an acoustic field does not penetrate into air very well and is attenuated comparatively rapidly there, so that the direct detection of acoustic signals at large distances from the interface is impossible. Remote reading of an acoustic signal is possible using microwave electromagnetic radiation and resonance volume scattering by an acoustic wave in air near the interface or phase modulation of the reflections from the interface, which oscillates under the action of the hydroacoustic signals on it. The characteristics of the first method of reading were investigated in Refs. 1–3, and in Refs. 4–6 it was shown that the second method is in principle realizable. The experimental investigation whose results are reported in the present letter was conducted in order to make an assessment of the possibility of practical applications of the second method under natural conditions.

The experimental investigation of the method of remote detection of a hydroacoustic signal according to the phase modulation of microwave reflections from the air–water interface was conducted in the tank at the Science and Industrial Association ''D. I. Mendeleev All-Russia Scientific-Research Institute of Metrology.'' The experimental conditions and the arrangement of the apparatus corresponded to Ref. 3.

The frequency of the hydroacoustic oscillations was 3.3 kHz. The microwave (3.2 cm) receiver–transmitter was placed in a cab which was moved by an overhead track hoist in the space above the tank. After the phase detector, the signal entered a selective amplifier tuned to the frequency of the acoustic oscillations. The signal from the output of the selective amplifier was recorded with a level plotter.

The amplitude of the vibrations of the water surface is related with the density P_S of the acoustic power flux at the interface as

$$A=(2P_S/\rho\nu)^{1/2}/(2\pi f), \tag{1}$$

where f is the frequency of the oscillations, ρ is the density of the liquid, and v is the velocity of sound in water.

The value of P_S is related with the power P_a and delth H of the hydroacoustic source as

$$P_S=GP_a/(4\pi H^2), \tag{2}$$

where G is the gain of the radiator.

From the relation (1), using Eq. (2) and substituting the values for water $\rho=10^3$ kg/m^3 and $\nu=1.5\times10^3$ m/s, we obtain

$$A=0.5\times10^{-11}(GP_a)^{1/2}/(fH). \tag{3}$$

The voltage at the output of the selective amplifier is proportional to the amplitude of the vibrations.[4] Therefore we can write

$$u\sim(GP_a)^{1/2}/(fH). \tag{4}$$

Figure 1 shows examples of the traces on the recorder chart for the acronym VNIIM transmitted in Morse code. The hydroacoustic radiator was located at a depth of 0.9 m, and the cab with the receiver–transmitter for reading information from the water surface was located 4.0 m from the water surface. Analysis of the traces presented shows that in all cases information is transmitted without distortion.

To obtain the experimental dependences for each 45–60 s realization, the values of the contrast $K=\overline{u_s}/\overline{u_n}$, where $\overline{u_s}$ and $\overline{u_n}$ are the average values of the voltage at the output of the selective amplifier with the sound source switched on and off, respectively, were determined. The contrast as a function of the various measurement conditions is presented in Fig. 2.

Figure 2a shows the values of the contrast (the vertical line characterizes the range of individual realizations) with the radar located 3.0 m above the undisturbed water surface for different depths of the hydroacoustic source. The figure also shows that theoretical dependence from Ref. 4. The discrepancy between the experimental and theoretical values for $H=0.5$ m is explained as follows. If only the part S_2 of the surface S_1 irradiated by the radar antenna vibrates, then the contrast

$$K=K_{\max}(S_2/S_1)^{1/2}, \tag{5}$$

where $K_{\max}$ is the contrast that would be obtained if the entire surface S_1 vibrated. Since the hydroacoustic field is spherical, Fresnel zones are formed on the water surface.

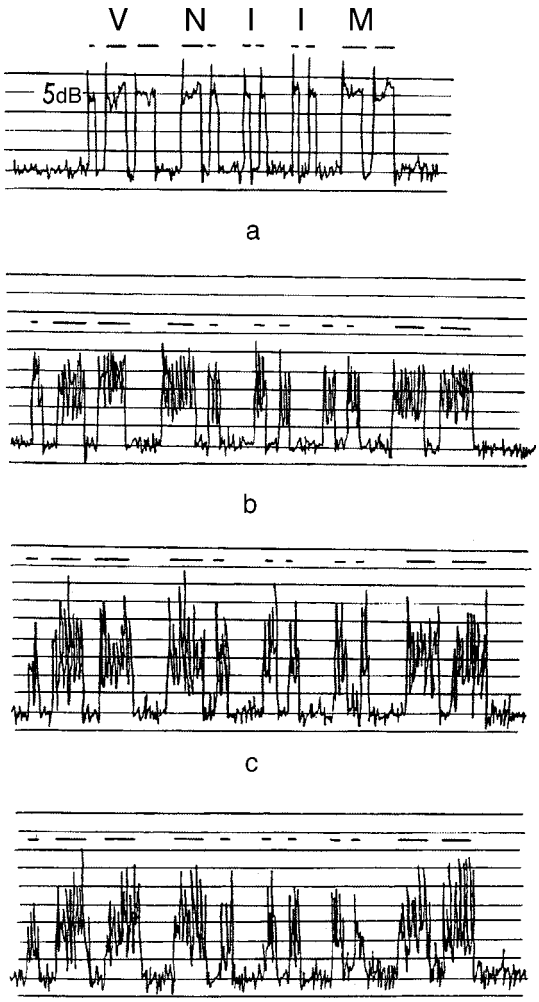

FIG. 1. Examples of the recorder traces ($H=0.9$ m, $h=4.0$ m): a — calm water and stationary cab; b — calm water and rocking cab, c — waves on the water surface and stationary cab, d — waves on the water surface and rocking cab.

Sound oscillations at the boundaries of these zones occur in antiphase. The radius of the section in which the phase of the oscillations differs by not more than $\pi/2$ (region of quasi-in-phase vibrations) is

$$r=[\lambda_a(H-\lambda_a/8)/2]^{1/2}, \tag{6}$$

where λ_a is the acoustic wavelength in water. The experimental results corrected taking this into account, shown in Fig. 3 by the dashed line, agree well with the theoretical values.

It should be noted that the effect of the incoherence of the vibrations on different sections of the surface waves must be taken into account when choosing the operating frequency of the hydroacoustic radiator. The condition

$$\lambda_a \geqslant 4h_{\max}, \tag{7}$$

where $h_{\max}$ is the maximum height of the sea waves, must be satisfied in order that the phase difference between the vibrations at the crest and in the trough of the sea waves not exceed $\pi/2$. Therefore lower sound frequencies must be used as the waves intensify. However, these frequencies should lie above the spectrum of Doppler frequencies of the reflected signal, which are due to the waves. Therefore the radar frequency must be decreased in this case. On the other hand, when the radar frequency is decreased, the sensitivity of the system decreases, since the degree of phase modulation decreases. These considerations show that an adaptive selection of the frequency of hydroacoustic and electromagnetic waves can be used.

The dependence of the contrast on the voltage U_{ac}, apply to the electroacoustic transducer (Fig. 2b), is nearly linear $K\sim U_{ac}$. The increase in the difference of the contrasts with increasing U_{ac} is due to the nonlinear dependence of the acoustic power on the voltage applied to the transducer.

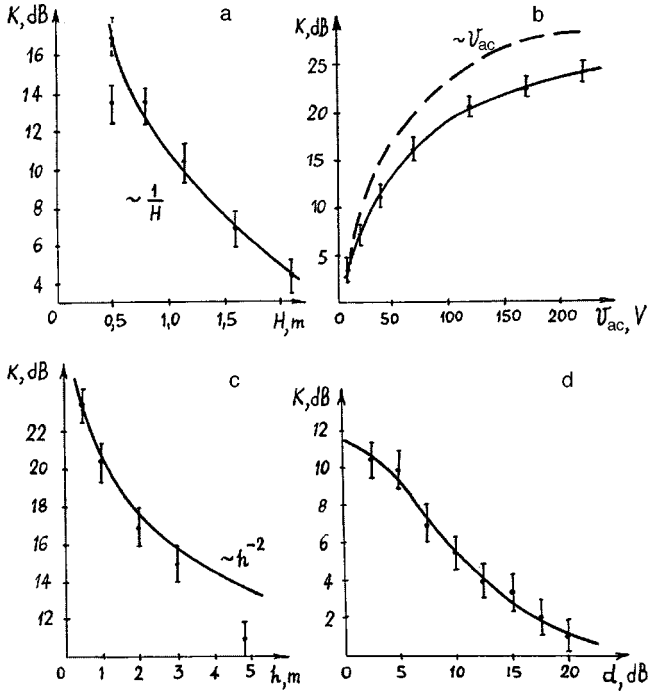

FIG. 2. Contrast versus a — the depth of the sound source ($h=3.0$ m), b — the voltage of the sound frequency ($h=0.5$ m), c — the height of the radar ($H=0.65$ m), and d — the attenuation of the received signal ($H=2.2$ m, $h=3.0$ m).

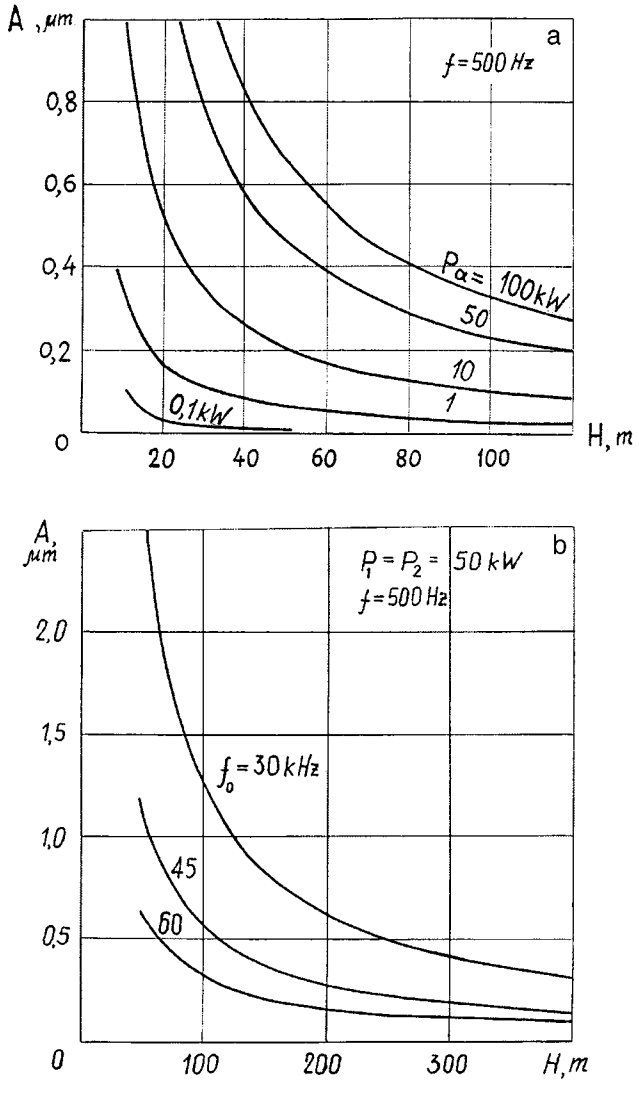

FIG. 3. Vibration amplitude versus the depth of nondirectional (a) and parametric (b) radiators.

The dependence of the contrast on the height of the radar system above the water surface is presented in Fig. 2c. The deviation of the experimental results from the theoretical dependence $K \sim h^{-2}$ with increasing height is due to the fact that the area irradiated by the radar becomes larger than the region of quasi-inphase vibrations.

The dependence of the contrast on the attenuation of the reflected signal (Fig. 2d) shows that the radar employed can be used to detect at height of 30 m the perturbations of the water surface by the sound source employed with a contrast of not less than 1 dB. The pressure 1 m from the radiator was 6300 Pa, which gives $A=0.13\,\mu$m for the estimated amplitude of the vibrations of the water surface.

We shall now estimate the limiting values of the depth of the hydroacoustic source and the height of the radar system on the basis of our experimental results.

Figure 3a shows the dependence, calculated from Eq. (3), of the vibration amplitude on the depth of the nondirectional ($G=1$) source of sound. It is evident from the figure that even with high hydroacoustic radiation power the amplitude of the vibrations of the water surface decreases to $0.2\,\mu$m when the source is at a deptj of the order of 120 m.

One promising avenue for forming a narrow directional pattern of radiators at low frequencies is to use parametric acoustic antennas.[7,8]

In this case the power emitted at the working frequency $f=f_1-f_2$ is determined by the expression[7]

$$P_a=3.4\times10^{-15}P_0^2 f^2/(2\Theta)_0^2, \tag{8}$$

where $P_0=P_1+P_2$ is the sum of the powers of the emitted signals (in W); f_1 and f_2 are the frequencies of the initial vibrations (in Hz); $(2\Theta)_0$ is the width (in degrees) of the directional pattern of the parametric radiator at the 3 dB level and is given by

$$2\Theta=4[(\alpha_1+\alpha_2-\alpha)/(k_1-k_2)]^{1/2}, \tag{9}$$

where α_1, α_2, and α are the absorption coefficients for acoustic oscillations of sea water at the primary frequencies and at the difference frequency, respectively; k_1 and k_2 are the wave numbers of the initial oscillations. Since the working frequency is much lower than the initial frequencies, and the latter are close to one another, we can write

$$\left.\begin{aligned}&\alpha_1\approx\alpha_2\approx\alpha_0,\\&\alpha_1+\alpha_2\gg\alpha,\end{aligned}\right\} \tag{10}$$

where α_0 is the absorption coefficient at the frequency $(f_1+f_2)/2$. From the expression (9) we obtain, using Eq. (10) and the equality $k_1-k_2=2\pi f/v$,

$$2\Theta\approx4\times[\alpha_0 v/(2\pi f)]^{1/2}. \tag{11}$$

The area of the ocean surface that is excited by the hydroacoustic energy is

$$S=\pi H^2\tan^2\Theta\approx\pi H^2\Theta^2. \tag{12}$$

Taking account of the relations (8), (11), and (12), the flux density of the acoustic power at the air–water interface can be expressed as

$$P_S=P_a/S\approx2.62\times10^{-20}[\pi^{3/2}P_0 f^2/(\alpha_0 v H)]^2. \tag{13}$$

In accordance with the expression (1), using the relation (13), we obtain for the amplitude of the vibrations

$$A\approx1.14\times10^{-10}\pi^{1/2}P_0 f/(\alpha_0 v^{3/2}\rho^{1/2}H). \tag{14}$$

The absorption coefficient can be determined from the formula[7]

$$\alpha_0=16\times10^3\pi^2\mu_s(1+0.75\mu_v/\mu_s)f_0^2/(3\rho v^3), \tag{15}$$

where μ_s and μ_v are, respectively, the shear and volume viscosities of the liquid.

From the expression (14), substituting the expression (15) and the values for water $\mu_s=0.001\,\text{Pa}\cdot\text{s}$, $\mu_v/\mu_s=2.81$, $v=1500\,\text{m/s}$, and $\rho=10^3\,\text{kg/m}^3$, we obtain

$$A\approx2.24\times10^{-3}P_0 f/(f_0^2 H). \tag{16}$$

The dependence $A(H)$ calculated using Eq. (16) is presented in Fig. 3b. It is evident from this figure that a parametric radiator makes it possible to excite vibrations of the air–water interface with amplitude greater than $0.2\,\mu$m with the acoustic source placed at depths greater than 400 m.

Taking account of the characteristics of the means employed in performing this experiment, the maximum height of the radar for observing vibrations of the water surface with an amplitude of the order of 0.13 μm under the condition that the contrast is less than 1 dB can be estimated from the relation

$$h_{\max} \approx 1.7 \times (G_1 G_2 P), \tag{17}$$

where G_1 and G_2 are, respectively, the gains for the transmitting and receiving antennas of the information reading system, and P is the emitted microwave signal power. A calculation using Eq. (17) shows that the radar can be placed at a height of several kilometers with comparatively low emitted powers (tens of watts) and antenna gains (of the order of 1000). The maximum height can be increased by using special methods to extract the signal from the noise (correlation processing, accumulation, and so on).

In summary, the results of our experimental investigation show that the method of remote detection of a hydroacoustic signal according to phase modulation of 3-cm microwave reflections from the air–water interface can be used under natural conditions to transmit information from an underwater source to a receiving point in the atmosphere.

[1] V. A. Assman, F. V. Bunkin, E. A. Vinogradov, V. I. Golovanov, G. A. Lyakhov, N. V. Suyazov, and K. F. Shipilov, Pis'ma Zh. Tekh. Fiz. **17**(5), 72 (1991). [Sov. Tech. Phys. Lett. **17**, 185 (1991)].
[2] V. A. Assman, F. V. Bunkin, E. A. Vinogradov, V. I. Golovanov, G. A. Lyakhov, N. V. Suyazov, and K. F. Shipilov, Preprint No. 113, IOF AN SSSR (Moscow, 1990), 29 pp.
[3] G. A. Lyakhov, N. V. Suyazov, I. E. Ushakov, and I. F. Shishkin, Pis'ma Zh. Tekh. Fiz. **20**(16), 44 (1994) [Tech. Phys. Lett. **20**, 665 (1994)].
[4] V. A. Syrvachev, I. F. Shishkin, and I. E. Ushakov, Metrologiya, No. 2, 38 (1979).
[5] I. E. Ushakov and I. F. Shishkin, in *Problems of the Signal Formation and Processing in Radio Electronic Systems* (Taganrog Radio Engineering Institute, Taganrog, 1980), Vol. 4, pp. 55–62.
[6] I. E. Ushakov and I. F. Shishkin, *Radar Sounding of the Sea Surface* (RITS ''Tat'yanin den','' Moscow, 1997), 264 pp.
[7] *Underwater Acoustics* (Russian translation, Mir, Moscow, 1979), pp. 325–346.
[8] R. D. Urik, *Principles of Hydroacoustics* (Russian translation, Sudostroenie, Leningrad, 1978), 445 pp.

Translated by M. E. Alferieff

Effect of the rise rate of nanosecond high-voltage pulses on the breakdown of air gaps

L. M. Vasilyak, S. P. Vetchinin, and D. N. Polyakov

Scientific-Research Center for Thermal Physics of Pulsed Actions, Joint Institute of High Temperatures, Russian Academy of Sciences, Moscow

(Submitted June 2, 1999)
Pis'ma Zh. Tekh. Fiz. **25**, 74–80 (September 26, 1999)

The breakdown velocity increases to 10–20 cm/ns when the leading edge of the negative voltage pulse decreases to 0.5–2.5 ns. The sharp increase in the velocity can be explained by the appearance of a short-pulse beam of high-energy electrons which produce in the gap a sufficient number of initial electrons. © *1999 American Institute of Physics.* [S1063-7850(99)02709-3]

Spark breakdown of long air gaps at atmospheric pressure occurs by the streamer and streamer–leader mechanisms. The leader velocity is $2-5\ \mathrm{cm}/\mu\mathrm{s}$,[1] though the streamer velocity can reach 1 cm/ns, and for this reason it is assumed that the rise rate of the voltage pulse should not affect the shorting time of the gap. On the other hand, it is known that the breakdown of long gas tubes by pulses with nanosecond leading edges occurs in the form of high-velocity waves of ionization with 1–10 cm/ns shorting velocities in the gap (Ref. 2) on account of the appearance of high-energy electrons in the wave front. It is known that the appearance of runaway electrons during breakdown of short gaps in dense gases by high-voltage pulses with a nanosecond leading edge makes the dynamics of breakdown substantially different from static or microsecond breakdown.[3,4]

Our objective in the present work is to investigate the processes influencing the propagation velocity of electric breakdown in atmospheric air with an increasing rise rate of the voltage pulse. The experimental arrangement and the methods employed are similar to those of Ref. 5. Breakdown of up to 25 cm long air gaps with different geometry (sphere–sphere with 4 cm diameters, plane–plane in the form of 21 cm in diameter disks, tip–plane and tip–tip with 1 mm diameters and 4 cm length) was accomplished by pulses with up to 420 kV amplitude, 60 ns duration, and from 0.5 to 8 ns leading edge. The average propagation velocity of a discharge in the gap was determined from the time delay between the appearance of a voltage pulse on the high-voltage electrode and the appearance of a current pulse at the low-voltage electrode.[5] The dependences of the average discharge propagation velocity on the length of the discharge gap with a 420 kV voltage for negative pulses and 350 kV for positive pulses with different leading edge durations are presented in Fig. 1a for the sphere–sphere configuration and in Fig. 1b for the plane–plane configuration. In a nonuniform electric field, the velocity depends strongly on the rise rate of the incident pulse and increases with decreasing leading edge duration. The average velocity for negative pulses with a <3 ns leading edge decreases with increasing gap length and increases for more slowly rising pulses. Breakdown occurs most rapidly in the sphere–sphere configuration. The breakdown velocity is maximum for a 0.5 ns leading edge and reaches 10–20 cm/ns for negative pulses in gaps less than 8 cm long. As the gap length increases, the growth velocity of the channel decreases to 2–4 cm/ns and reaches the level observed for pulses with a 5–8 ns leading edge. The same dependence is observed in the plane–plane configuration. For gaps with tip–tip and tip–plane geometries, the velocity is lower than for the sphere-sphere geometry but greater than for the plane–plane geometry. The breakdown velocity in a uniform field for positive pulses, in contrast to negative pulses, is somewhat higher than in a nonuniform field, and it increases with the gap length.

The high rate of development of breakdown is due to additional mechanisms which arse at high voltage rise rates. Figure 2 shows the average breakdown field corresponding to the moment breakdown is detected in a sphere–sphere gap for negative pulses. It depends strongly on the duration of the leading edge. For pulses with long leading edges, the average breakdown fields in short gaps can reach 200 kV/cm. For pulses with extremely short leading edges, 0.5–2.5 ns, when breakdown of short gaps occurs on the leading edge of the voltage pulse, the average breakdown fields in short gaps drop sharply to 15–20 kV/cm. It should be noted that for breakdown of gaps with a uniform field (plane–plane) by negative pulses with an 8 ns leading edge the average breakdown fields are close to the static intensity in a uniform field.

It is known that for breakdown of gaps several millimeters long by pulses with a nanosecond leading edge a beam of fast electrons can arise initially.[3] In our experiments, we observed powerful beams of high-energy electrons in much longer gaps. Fast electrons were detected according to the presence of x-ray bremsstrahlung. X-Ray radiation at the surface of a grounded electrode in the sphere–plane geometry was reliably detected on the basis of blackening of RT-5 film after three to five breakdowns only for breakdown of less than 8 cm long gaps by negative pulses with short leading edges 0.5–2.5 ns. For pulses with longer leading edges, no x-ray radiation was observed from the gap. Using the foil method, it was possible to determine that the maximum of the fast-electron spectrum occurs at 60–100 keV. In our case, the number of fast electrons produced during breakdown was much higher than in Ref. 3.

The high-energy electron beam arising can strongly affect the development of breakdown and can provide ultrahigh velocities in the case of breakdown by steep negative

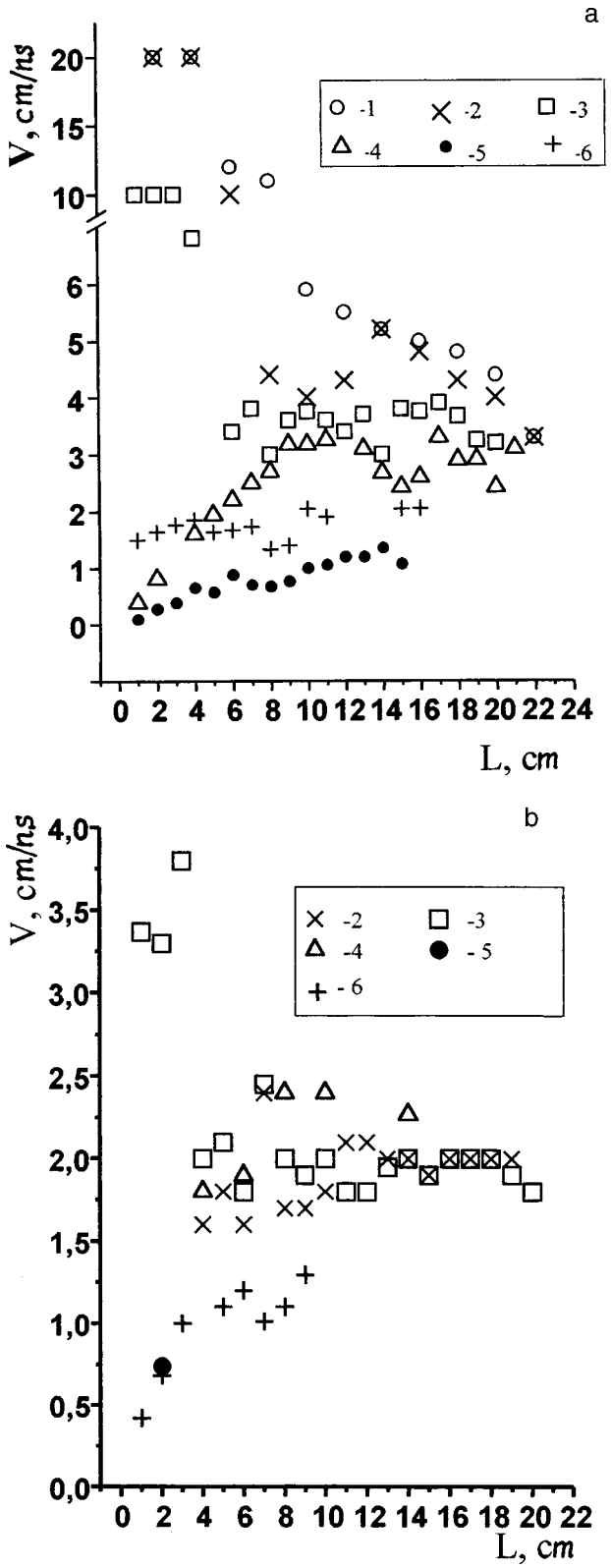

FIG. 1. Breakdown velocity versus the discharge gap length: a — sphere–sphere, b — plane–plane: *1–5* — negative polarity, *6* — positive polarity; *1* — 0.5 ns leading edge, *2* — 1.5 ns, *3* — 2.5 ns, *4* — 5 ns, *5*, *6* — 8 ns.

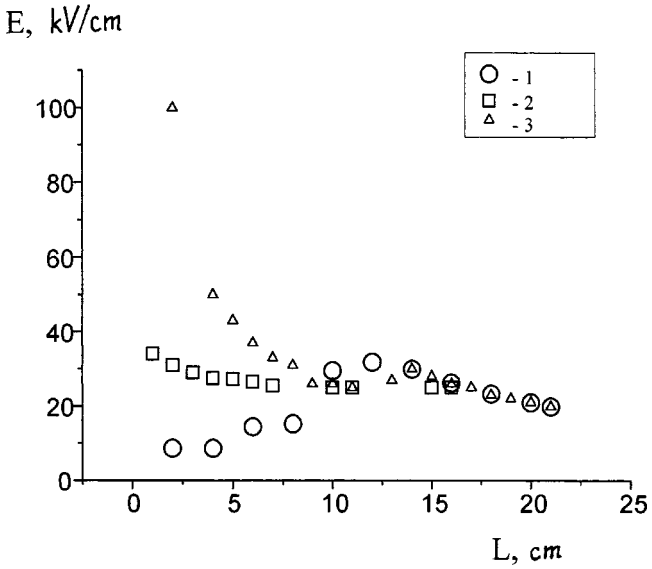

FIG. 2. Average breakdown field versus the discharge gap length for the sphere–sphere configuration with negative pulses: *1* — 0.5 ns leading edge, *2* — 2.5 ns, *3* — 5 ns.

pulses. The propagation velocity of streamers is limited by the production of the initial electrons in front of the streamer head. Fast electrons and the accompanying secondary electrons, arising as the beam moves in the gas, produce preionization ahead of the discharge front, which greatly facilitates the forward advancement of the front. In this case, a weak external electric field is required for motion of an ionization front, even with very high velocities. This is also confirmed by the data in Fig. 2, where the voltage drop for pulses with a short leading edge is recorded.

Under our conditions accelerated electrons appear at the stage when a breakdown wave propagates through the gap, in contrast to Ref. 3, where they were detected only on the leading edge of the current after the discharge shorted the gap. Their appearance is most likely explained by the mechanism of polarization acceleration on the front of the primary streamer,[3] which develops in the near-cathode region during the rapid growth of the voltage. For a sufficiently strong external field, this streamer with a strong local field at the head grows along an ionized path produced in the gas by the fast-electron flux. As a result of the high rate of ionization in a dense gas, such a negative streamer is a powerful high-velocity ionization front, which leaves behind it a high-conductivity plasma channel. The latter transfers the electrode potential to the streamer head. The conduction current flowing into the front should not be less than that required for charging the capacitance of the lengthening high-conductivity plasma channel: $I \sim CvU \sim 50-100$ A, where C is the capacitance per unit length of the streamer channel, v is the velocity, and U is the electrode potential. In the plane–plane case the uniform distribution of the field impedes the appearance of high-energy electrons.

For a positive pulse, the intensity of the electric field near the grounded electrode in a gap with a nonuniform field will be lower than at the high-voltage electrode, and fast electrons do not form or there are few such electrons and they move in a direction opposite to the direction of motion

of the ionization wavefront; this sharply decreases their effect on the development of breakdown.

In summary, increasing the rise rate of the negative pulse results in breakdown in the form of a high-velocity high-current negative streamer, whose front is a source of high-energy electrons, which fly out of it in the forward direction and produce preionization ahead of it. This mechanism gives breakdown velocities an order of magnitude higher than for streamer breakdown with photoionization ahead of the front.

This work was supported by the Russian Fund for Fundamental Research (Grant No. 98-02-17435).

[1] É. M. Bazelyan and Yu. P. Raĭzer, *Spark Discharges* (MFTI Press, Moscow, 1997).
[2] L. M. Vasilyak, S. V. Kostyuchenko, N. N. Kudryavtsev, and I. V. Filyugin, Usp. Fiz. Nauk **164**, 263 (1994).
[3] L. P. Babich, T. V. Loĭko, and V. A. Tsukerman, Usp. Fiz. Nauk **160**, 50 (1990) [Sov. Phys. Usp. **53**, 521 (1990)].
[4] Yu. D. Korolev and G. A. Mesyats, *The Physics of Pulsed Breakdown of Gases* (Nauka, Moscow, 1991).
[5] L. M. Vasilyak, S. P. Vetchinin, and D. N. Polyakov, in *Proceedings of the All-Russian Scientific-Educational Olympiad ''Plasma, 20th Century,''* including reports on the physics of low-temperature plasma FNTP-98 and lectures at the school for young scientists, Petrozavodsk, June 22–27, 1998, p. 327.

Translated by M. E. Alferieff

Antiferro–ferroelectric transition in the system $(1-x)NaNbO_3$—$xLiNbO_3$

I. B. Pozdnyakova, L. A. Reznichenko, and B. G. Gavrilyachenko

Rostov State University
(Submitted May 12, 1999)
Pis'ma Zh. Tekh. Fiz. **25**, 81–85 (September 26, 1999)

The dielectric properties of the system $(1-x)NaNbO_3$—$xLiNbO_3$ are investigated. The antiferro–ferroelectric transition region is determined for the first time. It is found that the antiferroelectric phase is stable for $x \leqslant 0.015$, while the ferroelectric phase is stable for $x \geqslant 0.0225$. The transition from one phase to another occurs in the concentration range $0.015 < x < 0.0225$. © *1999 American Institute of Physics.* [S1063-7850(99)02809-8]

As is well known, in the system $(1-x)NaNbO_3$—$xLiNbO_3$ the antiferroelectric (AFE) phase, which is characteristic of pure sodium niobate, becomes unstable even for low concentrations of the second component, transforming into the ferroelectric (FE) phase. Despite the large number of works on this system,[1–4] the exact location of the AFE–FE transition has still not been determined. In the present work we investigated in detail the dielectric properties of the system in the entire range of solubility of $LiNbO_3$ in $NaNbO_3$ ($0 \leqslant x \leqslant 0.145$), and the region of the AFE–FE transition is determined on the basis of the data obtained.

Ceramic samples in the system $(1-x)NaNbO_3$—$xLiNbO_3$ were obtained by solid-phase synthesis followed by hot pressing using ''Nbo–PT'' grade Nb_2O_5. Forty four compositions from the concentration range $0 \leqslant x \leqslant 0.145$ with average step $\Delta x \approx 0.003$ were investigated. The temperature dependences of the permittivity $\varepsilon(T)$ in the temperature range 20–600 °C with a constant electric field and in the absence of a field as well as the dielectric hysteresis loops were studied. The experimental samples were prepared in the form of 8–10 mm in diameter and 1 mm thick disks. The electrodes were deposited by annealing silver paste.

The experimental apparatus made it possible to obtain the temperature dependence $\varepsilon(T)$ by the bridge method ($f = 20$ kHz, $E_{\sim} = 10$ V/cm) under the action of a constant electric field. The conduction current was monitored in order to eliminate errors in determining the field acting on the sample; the field strength on the sample was 0.5–5 kV/cm. The concentration dependences of the transition temperatures ($T_c(x)$) and the field-induced ($\Delta T_c(x)$) change in T_c were determined from the temperature measurements. The dielectric hysteresis loops were observed with a Sawyer–Tower scheme at room temperature at frequency 50 Hz, and the external field applied to the sample reached 50 kV/cm. The x dependences of the coercive field E_c and the residual polarization P_0 were determined from the data.

Analysis of the dependences $\varepsilon(T)$ in the absence of an external electric field shows that in all compositions studied there exists a single anomaly of ε, which is stable with respect to heating–cooling cycles and corresponds to temperatures 335–405 °C during heating and 295–350 °C during cooling, in agreement with the results of Ref. 4. The Curie–Weiss law with the constant $C_w = (2-3.5) \times 10^5$ °C is satisfied above the transition point.

Figure 1 shows the x dependence of the change in T_c under the action of a constant electric field for 1 kV/cm (ΔT_c). It is evident that in samples with $x \leqslant 0.015$, the field

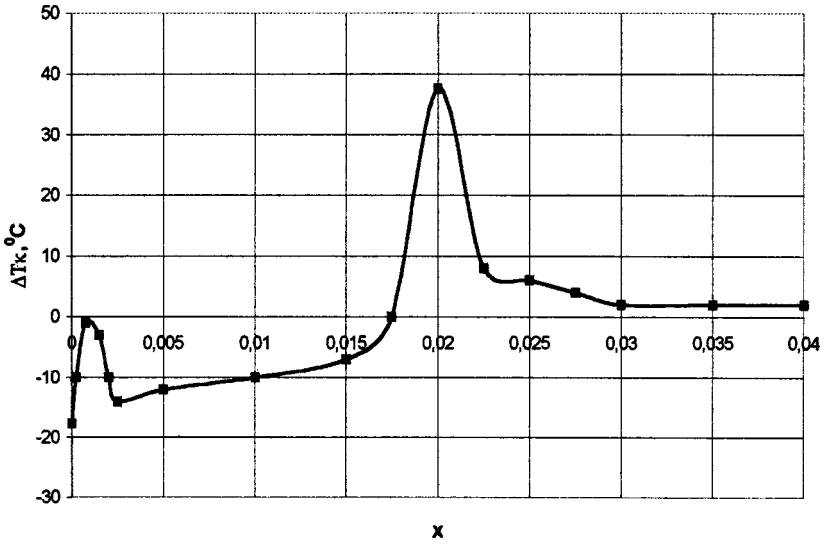

FIG. 1. Field-induced shift of the Curie temperature (ΔT_c) for 1 kV/cm versus the concentration x in the system $(1-x)NaNbO_3$—$xLiNbO_3$.

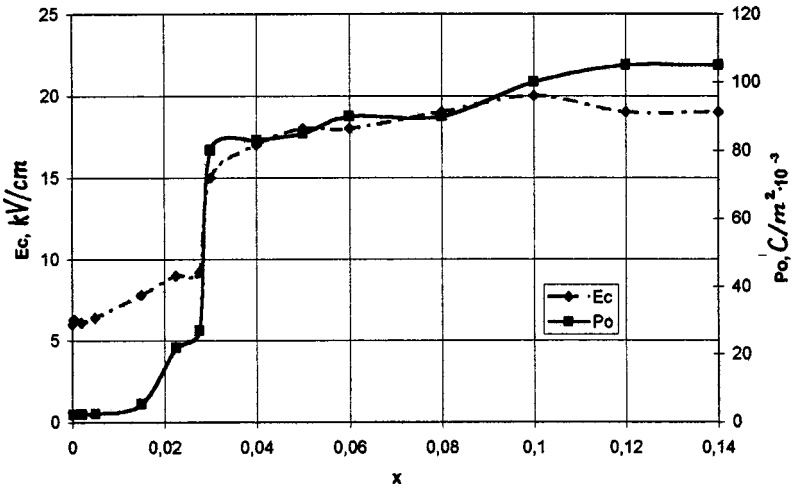

FIG. 2. Coercive field E_c and residual polarization P_0 versus the concentration x in the system $(1-x)NaNbO_3$—$xLiNbO_3$.

shifts T_c in the direction of low temperatures, as is characteristic of antiferroelectrics, while for $x \geqslant 0.0225$ the shift occurs in the opposite direction, as in ferroelectrics. The small peak in ΔT_c at $x=0.00075$ is due to the high density of defects in these compositions, which is due to Li ions occupying irregular positions of $NaNbO_3$, as confirmed by x-ray crystallographic methods. The peak in ΔT_c in the range $0.0175 \leqslant x \leqslant 0.02$ indicates a high mobility of structural elements due to a transition from the AFE into the FE phase. Further stabilization of the FE phase leads to ''stiffening'' of the structure and, in consequence, to a decrease of ΔT_c in the range $0.02 \leqslant x \leqslant 0.025$ and a negligible change with increasing x ($\Delta T_c \sim +3-1\,^\circ$C). For this reason, the concentration range $0 \leqslant x \leqslant 0.04$ is presented in the figure.

Ferroelectric hysteresis loops were observed in all compositions, including pure sodium niobate. For an electric field $E=35$ kV/cm in $NaNbO_3$ obtained using ''Nbo–PT'' Nb_2O_5, the coercive field is 6 kV/cm and the residual polarization is 2.3×10^{-3} C/m^2. When the field is applied gradually, the threshold value at which an FE loop arises is 6 kV/cm. For $NaNbO_3$ obtained from ultrapure Nb_2O_5, for $E=35$ kV/cm, $E_c=2.5$ kV/cm, and $P_0=1.1\times10^{-3}$ C/m^2 the threshold field is 10 kV/cm.

The presence of an FE hysteresis loop in $NaNbO_3$ could attest to a possible field-induced transition into the FE state in some crystallites of the ceramic, where the direction of antipolarization makes an optimal angle with the direction of the external field, as is observed in single crystals,[5] and to the possible coexistence of AFE and FE phases in it.[6] Low values of P_0 indicate that the FE phase is metastable. The higher values of E_c and P_0 in ''Nbo–PT'' $NaNbO_3$ as compared with ultrapure material can be explained by the presence in the former of a large number of various impurities, which can stabilize the FE phase. This is supported by the fact that the threshold field for the appearance of a FE hysteresis loop is lower. As x increased, the form of the hysteresis loop changed as follows: For $x \leqslant 0.015$ E_c and P_0 were essentially the same as the values obtained for $NaNbO_3$, and for $x>0.0225$ E_c and P_0 were appreciably higher. The dependences $E_c(x)$ and $P_0(x)$ are presented in Fig. 2.

In summary, it can be asserted on the basis of the present investigation that in the system $(1-x)NaNbO_3$—$xLiNbO_3$ the AFE phase is stable for $x \leqslant 0.015$, and the FE is stable for $x \geqslant 0.0225$. The transition from the AFE into the FE phase occurs in the range $0.015<x<0.0225$.

This work was partially supported by the Russian Fund for Fundamental Research under grant No. 99-02-17575.

[1] L. A. Peznichenko and L. A. Shilkina, Izv. Akad. Nauk SSSR, Ser. Fiz. **39**, No. 5, 1118 (1975).
[2] L. A. Reznichenko and L. A. Shilkina, Zh. Tekh. Fiz. **47**, 453 (1977) [Sov. Phys. Tech. Phys. **22**, 272 (1977)].
[3] L. A. Shilkina, I. V. Pozdnyakova, and L. A. Reznitchenko, *The Book of Abstracts of the IMFS-8* (Rostov-on-Don, 1998), pp. 190–191.
[4] G. Kus, W. S. Ptak, and W. Smiga, Ferroelectrics **124**, 249 (1991).
[5] V. G. Smotrakov, V. Yu. Topolov, and O. E. Fesenko, Fiz. Tverd. Tela (St. Petersburg) **39**(6), 1084 (1997) [Phys. Solid State **39**, 972 (1997)].
[6] J. Chen and D. Feng, Phys. Status Solidi A **109**, 171 (1988).

Translated by M. E. Alferieff

Role of internal stresses in the localization of plastic flow of irradiated materials

N. V. Kamyshanchenko, V. V. Krasil'nikov, V. V. Sirota, I. M. Neklyudov, and A. A. Parkhomenko

Belgorod State University, National Science Center ''Khar'kov Physicotechnical Institute''
(Submitted June 23, 1999)
Pis'ma Zh. Tekh. Fiz. **25**, 86–90 (September 26, 1999)

The collective behavior of dislocations in irradiated materials is studied using the kinetic equation for the dislocation density, taking account of a Burgers-type nonlinearity. It is shown that the degree of dislocation localization in slip bands is higher in the irradiated materials than in the unirradiated materials. © *1999 American Institute of Physics.*
[S1063-7850(99)02909-2]

There now exist several theoretical approaches for studying processes in the collective behavior of dislocations.[1] Often, in the evolutionary equations for the dislocation density $\rho(\mathbf{x},t)$ ($\mathbf{x}$ is the spatial coordinate and t is the time) the nonlinearity of the plasticity processes is represented by terms which are quadratic in the dislocation density.

In the present letter the kinetic equations that describe the collective behavior of dislocations taking account of the so-called Burgers nonlinearity, i.e., terms of the type $\rho(\partial\rho/\partial x)$, are used.

We proceed from balance equation for the density of moving dislocations[1,2]

$$\frac{\partial\rho(\mathbf{x},t)}{\partial t}+\mathrm{div}(\mathbf{V}\rho(\mathbf{x},t)-D\Delta\rho(\mathbf{x},t))=Q(\rho(\mathbf{x},t)), \qquad (1)$$

where $\mathbf{V}$ is the dislocation glide velocity, D is the dislocation diffusion coefficient, and $Q(\rho(\mathbf{x},t))$ is a functional of the dislocation density, determining the interaction of dislocations with one another. We shall consider a simplified model of a crystal, for which the moving dislocations glide in one plane in a certain definite direction, determined by the Ox axis, and possess charges with the same sign. The dislocation glide velocity V (since the motion is one dimensional, we omit the sign of the vector) is, generally speaking, a functional of the dislocation density, since the dislocation glide velocity can be represented as consisting of three parts $V=V_{\mathrm{ext}}+m(f_{\mathrm{int}}+f_{\mathrm{cor}})$, where V_{ext} is the velocity due to the external load, m is the dislocation mobility, and f_{int} is the internal stress force produced, for example, by the dislocation charges,[3] and is determined by the Green's function for the elastic problem

$$f_{\mathrm{int}}=b\int K(x-x',t-t')\rho(x',t')dx'dt',$$

where b is the magnitude of Burgers vector and the function $K(x-x',t-t')$ is determined by the nonlocal influence of the dislocation density and fluxes. In the leading approximation in the spatial gradient, it can be shown that

$$f_{\mathrm{int}}=bK\rho(x,t), \qquad (2)$$

where K is a proportionality coefficient and f_{cor} is a correlation force, arising due to the relative arrangement of the dislocations,[3] and is given by

$$f_{\mathrm{cor}}=\frac{Gb^2}{4\pi\rho_0}\frac{\partial\rho}{\partial x}, \qquad (3)$$

where G is the shear modulus and ρ_0 is a certain stationary dislocation density.

We shall assume the right-hand side of Eq. (1) to be zero. The physical justification for this is that we are interested in plastic flow in irradiated materials. According to recent works,[4] irradiation has an enormous effect on dislocation generation at the initial stages, often almost completely suppressing it, as a result of the strong blocking of dislocation sources by very small clusters of interstitial atoms. Moreover, dislocation annihilation processes are likewise suppressed by irradiation, since in irradiated deformable materials the properties of the dislocations themselves can change (expansion of dislocation nuclei, decrease of the defect packing energy).[5]

On the basis of these considerations, specifically, Eqs. (2) and (3), the balance equation (1) can be written in the form

$$\frac{\partial\rho}{\partial t}+\frac{\partial}{\partial x}\left(V_{\mathrm{ext}}\rho+mbK\rho^2+\left(m\frac{Gb^2}{4\pi\rho_0}-D\right)\right)=0. \qquad (4)$$

Writing $\rho(x,t)$ as

$$\rho(x,t)=\rho_0+\rho_1(x,t),$$

where ρ_0 is the average stationary dislocation density and $\rho_1(x,t)$ is the fluctuation of this density, we have

$$\frac{\partial\rho_1}{\partial t}+\alpha\frac{\partial\rho_1}{\partial x}+\rho_1\frac{\partial\rho_1}{\partial x}=-\delta\frac{\partial^2\rho_1}{\partial x^2}, \qquad (5)$$

where

$$\alpha=\rho_1+\frac{V_{\mathrm{ext}}}{2mbK},\quad \delta=\frac{1}{2Kb}\left(\frac{Gb^2}{4\pi}-\frac{D}{m}\right).$$

We note that the nonlinearity $\rho_1(\partial\rho_1/\partial x)$ is due to internal stresses produced by the dislocations. Analysis of the temperature dependences of the yield point of irradiated ma-

terials shows that the main effect of irradiation with neutrons and high-energy charged particles is due to an increase of the internal stresses, produced by radiation defects, on account of which in the irradiated materials the term $\rho_1(\partial\rho_1/\partial x)$ should play a dominant role.[5]

The stationary solution of Eq. (5) has the well-known form

$$\rho_1(x,t)=\alpha\delta\left(1+\tanh\frac{1}{2}(ax-a^2t\delta)\right), \tag{6}$$

where a is a constant determined by the boundary conditions, specifically, $\rho_1(x,t)\to\infty$ as $x-at\delta\to-\infty$. The solution (6) corresponds to the edge of the Chernov–Lüders band, i.e., the region where a jump occurs in the dislocation density. The ratio D/m appearing in the expression for δ (see Eq. (5)) can be written as

$$\frac{D}{m}=\frac{kT}{\nu}\cdot\frac{v_d}{V}\cdot\frac{\sigma_a}{\sigma_i}, \tag{7}$$

where k is Boltzmann's constant, T is the absolute temperature, v_d is the diffusion drift velocity of dislocations, σ_a is the stress of plastic flow in the slip plane, σ_i is the magnitude of the internal stresses, and ν is a numerical factor ($\nu\geqslant 1$). The ratio v_d/V in irradiated materials at the stage of formation of the localized-deformation bands decreases sharply as a result of the large increase in the fraction of dislocations moving with velocities of the order of $0.1c$ (c is the sound velocity) under the action of the stresses σ_a.[6] The factor σ_a/σ_i likewise decreases with increasing irradiation dose as a result of an increase in internal stresses. As a result of all this, increasing the irradiation dose will increase the height of the step determined by Eq. (6). This is illustrated qualitatively in Fig. 1, which shows three plots corresponding to the solution (6) for three values of the irradiation dose $p_1<p_2<p_3$.

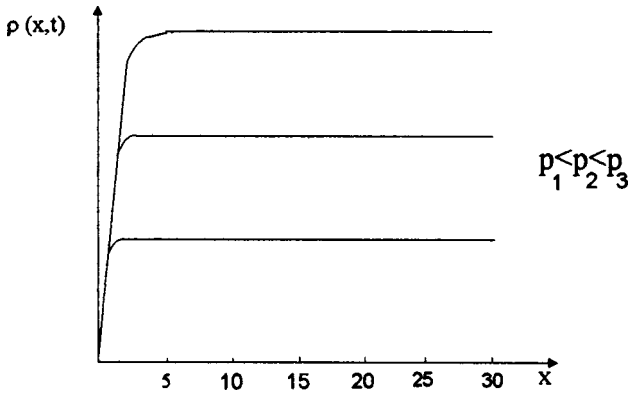

FIG. 1.

The increase in the step height as a result of irradiation corresponds to the experimental results showing an increase in the degree of localization of deformation in slip bands in irradiated materials. The dislocation density in them, even at doses less than one displacement per atom, is more than an order of magnitude higher than the dislocation density in the Chernov–Lüders bands in unirradiated materials.

[1] G. A. Malygin, Fiz. Tverd. Tela (St. Petersburg) **37**, 3 (1995) [Phys. Solid State **37**, 3 (1995)].
[2] G. F. Sarafanov, Fiz. Met. Metalloved. **85**(3), 46 (1998).
[3] Sh. Kh. Khannanov, Fiz. Met. Metalloved. **78**(2), 31 (1994).
[4] B. N. Singh, F. Horsewell, P. Tolf *et al.*, J. Nucl. Mater. **224**, 131 (1995).
[5] V. N. Voevodin, L. S. Ozhigov, A. A. Parkhamenko *et al.*, VANT. Ser. FRP i RM, No. 3(69), 4(40), 33 (1998).
[6] N. V. Kamyshanchenko, V. V. Krasil'nikov, I. M. Neklyudov *et al.*, Fiz. Tverd. Tela (St. Petersburg) **40**, 1632 (1998) [Phys. Solid State **40**, 1482 (1998)].

Translated by M. E. Alferieff

Propagation characteristics of plane waves of defects in a viscoplastic medium

N. V. Chertova and Yu. V. Grinyaev

Institute of Strength Physics and Materials Engineering, Siberian Branch of the Russian Academy of Sciences, Tomsk

(Submitted June 23, 1999)
Pis'ma Zh. Tekh. Fiz. **25**, 91–94 (September 26, 1999)

It is shown that dispersion is not observed in the propagation of a weakly damped wave, and dissipation is frequency-dependent. For strongly damped waves, dispersion and dissipation are observed. However, a wave in a viscoplastic medium decays over very short distances and the penetration depth of strongly damped waves of defects is bounded by the skin-layer thickness. © *1999 American Institute of Physics.* [S1063-7850(99)03009-8]

The system of dynamical equations of a dislocation ensemble

$$B\nabla\cdot I=-P, \tag{1.1}$$

$$\frac{\partial\alpha}{\partial t}=\nabla\times I, \tag{1.2}$$

$$\nabla\cdot\alpha=0, \tag{1.3}$$

$$S\nabla\times\alpha=-B\frac{\partial I}{\partial t}-\sigma, \tag{1.4}$$

derived on the basis of the gauge approach,[1–3] is the starting point for analyzing the defect field characterized by the dislocation density tensor α and the dislocation flux density tensor I in a medium with fixed effective stress σ and momentum $\mathbf{P}$. The quantity σ and P are related by the equation of dynamical equilibrium

$$\frac{\partial\mathbf{P}}{\partial t}=\nabla\sigma, \tag{2}$$

which is the condition of compatibility of Eqs. (1). In these expressions B and S are new constants of the theory, and the symbols $\cdot$ and $\times$ denote scalar and vector multiplication. Using the formal analogy between these equations and Maxwell's equations in electrodynamics,[4] the dislocation flux density tensor can be juxtaposed to the electric field tensor, the dislocation density tensor to the magnetic field intensity, the effective momentum to the charge, and the stress to the current, and we can write a material relation

$$\sigma=\eta I, \tag{3}$$

similar to the relation between the electromagnetic field in the presence of matter for a uniform conducting medium. In phenomenological theories of plasticity[5] this relation corresponds to the definition of viscoplastic flow, whence it follows that the coefficient η is a generalized viscosity of the medium. In the general case η is a viscosity tensor of rank 4, for which the number of independent components is determined by the symmetry of the medium and the tensors σ and I.

We shall study the laws of propagation of plane harmonic waves of defects in a viscoplastic medium on the basis of Eqs. (1)–(3). According to Eqs. (3) and (1.1), the equation of dynamical equilibrium can be written as

$$\frac{\partial\mathbf{P}}{\partial t}=-\frac{\eta}{B}\mathbf{P}, \tag{4}$$

whence

$$P=P_0\exp(-t/t_0),$$

i.e., the effective momentum in a viscoplastic medium decreases with time, where $t_0=B/\eta$ is the relaxation time. Taking this into account and setting the right-hand side of Eq. (1.1) equal to zero, the system of equations (1) can be written in the form

$$\frac{B}{S}\frac{\partial^2\alpha}{\partial t^2}-\Delta\alpha+\frac{\eta}{S}\frac{\partial\alpha}{\partial t}=0,$$

$$\frac{B}{S}\frac{\partial^2 I}{\partial t^2}-\Delta I+\frac{\eta}{S}\frac{\partial I}{\partial t}=0,$$

where Δ is the Laplacian. Let us assume that the field intensities α and I depend only on the coordinate x. Setting $\alpha=\alpha_0(x)\exp(-i\omega t)$, we obtain for the complex amplitude the Helmholtz equation

$$\frac{d^2\alpha_0}{dx^2}+\omega^2\frac{B}{S}\left(1+\frac{i\eta}{B\omega}\right)\alpha_0=0, \tag{5}$$

where

$$k^2=\omega^2\frac{B}{S}\left(1+\frac{i\eta}{B\omega}\right). \tag{6}$$

The solution of Eq. (5) (an analogous equation is obtained for I_0) can be written in the form

$$\alpha_0=c_1\exp(ikx)+c_2\exp(-ikx),$$

where c_1 and c_2 are unknown constants, to be determined from the boundary conditions, and the expression for k can be represented as

$$k=\omega(n+i\chi)/C. \tag{7}$$

Here n and χ are the refractive index and the absorption coefficient, and $C=\sqrt{S/B}$. The absorption coefficient χ is

characterized by the rate of decrease of the wave amplitude in the direction of wave propagation, and $n=C/V$ determines the phase velocity of the waves in the medium.

We shall now determine the dependence of n and χ on the frequency of the wave and the parameters of the medium. Let $\tan\delta=\eta/B\omega$, called the tangent of the loss angle. Equating the expressions (6) and (7)

$$(1+i\tan\delta)=(n+i\chi)^2,$$

we obtain

$$n=\sqrt{(1+\sqrt{1+\tan^2\delta})/2}, \quad \chi=\sqrt{(\sqrt{1+\tan^2\delta}-1)/2}, \tag{8}$$

i.e., in a viscoplastic medium the refractive index and absorption coefficient depend on the frequency, since $\tan\delta\sim 1/\omega$, and the medium is dispersive. When plane waves of arbitrary form propagate in a dispersive medium, the wave profile becomes distorted, since the phase velocity V and the damping coefficient $\omega\chi/C$ are not the same for different frequency components.

Let us consider the limiting cases of large and small losses. For a weakly damped wave, so that $\tan\delta\ll 1$ or $\omega t_0\gg 1$,

$$n=1=\text{const}, \quad \chi=\tan\delta/2=\chi(\omega), \tag{9}$$

i.e., dispersion is not observed in the propagation of a weakly damped wave, and dissipation is frequency-dependent. For strongly damped waves, $\tan\delta\gg 1$, so that

$$n\approx\chi=\sqrt{\tan\delta/2}=\sqrt{\eta/(2B\omega)}, \tag{10}$$

i.e., dispersion and dissipation are observed. However, for $\tan\delta\gg 1$ or $\omega t_0\ll 1$ there is essentially no wave process, since the wave decays over very short distances. The amplitude decreases by a factor of e over a distance

$$d=C/(\chi\omega)=\lambda/(2\pi\chi), \tag{11}$$

which for $\tan\delta\gg 1$ and $n\approx\chi\gg 1$ is much shorter than the wavelength λ. Therefore the penetration depth of defect waves in a viscoplastic medium with strong damping is bounded by the skin-layer thickness (11), where

$$\chi=\sqrt{(\sqrt{1+(\eta/B\omega)^2}-1)/2}$$
$$=\sqrt{(\sqrt{1+(\eta\lambda/2\pi BC)^2}-1)/2}.$$

The surface localization of waves of defects, as established above, makes it possible to understand the physical nature of many experimentally observed facts in fatigue fracture, and ultrasonic treatment. For example, it is known[6] that if repeated loads act on a sample, then a fatigue crack forms in the high-stress region, usually on the surface of the sample, and propagates until complete fracture occurs. The results obtained can be used to explain why a fatigue cracks forms at the surface. The reason is that the dislocation density localized at the surface corresponds, by definition of a defect in the continuum theory,[7] to internal stresses concentrated in the same region. Internal stresses engender a fatigue crack, and the fluxes of defects, also localized at the surface, determine the development of the crack.

[1] A. Kadic and D. G. B. Edelen, *A Gauge Theory of Dislocations and Disclinations* (Springer, Heidelberg, 1983).
[2] Yu. V. Grinyaev and V. E. Panin, Dokl. Akad. Nauk SSSR **353**, 37 (1997) [Phys. Dokl. **42**, 108 (1997)].
[3] Yu. V. Grinyaev and N. V. Chertova, Zh. Tekh. Fiz. **68**(9), 134 (1998) [Tech. Phys. **43**, 1128 (1998)].
[4] L. D. Landau and E. M. Lifshitz, *Electrodynamics of Continuous Media* (Pergamon Press, New York) [Russian original, Nauka, Moscow, 1982].
[5] P. Perzyna, *Fundamental Problems of Viscoplasticity* (Russian translation, Mir, Moscow, 1968).
[6] P. Forrest, *Fatigue of Metals* (Pergamon Rpr. UK, 1962; Mashinostroenie, Moscow, 1968).
[7] A. M. Kosevich, *Principles of the Mechanics of Crystal Structure* (Russian translation, Mir, Moscow, 1972).

Translated by M. E. Alferieff